Efficient Resource Allocation for 5G Hybrid Wireless Networks

Yongxu Zhu

A dissertation submitted in partial fulfillment

of the requirements for the degree of

Doctor of Philosophy

of

University College London.

Department of Electronic and Electrical Engineering

University College London

September 5, 2017

I, Yongxu Zhu, confirm that the work presented in this thesis is my own. Where information has been derived from other sources, I confirm that this has been indicated in the work.

Abstract

This thesis explores three directions of energy-efficiency(EE) and spectral-efficiency(SE) under 5G wireless networks. Firstly, we study the optimization of power control for the small (two-user) interference channel in which the terminals are time-switched between the signal-processing and energy-harvesting phases. Both energy harvesting and signal-processing processes are during the downlink. The objective is to maximize the sum-rate, subject to the minimum data and harvested energy constraints at the receivers, assuming a fixed time-switching coefficient. The key contribution is using a geometric approach that analyzes the feasible region governed by the constraints, which gives rise to the optimal power control solution.

Another topic focuses on the performance analysis of two user association schemes for wireless power transfer (WPT) in heterogeneous networks (HetNets) massive multiple-input multiple-output (MIMO) antennas, downlink for the WPT in the first phase and uplink for wireless information transfer (WIT) in the second phase. The two user association schemes considered in the analysis are the Downlink received signal power (DRSP) based approach for maximizing the harvested energy; and the uplink received signal power (URSP) based approach for minimizing the uplink path loss. In the downlink, we adopt a low-complexity approach for massive MIMO power transfer to recharge users. Then we derive the average uplink achievable rate with the harvested energy.

The last topic analyses a large-scale mmWave ad hoc network in the randomly located eavesdroppers area, where eavesdroppers can still intercept the confidential messages, since they may reside in the signal beam. This chapter explores the

potential of physical layer security in mmWave ad hoc networks. Specifically, we characterize the impact of mmWave channel characteristics, random blockages, and antenna gains on the secrecy performance. For the special case of the uniform linear array (ULA), a tractable approach is proposed to evaluate the average achievable secrecy rate.

Acknowledgements

The work presented in this thesis would not have been possible without the support and advice received from a multitude of people to whom I would like to express my most sincere gratitude.

First and foremost, I would like to thank my supervisor, Professor Kai-Kit Wong, for constantly providing me advices, encouragements and graveness which I will benefit for the rest of my life. I will always be in his debt for his help and instruction.

I am also very grateful to all my seniors, Dr Lifeng Wang for his sincerely help and countless discussions in academic; Prof. Shi Jin for his encouragement and generous assistance; Prof. Caijun Zhong, Dr Arman Shojaeifard and Dr Muhammad RA Khandaker for their insights and constant supports in research. Especially thank Dr Gan Zheng who supported my first postdoctoral job in life.

I would also like to thank my group, love and warm family 'UCL Wireless', Mr Raoul, for his honest and kindly help before group every meeting. Mr Alex, always took my photos when I am presenting in the conference. Also, I would like to thank Miss Jialing, Miss Xiaoyan and Mr Emanuele for share the research experience.

Last but not least, I am deeply grateful to my family. In particular, my husband, my faithful companions, Mr Jie Deng for his encouragement and positive attitude during my growth in academic and daily life. Thanks to my mother, father and parents in law, for their supports and concerns every day, they are the foundation of all my achievements.

Contents

List of Figures

List of Tables

Chapter 1

Introduction

1.1 Background

To meet the increasing demand for high speed and high quality wireless services, the fourth generation (4G) network has been rolling out in large-scale by major mobile service operators worldwide [4], which intends to provide a peak speed of 100 Mbit/s for high mobility communication (such as from trains and cars) and 1 Gbit/s for low mobility communication (such as pedestrians and stationary users). In the meantime, as the 4G network enters the commercial deployment stage, both the industry and academia have started the research on the fifth generation (5G) networks.

Compared to the 4G networks, a number of key features of the 5G networks has been identified [5]: (1) 100 times number of connected devices, (2) 1000 times higher mobile data volume per area, (3) 100 times higher data rate, (4) 1 millisecond latency, (5) 99.99% availability and coverage, (6) 0.1 times energy consumption as compared to 2010, (7) real-time information processing and transmission, (8) 0.2 times network management operation expenses, and (9) seamless integration of the current wireless technologies.

The dramatic increase in the wireless access speed has promoted the fast development of mobile internet, enabling a plethora of new types of mobile services such as mobile social, mobile payment, online gaming and mobile video. With the penetration of the mobile internet into the daily life of people at an unprecedented

pace, one of the critical problems in the industry is working out how to augment the operation time and the transmission rate of mobile terminals, which has become the single most important factor affecting user experiences. Unfortunately, the technological improvements for both battery capacity and transmission rates have been rather slow over the last decades. As such, seeking novel and effective transmission solutions has emerged as one of the major challenges in the area of information technology.

Moreover, another key scenario of 5G technology is the Internet-of-Things (IoT) networks, where thousands and millions of small devices such as sensors are connected to the internet, with a wide range of applications such as smart home, manufacturing, energy management, connected cars, and wearable devices.

Since these are groups of small devices which demand more resources including battery and spectrum, a major challenge is coordinating the network and making full use of the available resources, which is not only costly but is also a hostile environment.

Therefore, how to tackle this issue is of central importance. To this end, increasing the energy-efficiency has emerged as a promising way to address the above-mentioned challenges. In particular, far-field wireless power transfer (WPT) is one way to improve the energy-efficiency of the network dramatically. WPT could not only potentially tackle the problem of short operation time, but also eliminate the needs of power cable, thereby offering great freedom and convenience to end users. MmWave links are another way of increasing energy efficiency due to mmWave only needs limited transmission power and beamwidth. As such, it is expected that the energy-efficiency strategy would help more communication equipment in the IoT networks, including large-scale sensor networks as well as smart-grid networks. Due to the short range and high-density features of next generation networks, studying WPT and mmWave in 5G networks is highly non-trivial and requires substantial research efforts. For this reason, in this thesis, we make a provisional study of how to increase the overall resource effectiveness of wireless communications systems and how to devise sophisticated techniques to improve the

performance of wireless powered communications systems.

There is no doubt that providing efficient resource allocation schemes is also worthy of the wireless network. The radio frequency spectrum is a finite and precious natural resource that is critical especially for wireless communications. More than that, the resource allocation involves feasibility regions, spectrum resource management, network utility maximization, quality of service (QoS) support, convexity issues, proportional fairness, max-min fairness, efficiency versus fairness trade-off, interference hunting.

1.2 Promising Key 5G Wireless Technologies

Enhancing the performance and practical implementation of resource effectiveness is a major challenge. In particular, how to improve the overall resource effectiveness of wireless network is a critical problem to be tackled.

In this section, we first introduce energy harvesting (EH) systems and some recent processes on WPT, and then discuss two key techniques namely heterogeneous networks (HetNets) and massive multiple-input multiple-output (massive MIMO). Finally, we introduce Millimeter wave (mmwave) communication systems.

1.2.1 WPT and EH

By scavenging energy from natural resources such as solar and wind, EH systems can potentially operate in a self-sustained manner, i.e., no external power supply from the power grid is required. Hence, it has received enormous interest in recent years.

Traditional EH sources such as solar, wind, and hydroelectric power highly depend upon time and locations, as well as the conditions of the environments-it dictates the amount and rate of energy available for use. Wireless power transfer (WPT) in contrast is a much more controllable approach to prolong the lifetime of mobile devices [6, 7].

In wireless EH systems, [8] considered the wireless link where the receiver switches between being an energy receiver (ER) and an information receiver (IR). When the receiver operates as an ER, it replenishes energy opportunistically from

the unintended interference and/or the intended signal sent by the transmitter. To characterize the system performance trade-offs, the outage-energy and rate-energy regions were analyzed. Given the channel state information (CSI) at the transmitter, the joint optimization of transmitter power control, information and energy transfer scheduling, and the receiver's mode switching was also studied based on the instantaneous CSI and interference conditions.

In [9], analysis has shown that base stations have a much higher operational energy budget than mobile terminals when accounting for manufacturing or embodied energy costs. With the comprehensive deployment of battery powered wireless devices, in order to extend the lifetime of wireless networks, [10] presented optimally the transmission power policies for maximizing the throughput, given either causal side information or full side information.

A queue stabilizing transmission strategy was developed in [11] for a recharging battery powered transmitter. Another work in EH in [12] presented transmission policies that minimize the transmission completion time of a given group of data.

However, one of the major issues with the traditional EH system is that the amount of harvested energy from natural resource depends heavily on the time, location, as well as the weather conditions; hence, it may not be suitable for systems with stringent reliability requirement. In contrast, the radio frequency (RF) signals can be fully controlled; hence, the WPT based EH systems can provide much higher reliability [6].

Since the RF signals can carry both information and energy, a new concept, referred to as simultaneous wireless information and power transfer (SWIPT), has emerged.

SWIPT has already opened up new opportunities and led to numerous interesting but challenging optimization problems, e.g., [13, 14]. In [13], an energy-harvesting sensor network was investigated, in which a sensor node uses the harvested energy from the environment to generate and transmit data packets. Energy management policies that are throughput-optimal and delay-minimal were devised. Subsequently, in [14], the authors considered the use of energy harvesters as the en-

ergy sources and addressed the energy allocation problem according to the channel conditions and energy sources for maximizing the rate. Both causal and non-causal side information were considered, and the optimal energy allocation was obtained using dynamic programming and convex optimization techniques.

Due to the broadcast nature of wireless channels, in SWIPT systems, the messages sent to IRs can be eavesdropped by the ERs. In [15], a multiuser multiple-input single-output (MISO) SWIPT system was considered and the maximization of the secrecy rate for the IR subject to individual harvested energy constraints of the ERs was studied. The problem of maximizing the weighted sum-energy at the ERs subject to a secrecy rate constraint for the IR was also investigated.

Recently, SWIPT has been used for even more complex system model, e.g., [16–18]. In [16], a secrecy problem similar to [15] was tackled, but with consideration of imperfect CSI. The problem was further investigated in [17] to cope with the case that the ERs can collude to perform joint decoding to illicitly decode the secret message to the IR.

For complexity purpose, there remains two key challenges for practical implementations: one is time switching (TS) and another is power splitting (PS) . Compared to the PS approach, SWIPT can be realized using time-switching at more affordable complexity. Very recently in [18], the authors provided a thorough study for time-switching SWIPT in MIMO interference channels. Assuming that perfect cancellation of energy signals is possible at the receivers, *collaborative* energy beamforming was obtained.

1.2.2 Heterogeneous networks

Dense HetNets, which substantially reduce the distances between the BS and mobile terminals, can effectively mitigate the path-loss effect. Dense HetNets [19] offer a fast, flexible and cost-efficient extension for the traditional macro cellular networks that can coordinate the areas with uneven traffic distribution. However, the users in HetNets are affected from surrounding interference due to the universal spectrum use of different cells. HetNets are likely to become the dominant theme for WPT in 5G.

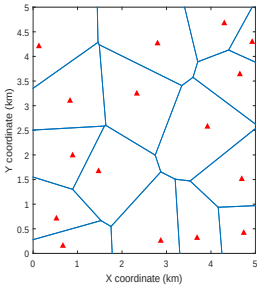

(a) Actual 4G deployment [21]

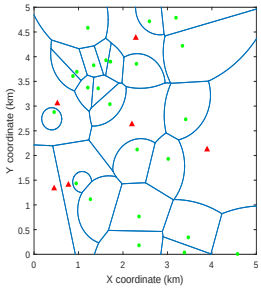

(b) Two-tier HetNet

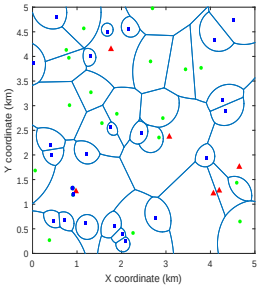

(c) Three-tier HetNet

Figure 1.1: Cellular Network Topology.

The effect of biased user association was investigated in the context of multi-tier downlink HetNets in [20] with the aid of stochastic geometry. Due to coverage footprints mostly changed by the deployment of small cells, the modeling of multi-tier HetNet does not follow the traditional hexagonal grid model as in the single-tier cellular network. The difference between the topology of the actual 4G deployment, the two-tier and three-tier HetNets is shown in Fig. 1.1.

Here, random spatial model means the locations of BSs in each tier follow a specific probability distribution.

Recently, there is an interesting integration between WPT and HetNets, suggesting that stations, referred to as power beacons (PBs), be deployed in cellular networks for powering users via WPT [7]. However, deploying large numbers of PBs just for recharging mobile users has been proved to be highly cost ineffective and worse, could generate unnecessary interference.

Regarded as a promising network architecture to meet the increasing demand for mobile data, massive MIMO empowered HetNets have recently attracted much

attention [22, 23], in [24] the total power consumption can be significantly reduced while satisfying the QoS constraints.

Paper [25] proposed the user association in a massive MIMO HetNet, realized the centralized and distributed user management. Particularly, they developed fairness optimal algorithms for maximizing the rate performance.

In [26], the authors explored a framework of cooperative green HetNet for 5G wireless communication systems, which aims at balancing and optimizing spectrum efficiency (SE), energy efficiency (EE), and QoS in 5G wireless communication systems.

Above all, the most important cellular architecture in 5G should also be a heterogeneous one. Energy cooperation under the hybrid energy sources scenario could support a large number of mobility terminals' energy requirements.

1.2.3 Massive MIMO

Massive MIMO systems [27] also known as large-scale antenna systems, which use of a very large number of antennas with sharp beam (around hundreds or thousands) that are operated fully coherently and adaptively [28, 29]. They promise an ultra-high SE and EE by accommodating a large number of users in the same radio channel.

Massive MIMO systems process using a large number of antennas at the BSs, achieve an ultra-high spectral efficiency by accommodating a large number of users in the same radio channel [30]. A massive MIMO system relies on the channel information at MBS, on both uplink and downlink channels. In addition, [31] considered the uplink throughput optimization in a single massive MIMO powered cell, where an access point equipped with a large antenna array transfers energy to multiple users.

Furthermore, massive MIMO system reduces energy, focuses on the radiated energy towards the intended directions while minimizing interference, and increases the capacity due to spatial multiplexing. However, massive MIMO may require major architectural changes, in particular in the design of MBSs, and it may also lead to new types of deployments [32].

Unlike the two-dimension (2D) MIMO, the MIMO signals can also be controllable by the three-dimension (3D) space and thus called as 3D MIMO [33]. 3D MIMO with a large number of antennas and also has the potential to facilitate enhanced spatial diversity via more complicated antenna deployment.

Although massive MIMO promises unprecedented high SE and EE, the BS's circuit power consumption also increases with the number of antennas.

1.2.4 Millimeter Wave

With the recent advances in radio frequency (RF) circuits, mmwave could now be used to improve the energy efficiency of 5G networks. Millimeter wave (also called extremely high frequency) is in the band of spectrum from 30GHz to 300 GHz, which can be used for a variety of services on mobile and wireless networks, such as high speed and broad range wireless local area networks.

Millimeter waves are strongly affected by the ambient atmosphere. Rain and construction can impact performance and reduce the range and strength of the waves, so mmwaves can be blocked by physical objects. The rate trends for cellular network can be obtained with real-world building footprints; the path-loss models during the transmission process can be divided into line-of-sight (LOS) and nonline-of-sight(NLOS) due to building blockage [34].

Due to the lack of central coordination, beamforming or directional antennas are one approach for suppressing interference [35]. Recently, millimeter wave (mmWave) has been viewed as a promising technology for supporting high-speed data rate in the mobile cellular systems [36]. MmWave with directional transmissions and large bandwidths provides rich opportunities for wireless networks. Compared to the lower frequency counterpart, mmWave wireless networks experience less interference and achieve greater coverage rate [37].

Due to peculiar mmWave channel characteristics, physical layer security in mmWave systems has recently attracted much interest [38–40]. In [38], mmWave antenna subset modulation was designed to secure point-to-point communication by introducing randomness in the received constellation, which confounds the eavesdropper. The work of [39] illustrated the impacts of key factors such as large band-

width and directionality on the physical layer security in mmWave networks, and provided more opportunities and challenges in this field. In [40], it was shown that even only one eavesdropper may be able to successfully intercept highly directional mmWave transmission.

1.3 Fundamental Concepts

This section provides the fundamental concepts for the technical work presented in the following Chapters. The basic resource allocation is described for a complete understanding of the technical work in Chapters 2 and 3. The concept of physical layer security is introduced in Chapter 4.

1.3.1 Resource Allocation

In wireless communication systems, resource allocation power control and user association are two methods used to balance the load, manage resources and maximize the capacity. Power control is used to dynamically adjust the transmitted power according to some chosen criterion and user association policy is normally highly coupled with resource allocation in HetNets.

Assuming perfect CSI at the transmitter, joint optimization and analysis of transmit power control, information and power transfer scheduling are core concepts of resource allocation in WPT. There are two modes to schedule the resources in cellular networks: local resource allocation and global resource allocation.

1.3.1.1 Power Control

Optimal power strategy for energy harvesting nodes have attracted recent interest in the research community. The core concept of power control on WPT networks is minimizing the transmit powers to achieve the maximum acceptable signal-to-interference-plus-noise ratio (SINR) and received energy on the same spectral resource for each user. Now, researchers are trying to investigate power control for 5G networks.

Geometric programming techniques is a type of mathematical optimization problem characterized by objective and subject functions. Geometric program is an alternative to game theoretic approaches, which can be applied in the high or low

SINR regimes where the power control problem may be convex [41].

Power control is always associated with at least one power constraint, the most common ones being average power constraints, minimum power constraints and maximum power constraints. The average transmitted power is required to be above minimum power constraint and under maximum power constraint. Obviously, it is also important that the transmit power will be controlled based on the CSI. Maximum and minimum constraints could be imposed for several reasons: (i) from a theory perspective, it will control the power radiation to limit the interference to other users and systems; (ii) from a practical perspective, it will control the emitted power to avoid harming humans and animal. Since many components in a communication system with peak power limited [42, 43].

Generally speaking, capacity maximizing power allocation strategies are distributed by nature and difficult to achieve. Also, all the current schemes are not suitable for large networks because game theoretic algorithms represent the interfering links in the global network topology as players of a non-cooperative game, which means that it is an NP-hard problem [44]. In [45], the authors considered a dynamic policy to find the power control for HetNets with both time varying channels and wireless components. The solution involves resource allocation and routing decisions that are decoupled over the independent portions of the network.

Power control can also be interpreted as one form of energy management [46]. In 5G wireless communication systems, power control is applied to dynamically adjust the transmission power according to some chosen criterion. There are a variety of motivations behind the use of power control, including maintaining communication quality for meeting the energy and information requirements [47].

1.3.1.2 User Association Schemes

One typical example of local resource allocation was in [48], where it was proposed to collect information of the surrounding environment and then use a game theoretic model to implement correlative learning algorithms.

In [49], global resource allocation was applied to allow device-to-device (D2D) devices for cooperating with each other to reuse the resources in D2D networks.

Resource allocation for D2D communication can be treated as games. The theories behind global resource allocation provide a variety of mathematical tools to analyze the individual or group behaviors of D2D users.

However, the traditional user association rule is unsuitable for HetNets, since the transmit power variance of macro base station (MBS) and the small base station (SBS) will naturally lead to the majority of users associated with the MBS. Efforts are required to improve the rate of usage of BS.

The user-cell association scheme that may be used in such networks has a large impact on network performance. In cellular networks, user selection is usually based on the received signal strength indication values which means that the user can choose nearby BSs: users simply associate with the BS with the strongest received signal [50]. However, if a BS is already at its maximum capacity and associated with the maximum allowable number of users, it will reject further association requests and force users to select another nearby BS. In order to maximize the sum rate of all users, [51] proposed a novel distributed optimization method for dynamic user association in HetNets, which applies load balancing in multi-cell networks.

The interesting conclusion in user association is that maximizing the sum data rate of global users may result in an unfair data rate allocation, this phenomenon appears to be of similar nature with power control.

1.3.2 Physical layer Security in ad hoc networks

Physical layer security in wireless networks is important [52]. The traditional higher-layer key distribution and management may increase the burden of transmitting confidential messages in such decentralized networks. Recent developments have shown that by leveraging the randomness inherent in wireless channels, physical layer security can be a low-complexity alternative for safeguarding complex wireless networks [53]. By taking advantage of unique mmWave channel features, this paper establishes the potential of physical layer security in mmWave ad hoc networks.

Early work has studied the effects of channel fading on physical layer security,

see, e.g., [54, 55] and the references therein. The implementation of cooperative jamming and artificial noise can degrade the eavesdropper's channel and further improve secrecy [53, 56]. Recently, new network architectures and emerging transmission technologies such as heterogeneous networks (HetNets) and massive multiple-input multiple-output (MIMO) have promoted more research on physical layer security. In HetNets, dense small cells are deployed, which results in ubiquitous inter-tier and intra-tier interference. For secrecy communications at the physical layer, such interference can be utilized for confounding the eavesdroppers. In [57], spectrum allocation and transmit beamforming were designed for maximizing the secrecy rate in a two-tier HetNet. In [58], an access threshold-based secrecy mobile association policy was proposed in a K-tier HetNet. Massive MIMO uses large number of antennas to provide high array gains for legitimate receivers. It was shown in [59] that the application of random artificial noise in massive MIMO cellular networks can achieve a better performance/complexity tradeoff compared to the conventional null space based artificial noise. While the aforementioned literature has provided a solid understanding of physical layer security in the wireless systems with lower-frequency bands (sub-6 GHz), the research on mmWave secrecy communication is in its infancy.

Physical layer security in decentralized wireless networks such as sensor and ad hoc type of networks has been investigated in [60–63]. In [60], secrecy transmission capacity under connection outage and secrecy outage concerns was examined in an ad hoc network, in which both legitimate nodes and eavesdroppers are randomly distributed. In [61], the average achievable secrecy rate was examined in a three-tier sensor networks consisting of sensors, access points and sinks, and it was shown that there exists optimal number of access points for maximizing the average achievable secrecy rate. Secrecy enhancement in ad hoc networks was studied in [62], where two schemes for the generation of artificial noise were compared. In [63], relay transmission in ad hoc networks was evaluated from the perspective of security connectivity. Again, these works solely focus on the lower-frequency secrecy communications in decentralized wireless networks.

Secrecy outage of an mmWave cellular network was analyzed in [64], where authorized users and eavesdroppers were assumed to be single-omnidirectional-antenna nodes. In [65], secrecy outage of a mmWave overlaid microwave network was derived by considering a specific blockage model and assuming that mmWave channel undergoes Nakagami-m fading for tractability. In two-way amplify-and-forward MIMO relaying networks, [66] proposed mmWave secrecy beamforming schemes to maximize the secrecy sum rate.

1.4 Motivation

Energy efficiency in wireless communication networks appears to be one of the most significant and urgent issues in 5G systems. This thesis aims to study some important factors such as WPT, HetNets, Massive-MIMO and mmwave in 5G networks as well as to devise advanced techniques to enhance the performance of wireless communications systems. We begin by addressing how to allocate resources and improve security to enhance system energy efficiency and spectral efficiency. The focus of this thesis on overall resources effectiveness is mostly motivated by the need to enhance the efficiency of 5G wireless networks.

1.5 Publications

Our contributions have led to the following publications:

- **Yongxu Zhu**, Kai-Kit Wong, Yangyang Zhang, Christos Masouros, "Geometric power control for time-switching energy-harvesting two-user interference channel," published in *IEEE Trans. Veh. Technol.*, vol. 65, no. 12, pp. 97599772, Jan. 2016.

- **Yongxu Zhu**, Lifeng Wang, Kai-Kit Wong, Shi Jin, and Zhongbin Zheng, "Wireless power transfer in massive MIMO aided HetNets with user association," published in *IEEE Trans. Commun.*,vol. 64, no. 10, pp. 0090-6778, Jul. 2016.

- **Yongxu Zhu**, Lifeng Wang, Kai-Kit Wong, and Robert W. Heath, "Secure

Communications in Millimeter Wave Ad Hoc Networks," published in IEEE Trans. Wireless Commun., vol. 16, no. 5, pp. 3205-3217, May 2017.

- **Yongxu Zhu**, Lifeng Wang, Kai-Kit Wong, and Shi Jin, "System analysis of wireless power transfer in massive MIMO aided two-tier HetNets," published in *Proc. Euro. Signal Process. Conf. (EUSIPCO) - Special Session: Signal Processing in Enhancing 5G Wireless Spectrum Efficiency, Energy Efficiency and QoE*, 29 August-2 September 2016, Budapest, Hungary.

- **Yongxu Zhu**, Lifeng Wang, Kai-Kit Wong, and Robert Heath Jr., "Physical layer security in large-scale millimeter wave ad hoc networks," published in *Proc. IEEE Global Communications Conference (GLOBECOM)*, 4-8 December 2016, Washington, DC USA.

1.6 Thesis Organization

The rest of this thesis is organized as follows.

Chapter 1 introduces the background knowledge of this thesis. The technical contributions of this thesis are covered in Chapter 2 and Chapter 3.

Chapter 2 considers the geometric power control for time-switching energy-harvesting two-user interference channel. It studies the optimization of power control in two-user interference channel system where the terminals are time-switched between the communication and energy-harvesting phases.

Chapter 3 proposes a two user system analysis of WPT in massive MIMO aided HetNets. In this chapter, we explore the potential implementation of WPT in HetNets for RF energy harvesting users using massive MIMO antennas. The two user association which aim to harvest as much energy as possible and reduce the uplink path loss for enhancing their information transfer.

Chapter 4 explores the potential of physical layer security in mmWave ad hoc networks. For a large-scale mmWave ad hoc network in which eavesdroppers are randomly located, eavesdroppers can still intercept confidential messages, since they may reside in the signal beam.

Chapter 5 draws conclusions from the present work and discusses potential directions for future work.

Chapter 2

Geometric Power Control for Time-Switching Energy-Harvesting Two-User Interference Channel

2.1 Introduction

In recent years, green communications in 5G has been a main research theme in wireless communications, with an ever increasing focus on energy efficiency [9]. While power saving continues to be important, many have turned their attention to study ways to extend the lifetime of mobile terminals to realize genuine sustainability. The concept of SWIPT has thus emerged and has already opened up new opportunities and led to numerous interesting but challenging optimization problems, an energy-harvesting sensor network was investigated, in which a sensor node uses the harvested energy from the environment to generate and transmit data packets. Energy management policies that are throughput-optimal and delay-minimal were devised.

[18] studied the achievable rate-energy regions for the four possible modes of ER/IR for the two-user case. For more users, pairwise cooperation was proposed.

For complexity sake, time-switching SWIPT appears more appealing than the PS approach. Though [18] provided a useful study for time-switching SWIPT, there are further important problems that need investigating. Firstly, collaborative energy

beams may not always be possible in the interference channel. Secondly, in the interference channel, meeting the target rates at individual IRs can sometimes be much more important than maximizing their sum-rate (the latter being the focus of [18]). Most recently in [67], a block-based time-switching protocol was proposed for powering relaying transmission.

2.2 Contribution

In this chapter, we investigate the two-user interference channel where both users operate synchronously in *fixed* time-switching manner, for wireless information transfer (WIT) and WPT. Both users are subject to individual data and energy harvesting requirements, while aiming for maximizing their channel sum-rate. Assuming a fixed prescribed time-switching factor, our problem of interest is to find the optimal power control for both users to achieve this, given perfect CSI. In particular, we address this non-convex optimization problem by analyzing the geometry of the feasible region. In particular, our work differs from [18] in that the sum-rate maximization is studied with *both rate and energy harvesting constraints* whereas [18] did not have rate or energy harvesting constraints in the optimization. The inclusion of the rate and energy harvesting constraints is what makes our optimization of the users' transmit power so much more difficult compared to the ones in [18]. On the other hand, [67] studied optimization of the time-switching parameter τ for a relaying channel with WPT. Clearly, the inter-user interference aspect and the trade-off between WIT and WPT in the interference-limited environment that our work has tackled were not addressed.

The remainder of this chapter is organized as follows. Section 2.3 introduces the network model. In Section 2.4, we first present some lemmas which are key to understanding the geometric properties of the constraints for maximizing the sum-rate, and then present the optimal power allocation for the cases of rate constraints only, energy constraints only, and both data and energy constraints. Section 2.5 provides the numerical results and all the appendix in Section 6.

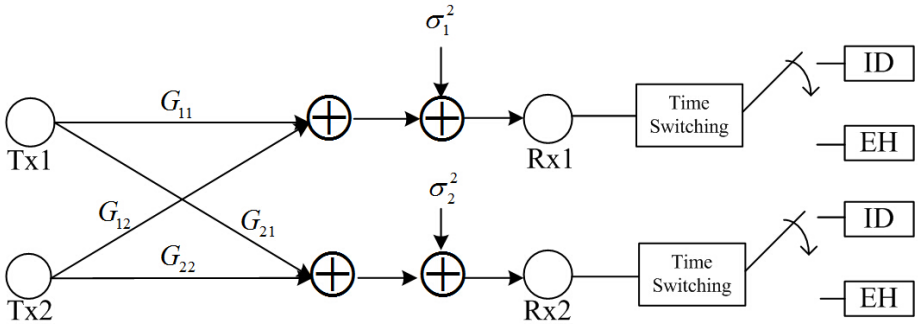

Figure 2.1: A time-switching SWIPT network model.

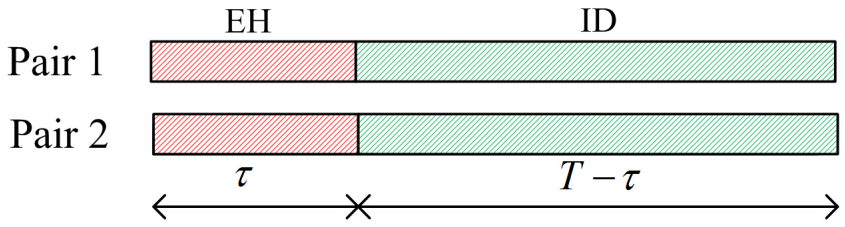

Figure 2.2: Illustration of the time switching operation.

2.3 Two-User Time-Switching SWIPT

We consider a two-user SWIPT communications network in which two transmitters communicate with their own receivers on a single radio channel over flat fading. Hence, they interfere with each other. As shown in Fig. 2.1, the considered SWIPT system operates in time switching fashion, switching between IR and ER, with τ units of time dedicated for WPT while the remaining $T-\tau$ units of time for WIT. The time-switching factor, τ, is assumed fixed and adopted by both users.

This is a crosstalk interference channel which is characterized by the two-input two-output channel gain matrix

$$\mathbf{G} = \begin{bmatrix} G_{1,1} & G_{1,2} \\ G_{2,1} & G_{2,2} \end{bmatrix}. \tag{2.1}$$

During the WIT phase, both users' receivers act as IRs, and the SINR at the nth receiver can be written as

$$\text{SINR}_n = \frac{P_n^i G_{n,n}}{\sigma_n^2 + P_m^i G_{n,m}}, \text{ for } m \neq n, \text{ and } m,n = 1,2, \tag{2.2}$$

where P_1^i and P_2^i denote, respectively, the transmit power for user 1 and user 2 in the WIT phase, and σ_n^2 denotes the noise power at receiver n. To maximize the utilization of the channel, it is customary to maximize the achievable sum-rate

$$\begin{aligned} R_{sum} &\equiv (T-\tau)(R_1+R_2), \\ &= (T-\tau)\left(\log_2(1+\mathrm{SINR}_1)+\log_2(1+\mathrm{SINR}_2)\right). \end{aligned} \tag{2.3}$$

Therefore, we have the maximization problem:

$$\max_{\boldsymbol{P}^i} \log_2(1+\mathrm{SINR}_1(\boldsymbol{P}^i))+\log_2(1+\mathrm{SINR}_2(\boldsymbol{P}^i)), \tag{2.4}$$

where $\boldsymbol{P}^i \triangleq (P_1^i, P_2^i)$, and the factor $(T-\tau)$ is removed since T and τ are constants and do not affect the optimization.

For WPT, all received powers (including the noise power) contribute to the harvested power. In particular, without loss of generality, assuming 100% harvesting efficiency, the harvested power at the receivers is, respectively, given by

$$\frac{\mathscr{W}_n}{\tau} = Y_n = P_n^e G_{n,n} + \sigma_n^2 + P_m^e G_{n,m}, \text{for } m \neq n, \text{ and } m,n = 1,2, \tag{2.5}$$

where $\mathscr{W}_n$ denotes the energy received in the entire WPT slot, and hence Y_n represents the received power, and P_n^e denotes the transmit power for user n in the WPT phase.

For the two-user interference channel, it is important to meet individual constraints and in SWIPT, it is considered that each user should be given a data constraint for WIT and a harvested energy constraint for WPT. Mathematically, we have

$$Y_1\tau \geq \underline{\mathscr{W}}_1, \tag{2.6}$$

$$Y_2\tau \geq \underline{\mathscr{W}}_2, \tag{2.7}$$

$$R_1(T-\tau) \geq \underline{\mathscr{D}}_1, \tag{2.8}$$

$$R_2(T-\tau) \geq \underline{\mathscr{D}}_2, \tag{2.9}$$

where $\underline{\mathscr{W}}_1$ and $\underline{\mathscr{W}}_2$ are the minimum target harvested energy for user 1 and user 2, respectively, and $\underline{\mathscr{D}}_1$ and $\underline{\mathscr{D}}_2$ denote the minimum target data for user 1 and user 2, respectively.

As a result, the optimization problem for the fixed time-switching SWIPT interference system over one complete WIT-WPT period can be written as

$$\begin{aligned} \max_{\boldsymbol{P}^i,\boldsymbol{P}^e} \ & R_{sum} = R_1 + R_2 \\ \text{s.t.} \ & \begin{cases} Y_1 \geq \dfrac{\underline{\mathscr{W}}_1}{\tau}, \\ Y_2 \geq \dfrac{\underline{\mathscr{W}}_2}{\tau}, \\ R_1 \geq \dfrac{\underline{\mathscr{D}}_1}{T-\tau}, \\ R_2 \geq \dfrac{\underline{\mathscr{D}}_2}{T-\tau}, \\ 0 \leq P_1^i + P_1^e \leq \bar{P}_1, \\ 0 \leq P_2^i + P_2^e \leq \bar{P}_2. \end{cases} \end{aligned} \tag{2.10}$$

where $\boldsymbol{P}^e \triangleq (P_1^e, P_2^e)$, and $\bar{P}_1$ and $\bar{P}_2$ denote the maximum permissible power for transmitter 1 and transmitter 2, respectively. Note that the peak power constraint is shared over the WIT and WPT phases. It is possible that the sum-rate can be improved if different power is allocated for the two phases. As Y_1 and Y_2 are increasing functions of P_1^e and P_2^e, respectively, if P_1^i and P_2^i are decided, then we can set $P_1^e = \bar{P}_1 - P_1^i$ and $P_2^e = \bar{P}_2 - P_2^i$, without affecting the optimality and feasibility of (2.10). Therefore, we can rewrite (2.10) as

$$\max_{\boldsymbol{P}^i,\boldsymbol{P}^e} \; R_{sum} = R_1 + R_2$$
$$\text{s.t.} \begin{cases} Y_1 \geq \frac{\mathscr{W}_1}{\tau}, \\ Y_2 \geq \frac{\mathscr{W}_2}{\tau}, \\ R_1 \geq \frac{\mathscr{D}_1}{T-\tau}, \\ R_2 \geq \frac{\mathscr{D}_2}{T-\tau}, \\ 0 \leq P_1^i \leq \bar{P}_1, \\ 0 \leq P_2^i \leq \bar{P}_2, \\ P_1^e = \bar{P}_1 - P_1^i, \\ P_2^e = \bar{P}_2 - P_2^i. \end{cases} \tag{2.11}$$

2.4 Optimal Power Control

This section uses a geometrical analysis to find the optimal power pair allocation for (2.11) in the transmit power region $\Pi = \{(P_1^i, P_2^i) | 0 \leq P_1^i \leq \bar{P}_1, 0 \leq P_2^i \leq \bar{P}_2\}$. As stated above, it suffices to obtain the optimal $\boldsymbol{P}^i \subseteq \Pi$, as $\boldsymbol{P}^e$ can be found from $\boldsymbol{P}^i$. To proceed, we have the following lemmas.

2.4.1 Lemmas

Lemma 1. *In order to maximize the system sum-rate function R_{sum}, the optimal power allocation appears at either boundary of $P_1^i = \bar{P}_1^i$ or $P_2^i = \bar{P}_2^i$, where $\bar{P}_k^i$ denotes the maximum permissible transmit power for P_k^i which is usually less than $\bar{P}_k$ because of meeting the energy harvesting constraints.*

Proof. Since the log function is a monotonically increasing function, it suffices to look at the function

$$f(\boldsymbol{P}^i) \triangleq \left(1 + \frac{P_1^i G_{1,1}}{P_2^i G_{1,2} + \sigma_1^2}\right)\left(1 + \frac{P_2^i G_{2,2}}{P_1^i G_{2,1} + \sigma_2^2}\right). \tag{2.12}$$

Given that $0 \leq P_1^i \leq \bar{P}_1^i$ and $0 \leq P_2^i \leq \bar{P}_2^i$, we proceed to analyze the maximization of f with respect to (w.r.t.) $\boldsymbol{P}^i$.

Now, treating P_2^i as *fixed*, differentiate f w.r.t. P_1^i to give

$$\frac{\partial f(\boldsymbol{P}^i)}{\partial P_1^i} = \left(\frac{G_{1,1}}{A(P_2^i)}\right)\left(1+\frac{P_2^i G_{2,2}}{B(P_1^i)}\right) - \left(\frac{G_{2,1}}{B(P_1^i)}\right)\left(\frac{P_2^i G_{2,2}}{B(P_1^i)}\right)\left(1+\frac{P_1^i G_{1,1}}{A(P_2^i)}\right), \tag{2.13}$$

where, for convenience, we have defined

$$\begin{cases} A(P_2^i) = P_2^i G_{1,2} + \sigma_1^2 > 0, \\ B(P_1^i) = P_1^i G_{2,1} + \sigma_2^2 > 0. \end{cases} \tag{2.14}$$

If we have either $\frac{\partial f(\boldsymbol{P}^i)}{\partial P_1^i} > 0$ or $\frac{\partial f(\boldsymbol{P}^i)}{\partial P_1^i} < 0$, then $f(\boldsymbol{P}^i)$ is a monotonic function, and the maximum of $f(\boldsymbol{P}^i)$ will appear at an endpoint of P_1^i, i.e., either 0 or $\bar{P}_1^i$. On the other hand, if it is possible that $\frac{\partial f(\boldsymbol{P}^i)}{\partial P_1^i} = 0$, then the maximum may occur at the P_1^i such that $\frac{\partial f(\boldsymbol{P}^i)}{\partial P_1^i} = 0$. To analyze this case, it can be easily shown that if $\frac{\partial f(\boldsymbol{P}^i)}{\partial P_1^i} = 0$, then we have

$$\frac{G_{2,1}}{B(P_1^i)}\left(1+\frac{P_1^i G_{1,1}}{A(P_2^i)}\right) - \frac{G_{1,1}}{A(P_2^i)} = \frac{G_{1,1}B(P_1^i)}{A(P_2^i)P_2^i G_{2,2}}. \tag{2.15}$$

To find out whether such P_1^i corresponds to a maximum or minimum, we obtain the second derivative $\frac{\partial^2 f(\boldsymbol{P}^i)}{\partial {P_1^i}^2}$ as

$$\frac{\partial^2 f(P_1^i, P_2^i)}{\partial {P_1^i}^2} = \frac{2P_2^i G_{2,2} G_{2,1}}{B^2(P_1^i)}\left[\frac{G_{2,1}}{B(P_1^i)}\left(1+\frac{P_1^i G_{1,1}}{A(P_2^i)}\right) - \frac{G_{1,1}}{A(P_2^i)}\right]. \tag{2.16}$$

Using (2.15) on the above, it is found that at the turning point $\frac{\partial f(\boldsymbol{P}^i)}{\partial P_1^i} = 0$, we have

$$\frac{\partial^2 f(\boldsymbol{P}^i)}{\partial {P_1^i}^2} = \frac{2G_{2,2}G_{1,1}}{A(P_2^i)B(P_1)} > 0, \tag{2.17}$$

which means that it is a minimum and $f(\boldsymbol{P}^i)$ is convex, so the maximum occurs at an endpoint of P_1^i. A similar result for P_2^i is also anticipated. Thus, we complete the proof. □

Corollary 1. *The power allocation pair $\boldsymbol{P}^i$ that maximizes the sum-rate is in the set*

Table 2.1: Attributes of the rate constraint lines.

	$\boldsymbol{l}_{R_1}$	$\boldsymbol{l}_{R_2}$
Slope	$\frac{1}{2^{\frac{\mathscr{Q}_1}{T-\tau}}-1}\left(\frac{G_{1,1}}{G_{1,2}}\right)$	$\left(2^{\frac{\mathscr{Q}_2}{T-\tau}}-1\right)\left(\frac{G_{2,1}}{G_{2,2}}\right)$
P_1^i-intercept $P_1^i\|_{(\boldsymbol{l}_R,P_2^i=0)}$ §	$\left(2^{\frac{\mathscr{Q}_1}{T-\tau}}-1\right)\frac{\sigma_1^2}{G_{1,1}}$	$-\frac{\sigma_2^2}{G_{2,1}}$
P_2^i-intercept $P_2^i\|_{(\boldsymbol{l}_R,P_1^i=0)}$	$-\frac{\sigma_1^2}{G_{1,2}}$	$\left(2^{\frac{\mathscr{Q}_2}{T-\tau}}-1\right)\frac{\sigma_2^2}{G_{2,2}}$

§Note that throughout this chapter, the notation $P|_{(\boldsymbol{l}_X,\boldsymbol{l}_Y)}$ is used to specify the value for P at the intersection point of line $\boldsymbol{l}_X$ and line $\boldsymbol{l}_Y$.

of the corner points:

$$\boldsymbol{P}^i \in \left\{(\bar{P}_1^i,0),(0,\bar{P}_2^i),(\bar{P}_1^i,\bar{P}_2^i)\right\}. \tag{2.18}$$

Proof. This is a direct result of *Lemma 1*. □

Lemma 2. *With the rate constraints, the feasible region for $\boldsymbol{P}^i$ is characterized by the half planes defined by the two straight lines on the (P_1^i,P_2^i)-plane, given by*

$$\begin{aligned}\boldsymbol{l}_{R_1}: P_2^i &= \frac{1}{2^{\frac{\mathscr{Q}_1}{T-\tau}}-1}\left(\frac{G_{1,1}}{G_{1,2}}\right)P_1^i-\frac{\sigma_1^2}{G_{1,2}},\\ \boldsymbol{l}_{R_2}: P_2^i &= \left(2^{\frac{\mathscr{Q}_2}{T-\tau}}-1\right)\left(\frac{G_{2,1}}{G_{2,2}}\right)P_1^i+\left(2^{\frac{\mathscr{Q}_2}{T-\tau}}-1\right)\frac{\sigma_2^2}{G_{2,2}}.\end{aligned} \tag{2.19}$$

In particular, the feasible region is the intersection of the lower half plane of $\boldsymbol{l}_{R_1}$ and the upper half plane of $\boldsymbol{l}_{R_2}$.

Proof. The results can be immediately obtained by manipulating the rate (or data) constraints in (2.10). The attributes of the straight lines are summarized in Table 2.1. Also, we can see that the slopes of both lines are positive; hence the angles enclosed by the straight lines and the P_1^i-axis are acute. □

Corollary 2. *The slope of $\boldsymbol{l}_{R_1}$ must be greater than the slope of $\boldsymbol{l}_{R_2}$, if problem (2.11) is feasible.*

Proof. If the slope of $\boldsymbol{l}_{R_1}$ is smaller than the slope of $\boldsymbol{l}_{R_2}$, then the intersection area will occur at the third quadrant of the (P_1^i,P_2^i)-plane, which means that the required power $\boldsymbol{P}^i$ needs to be negative. Therefore, the contrary must be true. □

Lemma 3. *The sum-rate, R_{sum}, increases along the line $\boldsymbol{l}_{R_1}$ (or $\boldsymbol{l}_{R_2}$) of increasing the transmit power P_1^i and P_2^i.*

Proof. We will focus on the proof for the sum-rate along line $\boldsymbol{l}_{R_1}$ when P_1^i increases. The proof for other results follow similarly. As we know, on line $\boldsymbol{l}_{R_1}$, $R_1 = \frac{\mathscr{D}_1}{T-\tau}$ is constant, and therefore, R_{sum} increases if R_2 increases. To see this is indeed the case, we can express P_2^i in terms of P_1^i using $\boldsymbol{l}_{R_1}$ in (2.19), and differentiate R_2 w.r.t. P_1^i, which shows

$$\frac{\partial R_2}{\partial P_1^i} = \frac{1}{\ln 2}\left(\frac{1}{\left(\frac{1}{2^{\frac{\mathscr{D}_1}{T-\tau}}-1}\left(\frac{G_{1,1}}{G_{1,2}}\right)P_1^i - \frac{\sigma_1^2}{G_{1,2}}\right)G_{2,2} + P_1^i G_{2,1} + \sigma_2^2}\right) \tag{2.20}$$

$$\times\left(\frac{\left(\frac{1}{2^{\frac{\mathscr{D}_1}{T-\tau}}-1}\left(\frac{G_{1,1}}{G_{1,2}}\right)P_1^i - \frac{\sigma_1^2}{G_{1,2}}\right)G_{2,2}G_{2,1}}{P_1^i G_{2,1} + \sigma_2^2}\right) > 0. \tag{2.21}$$

This implies that R_2 (and hence R_{sum}) is monotonic increasing in P_1^i and P_2^i along $\boldsymbol{l}_{R_1}$, which completes the proof. □

The results of *Lemma 2* and *Corollary 2* together provide the feasible region given by the rate constraints mathematically. Fig. 2.3 shows the possible feasible regions graphically. In this figure, we have used the corner point $(\bar{P}_1, \bar{P}_2)$ to characterize the possible cases in which the lines $\boldsymbol{l}_{R_1}$ and $\boldsymbol{l}_{R_1}$ may cut the box region Π. In particular, the achievable rates for $(\bar{P}_1, \bar{P}_2)$, denoted as (D_1°, D_2°) are used as the references, i.e.,

$$D_1^\circ = (T-\tau)\log_2\left(1 + \frac{\bar{P}_1 G_{1,1}}{\sigma_1^2 + \bar{P}_2 G_{1,2}}\right), \tag{2.22}$$

$$D_2^\circ = (T-\tau)\log_2\left(1 + \frac{\bar{P}_2 G_{2,2}}{\sigma_2^2 + \bar{P}_1 G_{2,1}}\right). \tag{2.23}$$

For $\boldsymbol{l}_{R_1}$, the line divides the region into $R_1 > \frac{\mathscr{D}_1}{T-\tau}$ (lower half plane) and $R_1 < \frac{\mathscr{D}_1}{T-\tau}$ (upper half plane). For the case in Fig. 2.3(b), the rate achievable by user 1 at $(\bar{P}_1, \bar{P}_2)$ appears to be in the lower half plane of $\boldsymbol{l}_{R_1}$. Therefore, it corre-

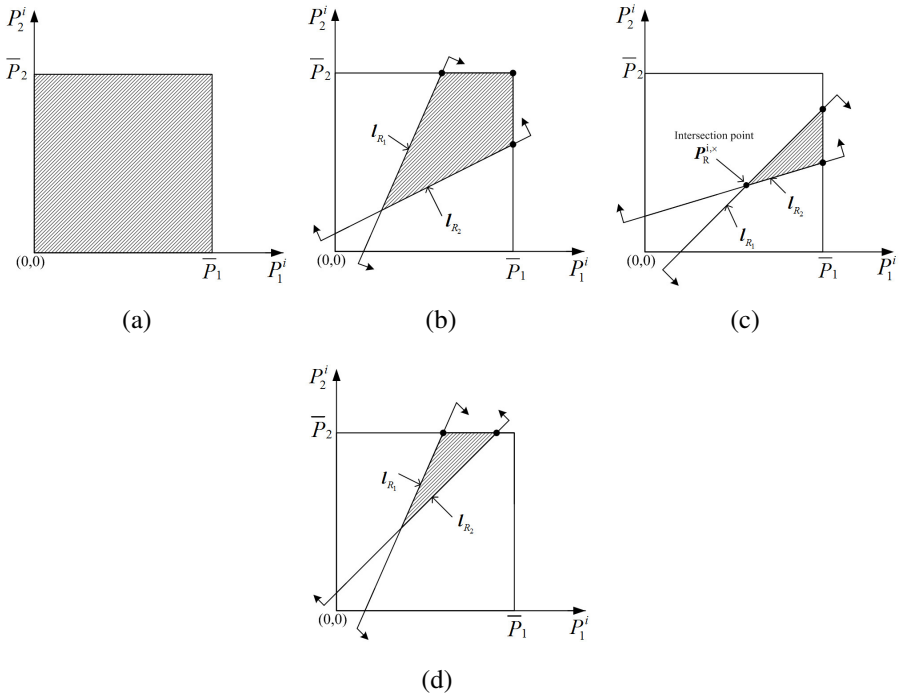

Figure 2.3: Illustration of the possible feasible regions (shaded areas) for $\boldsymbol{P}^i$ when considering the rate constraints: (a) The box region Π, with only peak power constraints and no rate constraints; (b)–(d) Π with peak power constraints and minimum rate constraints, (b) when $\mathscr{D}_1 < D_1^\circ$ and $\mathscr{D}_2 < D_2^\circ$, (c) when $\mathscr{D}_1 > D_1^\circ$ and $\mathscr{D}_2 < D_2^\circ$, and (d) when $\mathscr{D}_1 < D_1^\circ$ and $\mathscr{D}_2 > D_2^\circ$. Note that if $\mathscr{D}_1 > D_1^\circ$ and $\mathscr{D}_2 > D_2^\circ$, the intersection point will appear outside the box region Π and in this case, no power will be feasible. For the same reason, due to *Corollary 2*, this figure only illustrates the cases if the slope of $\boldsymbol{l}_{R_1}$ > the slope of $\boldsymbol{l}_{R_2}$; otherwise, the intersection point will appear in the third quadrant of the (P_1^i, P_2^i)-plane and no power will be feasible.

sponds to $D_1^\circ > \underline{\mathscr{D}}_1$. Similar arguments for $\boldsymbol{l}_{R_2}$ will indicate that in this case, it also corresponds to the fact that $D_2^\circ > \underline{\mathscr{D}}_2$. Other cases in Fig. 2.3 can also be deduced in a similar way.

Alternatively, feasibility can be understood via the intersection point of $\boldsymbol{l}_{R_1}$ and $\boldsymbol{l}_{R_2}$, denoted as $\boldsymbol{P}_{\mathrm{R}}^{i,\times} = (P_{1,\mathrm{R}}^{i,\times}, P_{2,\mathrm{R}}^{i,\times})$, which is given by

$$\begin{cases} P_{1,\mathrm{R}}^{i,\times} = \dfrac{\left(2^{\frac{\mathscr{D}_1}{T-\tau}}-1\right)\left(\left(2^{\frac{\mathscr{D}_2}{T-\tau}}-1\right)G_{1,2}\sigma_2^2 + G_{2,2}\sigma_1^2\right)}{G_{1,1}G_{2,2} - \left(2^{\frac{\mathscr{D}_1}{T-\tau}}-1\right)\left(2^{\frac{\mathscr{D}_2}{T-\tau}}-1\right)G_{2,1}G_{1,2}}, \\ P_{2,\mathrm{R}}^{i,\times} = \dfrac{\left(2^{\frac{\mathscr{D}_2}{T-\tau}}-1\right)\left(G_{1,1}\sigma_2^2 + \left(2^{\frac{\mathscr{D}_1}{T-\tau}}-1\right)G_{2,1}\sigma_1^2\right)}{G_{1,1}G_{2,2} - \left(2^{\frac{\mathscr{D}_1}{T-\tau}}-1\right)\left(2^{\frac{\mathscr{D}_2}{T-\tau}}-1\right)G_{2,1}G_{1,2}}. \end{cases} \tag{2.24}$$

Corollary 3. *To be feasible with the data/rate constraints, the intersection point* $\boldsymbol{P}_{\mathrm{R}}^{i,\times}$ *must be inside the power region* Π.

Proof. This is a direct result of *Lemma 2*. □

Lemma 4. *For the energy harvesting constraints, the feasible region for our problem is characterized by the intersection of the lower half planes of the two straight lines on the* (P_1^i, P_2^i)*-plane that are, respectively, given by*

$$\begin{cases} \boldsymbol{l}_{Y_1} : P_2^i = \left(-\dfrac{G_{1,1}}{G_{1,2}}\right) P_1^i \\ \qquad\qquad + \dfrac{1}{G_{1,2}} \left(\bar{P}_1 G_{1,1} + \bar{P}_2 G_{1,2} - \dfrac{\mathscr{W}_1}{\tau} + \sigma_1^2\right), \\ \boldsymbol{l}_{Y_2} : P_2^i = \left(-\dfrac{G_{2,1}}{G_{2,2}}\right) P_1^i \\ \qquad\qquad + \dfrac{1}{G_{2,2}} \left(\bar{P}_1 G_{2,1} + \bar{P}_2 G_{2,2} - \dfrac{\mathscr{W}_2}{\tau} + \sigma_2^2\right). \end{cases} \tag{2.25}$$

Proof. Using (2.5) with the substitution $P_1^e = \bar{P}_1 - P_1^i$ and $P_2^e = \bar{P}_2 - P_2^i$ in the energy harvesting constraints of (2.10) will result in the two straight lines (2.25). Moreover, both lines have negative slopes, which means that the angles enclosed by the lines and the P_1^i-axis are obtuse. As before, the attributes of the straight lines are provided in Table 2.2. □

In typical scenarios, we likely have the main channel gains greater than that of the crosstalk channels, i.e., $G_{1,1} > G_{1,2}$, and $G_{2,2} > G_{2,1}$. Therefore, we will have

$$\text{slope of } \boldsymbol{l}_{Y_1} = -\frac{G_{1,1}}{G_{1,2}} < -1, \tag{2.26}$$

and

$$\text{slope of } \boldsymbol{l}_{Y_2} = -\frac{G_{2,1}}{G_{2,2}} > -1 > \text{slope of } \boldsymbol{l}_{Y_1}. \tag{2.27}$$

Corollary 4. *Typically, the* P_1^i*-intercepts and* P_2^i*-intercepts for both lines* $\boldsymbol{l}_{Y_1}$ *and* $\boldsymbol{l}_{Y_2}$ *are positive, and the energy harvesting constraints are activated.*

Proof. As shown in Table II, for both $\boldsymbol{l}_{Y_1}$ and $\boldsymbol{l}_{Y_2}$, the P_1^i-intercept and P_2^i-intercept have the same polarities. That is to say, they are either both positive or both negative.

Table 2.2: Attributes of the energy harvesting constraint lines.

	$\boldsymbol{l}_{Y_1}$	$\boldsymbol{l}_{Y_2}$
Slope	$-\frac{G_{1,1}}{G_{1,2}}$	$-\frac{G_{2,1}}{G_{2,2}}$
P_1^i-intercept $P_1^i\big\vert_{(\boldsymbol{l}_Y, P_2^i=0)}$	$\frac{\bar{P}_1 G_{1,1}+\bar{P}_2 G_{1,2}-\frac{\mathscr{W}_1}{\tau}+\sigma_1^2}{G_{1,1}}$	$\frac{\bar{P}_1 G_{2,1}+\bar{P}_2 G_{2,2}-\frac{\mathscr{W}_2}{\tau}+\sigma_2^2}{G_{2,1}}$
P_2^i-intercept $P_2^i\big\vert_{(\boldsymbol{l}_Y, P_1^i=0)}$	$\frac{\bar{P}_1 G_{1,1}+\bar{P}_2 G_{1,2}-\frac{\mathscr{W}_1}{\tau}+\sigma_1^2}{G_{1,2}}$	$\frac{\bar{P}_1 G_{2,1}+\bar{P}_2 G_{2,2}-\frac{\mathscr{W}_2}{\tau}+\sigma_2^2}{G_{2,2}}$

The feasible region for $\boldsymbol{P}^i$ is the intersection of the lower half planes made by $\boldsymbol{l}_{Y_1}$ and $\boldsymbol{l}_{Y_2}$ (according to *Lemma 4*), and the box region Π due to the peak power constraints. If both of the intersects are negative, the intersection is null and the problem is infeasible, so the energy harvesting constraints are only meaningful when the P_1^i-intercept and P_2^i-intercept are both positive. □

In terms of feasibility, the intersection point of $\boldsymbol{l}_{Y_1}$ and $\boldsymbol{l}_{Y_2}$, denoted as $\boldsymbol{P}_{\mathrm{Y}}^{i,\times} = (P_{1,\mathrm{Y}}^{i,\times}, P_{2,\mathrm{Y}}^{i,\times})$, which is given by

$$\begin{aligned} P_{1,\mathrm{Y}}^{i,\times} &= \frac{G_{2,2}\left(\bar{P}_1 G_{2,1}+\bar{P}_2 G_{2,2}-\frac{\mathscr{W}_2}{\tau}+\sigma_2^2\right)}{G_{1,1}G_{2,2}-G_{1,2}G_{2,1}} \\ &\quad - \frac{G_{2,1}\left(\bar{P}_1 G_{1,1}+\bar{P}_2 G_{1,2}-\frac{\mathscr{W}_1}{\tau}+\sigma_1^2\right)}{G_{1,1}G_{2,2}-G_{1,2}G_{2,1}}, \end{aligned} \tag{2.28}$$

$$\begin{aligned} P_{2,\mathrm{Y}}^{i,\times} &= \frac{G_{1,1}\left(\bar{P}_1 G_{1,1}+\bar{P}_2 G_{1,2}-\frac{\mathscr{W}_1}{\tau}+\sigma_1^2\right)}{G_{1,1}G_{2,2}-G_{1,2}G_{2,1}} \\ &\quad - \frac{G_{1,2}\left(\bar{P}_1 G_{2,1}+\bar{P}_2 G_{2,2}-\frac{\mathscr{W}_2}{\tau}+\sigma_2^2\right)}{G_{1,1}G_{2,2}-G_{1,2}G_{2,1}}. \end{aligned} \tag{2.29}$$

plays an important role. See caption of Fig. 2.4.

Fig. 2.4 depicts the possible feasible regions of $\boldsymbol{P}^i$ as far as the energy harvesting constraints are concerned.

Lemma 5. *Along the energy harvesting constraint lines $\boldsymbol{l}_{Y_1}$ and $\boldsymbol{l}_{Y_2}$ specified in Lemma 4, the maximum sum-rate, R_{sum}, occurs at the endpoints within the power constraints Π.*

Proof. We will focus on line $\boldsymbol{l}_{Y_1}$ but the proof follows naturally for $\boldsymbol{l}_{Y_2}$. On $\boldsymbol{l}_{Y_1}$,

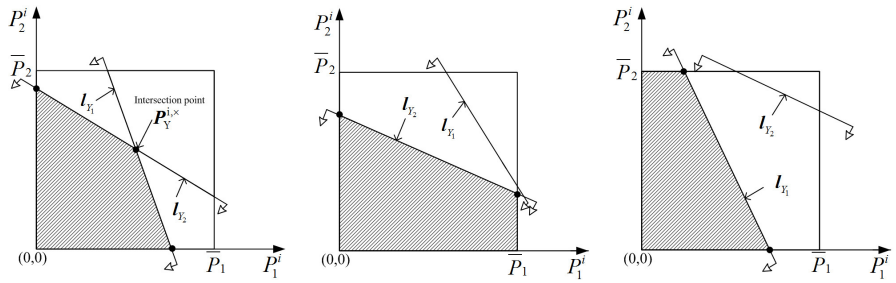

Figure 2.4: Illustration of the possible feasible regions (shaded areas) for $\boldsymbol{P}^i$ when considering both the energy harvesting constraints and the peak power constraints Π, assuming the slope of $\boldsymbol{l}_{Y_2}$ > that of $\boldsymbol{l}_{Y_1}$ (the typical situation). In (a), $\boldsymbol{P}_{\mathrm{Y}}^{i,\times}$ occurs inside Π, or $0 \le P_{1,\mathrm{Y}}^{i,\times} \le \bar{P}_1$ and $0 \le P_{2,\mathrm{Y}}^{i,\times} \le \bar{P}_2$, while in (b), $\boldsymbol{P}_{\mathrm{Y}}^{i,\times}$ is outside Π on the right, i.e., $P_{1,\mathrm{Y}}^{i,\times} > \bar{P}_1$ and $0 \le P_{2,\mathrm{Y}}^{i,\times} \le \bar{P}_2$. For (c), $\boldsymbol{P}_{\mathrm{Y}}^{i,\times}$ is above Π or $0 \le P_{1,\mathrm{Y}}^{i,\times} \le \bar{P}_1$ and $P_{2,\mathrm{Y}}^{i,\times} > \bar{P}_2$. The case that the slope of $\boldsymbol{l}_{Y_2}$ < that of $\boldsymbol{l}_{Y_1}$ is also possible, and the analysis is similar. In the case that $\boldsymbol{P}_{\mathrm{Y}}^{i,\times}$ is far away from Π, the problem is infeasible.

using (2.25), we can write P_2^i in terms of P_1^i. Then as in the proof of *Lemma 1*, we substitute such $\boldsymbol{P}^i$ into f, and differentiate it w.r.t. P_1^i to give

$$\frac{\partial f(\boldsymbol{P}^i)}{\partial P_1^i} = \frac{G_{1,1}}{M_3}\left(\frac{G_{2,2}M_1(P_1^i)}{M_2(P_1^i)}+1\right)\left(\frac{G_{1,1}P_1^i}{M_3}+1\right) - \frac{G_{2,2}}{M_2(P_1^i)}\left(\frac{G_{2,1}M_1(P_1^i)}{M_2(P_1^i)}+\frac{G_{1,1}}{G_{1,2}}\right)\left(\frac{G_{1,1}P_1^i}{M_3}+1\right), \quad (2.30)$$

where

$$\begin{aligned} M_1 &= \frac{1}{G_{1,2}}\left(G_{1,1}\bar{P}_1 + G_{1,2}\bar{P}_2 - G_{1,1}P_1^i - \frac{\cancel{W}_1}{\tau} + \sigma_2^2\right) > 0, \\ M_2 &= \sigma_2^2 + G_{2,1}P_1^i > 0, \\ M_3 &= \sigma_1^2 + G_{1,2}M_1 > 0. \end{aligned} \quad (2.31)$$

If $\frac{\partial f(\boldsymbol{P}^i)}{\partial P_1^i}$ is either always positive or always negative, then f is monotonic and the result of this lemma follows. Otherwise, we need to show that f is convex. To do so, we first obtain the condition for the turning point, $\frac{\partial f(\boldsymbol{P}^i)}{\partial P_1^i} = 0$, giving

$$\frac{G_{1,1}^2}{M_3^2}\left(\frac{G_{2,2}M_1}{M_2}+1\right) - \frac{G_{2,2}G_{1,1}}{M_2M_3}\left(\frac{G_{2,1}M_1}{M_2}+\frac{G_{1,1}}{G_{1,2}}\right) = 0. \quad (2.32)$$

Next, we get the second-order derivative of f at $\frac{\partial f(\boldsymbol{P}^i)}{\partial P_1^i} = 0$ by deriving

$$\frac{\partial^2 f(\boldsymbol{P}^i)}{\partial {P_1^i}^2} = 2\left(\frac{G_{1,1}P_1}{M_3}+1\right) \times \left[\frac{G_{1,1}^2}{M_2^2}\left(\frac{G_{2,2}M_1}{M_2}+1\right) - \frac{G_{2,2}G_{1,1}}{M_2M_3}\left(\frac{G_{2,1}M_1}{M_2}+\frac{G_{1,1}}{G_{1,2}}\right) + \frac{G_{2,1}G_{2,2}}{M_2^2}\left(\frac{G_{2,1}M_1}{M_2}+\frac{G_{1,1}}{G_{1,2}}\right)\right]. \tag{2.33}$$

Now, using (2.32) in the above, we can see that at the turning point, $\frac{\partial f(\boldsymbol{P}^i)}{\partial P_1^i} = 0$, we have

$$\frac{\partial^2 f(\boldsymbol{P}^i)}{\partial {P_1^i}^2} = 2\left(\frac{G_{1,1}P_1}{M_3}+1\right)\frac{G_{2,1}G_{2,2}}{M_2^2}\left(\frac{G_{2,1}M_1}{M_2}+\frac{G_{1,1}}{G_{1,2}}\right) > 0, \tag{2.34}$$

which shows that f (and hence the sum-rate) is convex over line $\boldsymbol{l}_{Y_1}$. This concludes that the maximum sum-rate occurs at the endpoints of $\boldsymbol{l}_{Y_1}$ over Π, which completes the proof. □

2.4.2 With Data/Rate Constraints Only

Now, we derive the optimal power control according to the three possible scenarios in Fig. 2.3. According to *Lemma 3*, for the maximization of sum-rate, the optimal power control will appear at the edges of the box Π. In the following, we will give the optimal power control, $\boldsymbol{P}^i_{\text{opt}} = (P^i_{1,\text{opt}}, P^i_{2,\text{opt}})$, for maximizing the sum-rate with the rate constraints.

2.4.2.1 Scenario 1 (see Fig. 2.3(b))

In this case, the problem is feasible and $\boldsymbol{P}^{i,\times}_{\text{R}}$ occurs within the permissible region Π. As shown in *Lemma 3*, the optimal $\boldsymbol{P}^i_{\text{opt}}$ for maximizing the sum-rate occurs at the edges of the box Π, $P_1^i = \bar{P}_1$ or $P_2^i = \bar{P}_2$. Because of the rate constraints, there are two intersections, one for $\boldsymbol{l}_{R_1}$ and $P_2^i = \bar{P}_2$ in which case we denote

$$P_1^i = P_1^i\big|_{(\boldsymbol{l}_{R_1}, P_2^i=\bar{P}_2)} = \frac{\left(2^{\frac{\mathscr{Q}_1}{T-\tau}}-1\right)}{G_{1,1}}\left(G_{1,2}\bar{P}_2+\sigma_1^2\right), \tag{2.35}$$

and another one for $\boldsymbol{l}_{R_2}$ and $P_1^i = \bar{P}_1$ where

$$P_2^i = P_2^i\big|_{(\boldsymbol{l}_{R_2}, P_1^i = \bar{P}_1)} = \frac{\left(2^{\frac{\mathscr{D}_2}{T-\tau}} - 1\right)}{G_{2,2}} \left(G_{2,1}\bar{P}_1 + \sigma_2^2\right). \tag{2.36}$$

Furthermore, from *Corollary 1*, we know that not only does the optimal $\boldsymbol{P}_{\text{opt}}^i$ occur at the edges, it occurs at an endpoint of the feasible edges. In other words, we have

$$\boldsymbol{P}_{\text{opt}}^i = \arg \max_{\boldsymbol{P}^i \in \left\{ \begin{array}{c} (\bar{P}_1, \bar{P}_2), \\ \left(\bar{P}_1, P_2^i\big|_{(\boldsymbol{l}_{R_2}, P_1^i = \bar{P}_1)}\right), \\ \left(P_1^i\big|_{(\boldsymbol{l}_{R_1}, P_2^i = \bar{P}_2)}, \bar{P}_2\right) \end{array} \right\}} R_{sum}(\boldsymbol{P}^i). \tag{2.37}$$

2.4.2.2 Scenario 2 (see Fig. 2.3(c))

As shown, in this case, both lines $\boldsymbol{l}_{R_1}$ and $\boldsymbol{l}_{R_2}$ intersect on $P_1^i = \bar{P}_1$. As such,

$$\boldsymbol{P}_{\text{opt}}^i = \arg \max_{\boldsymbol{P}^i \in \left\{ \begin{array}{c} \left(\bar{P}_1, P_2^i\big|_{(\boldsymbol{l}_{R_1}, P_1^i = \bar{P}_1)}\right), \\ \left(\bar{P}_1, P_2^i\big|_{(\boldsymbol{l}_{R_2}, P_1^i = \bar{P}_1)}\right) \end{array} \right\}} R_{sum}(\boldsymbol{P}^i), \tag{2.38}$$

where

$$P_2^i\big|_{(\boldsymbol{l}_{R_1}, P_1^i = \bar{P}_1)} = \frac{1}{G_{1,2}} \left(\frac{G_{1,1}\bar{P}_1}{2^{\frac{\mathscr{D}_1}{T-\tau}} - 1} - \sigma_1^2 \right). \tag{2.39}$$

2.4.2.3 Scenario 3 (see Fig. 2.3(d))

Another possible situation is that both the lines $\boldsymbol{l}_{R_1}$ and $\boldsymbol{l}_{R_2}$ intersect on $P_2^i = \bar{P}_2$. As such, the optimal $\boldsymbol{P}_{\text{opt}}^i$ can be found by

$$\boldsymbol{P}_{\text{opt}}^i = \arg \max_{\boldsymbol{P}^i \in \left\{ \begin{array}{c} \left(P_1^i\big|_{(\boldsymbol{l}_{R_1}, P_2^i = \bar{P}_2)}, \bar{P}_2\right), \\ \left(P_1^i\big|_{(\boldsymbol{l}_{R_2}, P_2^i = \bar{P}_2)}, \bar{P}_2\right) \end{array} \right\}} R_{sum}(\boldsymbol{P}^i), \tag{2.40}$$

where

$$P_1^i\big|_{(\boldsymbol{l}_{R_2}, P_2^i = \bar{P}_2)} = \frac{1}{G_{2,1}} \left(\frac{G_{2,2}\bar{P}_2}{2^{\frac{\mathscr{D}_2}{T-\tau}} - 1} - \sigma_2^2 \right). \tag{2.41}$$

2.4.3 With Energy Harvesting Constraints Only

The results in *Lemma 5* and the intersection point $\boldsymbol{P}_{\mathrm{Y}}^{i,\times}$ will be useful in determining the optimal $\boldsymbol{P}_{\mathrm{opt}}^{i}$ with the energy harvesting constraints, which we detail below.

2.4.3.1 Scenario 1 (see Fig. 2.4(a))

When the point of intersection $\boldsymbol{P}_{\mathrm{Y}}^{i,\times}$ is inside the box region Π, two points are of interest. According to Fig. 2.4(a), the first one is the intersection point between line $\boldsymbol{l}_{Y_1}$ and line $P_2^i = 0$, denoting as $(P_1^i\big|_{(\boldsymbol{l}_{Y_1}, P_2^i=0)}, 0)$, and another one is the intersection point between $\boldsymbol{l}_{Y_2}$ and line $P_1^i = 0$, or $(0, P_2^i\big|_{(\boldsymbol{l}_{Y_2}, P_1^i=0)})$, where

$$P_1^i\big|_{(\boldsymbol{l}_{Y_1}, P_2^i=0)} = \frac{1}{G_{1,1}}\left(\bar{P}_1 G_{1,1} + \bar{P}_2 G_{1,2} - \frac{\mathscr{W}_1}{\tau} + \sigma_1^2\right), \tag{2.42}$$

and

$$P_2^i\big|_{(\boldsymbol{l}_{Y_2}, P_1^i=0)} = \frac{1}{G_{2,2}}\left(\bar{P}_1 G_{2,1} + \bar{P}_2 G_{2,2} - \frac{\mathscr{W}_2}{\tau} + \sigma_2^2\right). \tag{2.43}$$

Using *Lemma 5*, the optimal $\boldsymbol{P}_{\mathrm{opt}}^{i}$ can thus be found by

$$\boldsymbol{P}_{\mathrm{opt}}^{i} = \arg \max_{\boldsymbol{P}^i \in \left\{ \begin{array}{c} (P_{1,\mathrm{Y}}^{i,\times}, P_{2,\mathrm{Y}}^{i,\times}), \\ \left(P_1^i\big|_{(\boldsymbol{l}_{Y_1}, P_2^i=0)}, 0\right), \\ \left(0, P_2^i\big|_{(\boldsymbol{l}_{Y_2}, P_1^i=0)}\right) \end{array} \right\}} R_{sum}(\boldsymbol{P}^i). \tag{2.44}$$

However, Fig. 2.4(a) illustrates only one of the many possibilities. In fact, $\boldsymbol{l}_{Y_2}$ may cut the top side of Π instead of the left side. In this case, the point of interest will be the intersection point between $\boldsymbol{l}_{Y_2}$ and line $P_2^i = \bar{P}_2$ but not the line $P_1^i = 0$. Specifically, this will happen if $P_2^i\big|_{(\boldsymbol{l}_{Y_2}, P_1^i=0)} > \bar{P}_2$. Moreover, from *Corollary 1*, the point $(0, \bar{P}_2)$ is now feasible and has a higher sum-rate than any other feasible point, and hence is the optimal power control solution. Similarly, $\boldsymbol{l}_{Y_1}$ may cut the right side of Π instead of the bottom side, and we can have similar consideration to have the optimal solution $(\bar{P}_1, 0)$.

To account for the above, the optimal power control solution in (2.44) can be

extended to

$$\boldsymbol{P}^{i}_{\text{opt}} = \arg \max_{\boldsymbol{P}^{i} \in \left\{ \begin{array}{c} (P^{i,\times}_{1,\text{Y}}, P^{i,\times}_{2,\text{Y}}), \\ \left(\min\left\{\bar{P}_1,\, P^{i}_{1}\big|_{(\boldsymbol{l}_{Y_1}, P^{i}_{2}=0)}\right\}, 0\right), \\ \left(0, \min\left\{\bar{P}_2,\, P^{i}_{2}\big|_{(\boldsymbol{l}_{Y_2}, P^{i}_{1}=0)}\right\}\right) \end{array} \right\}} R_{sum}(\boldsymbol{P}^{i}). \tag{2.45}$$

Notice also that the illustration in Fig. 2.4 or the above analysis has assumed that the slope of $\boldsymbol{l}_{Y_1}$ < that of $\boldsymbol{l}_{Y_2}$. If the slope of $\boldsymbol{l}_{Y_1}$ > that of $\boldsymbol{l}_{Y_2}$, similar analysis can be carried out. Hence, we have the generalized result in (2.46) (see top of the page).

$$\boldsymbol{P}^{i}_{\text{opt}} = \begin{cases} \arg\max\limits_{\boldsymbol{P}^{i} \in \left\{ \begin{array}{c} (P^{i,\times}_{1,\text{Y}}, P^{i,\times}_{2,\text{Y}}), \\ \left(\min\left\{\bar{P}_1,\, P^{i}_{1}\big|_{(\boldsymbol{l}_{Y_1}, P^{i}_{2}=0)}\right\}, 0\right), \\ \left(0, \min\left\{\bar{P}_2,\, P^{i}_{2}\big|_{(\boldsymbol{l}_{Y_2}, P^{i}_{1}=0)}\right\}\right) \end{array} \right\}} R_{sum}(\boldsymbol{P}^{i}) & \text{if the slope of } \boldsymbol{l}_{Y_1} < \text{that of } \boldsymbol{l}_{Y_2}, \\ \arg\max\limits_{\boldsymbol{P}^{i} \in \left\{ \begin{array}{c} (P^{i,\times}_{1,\text{Y}}, P^{i,\times}_{2,\text{Y}}), \\ \left(\min\left\{\bar{P}_1,\, P^{i}_{1}\big|_{(\boldsymbol{l}_{Y_2}, P^{i}_{2}=0)}\right\}, 0\right), \\ \left(0, \min\left\{\bar{P}_2,\, P^{i}_{2}\big|_{(\boldsymbol{l}_{Y_1}, P^{i}_{1}=0)}\right\}\right) \end{array} \right\}} R_{sum}(\boldsymbol{P}^{i}) & \text{if the slope of } \boldsymbol{l}_{Y_1} \geq \text{that of } \boldsymbol{l}_{Y_2}, \end{cases} \tag{2.46}$$

2.4.3.2 Scenario 2 (see Fig. 2.4(b))

This scenario considers that the intersection point $\boldsymbol{P}^{i,\times}_{\text{Y}}$ is outside and on the right side of Π. With the assumption that the slope of $\boldsymbol{l}_{Y_1}$ < the slope of $\boldsymbol{l}_{Y_2}$, line $\boldsymbol{l}_{Y_2}$ solely determines the feasible region and there are two possible cases. In the first case, $\boldsymbol{l}_{Y_2}$ cuts $P^{i}_{1} = \bar{P}_1$ and $P^{i}_{1} = 0$ to have the intersection points $(\bar{P}_1, P^{i}_{2}\big|_{(\boldsymbol{l}_{Y_2}, P^{i}_{1}=\bar{P}_1)})$, and $(0, P^{i}_{2}\big|_{(\boldsymbol{l}_{Y_2}, P^{i}_{1}=0)})$, respectively. Therefore, using *Corollary 1* again, the points of interest for maximizing the sum-rate will be $(\bar{P}_1, 0)$ and $(0, P^{i}_{2}\big|_{(\boldsymbol{l}_{Y_2}, P^{i}_{1}=0)})$. Alternatively, it may be possible that $\boldsymbol{l}_{Y_2}$ cuts $P^{i}_{1} = \bar{P}_1$ and $P^{i}_{2} = \bar{P}_2$. In this case, the points of interests for maximizing the sum-rate become $(\bar{P}_1, 0)$ and $(0, \bar{P}_2)$. Summarizing both gives the optimal $\boldsymbol{P}^{i}_{\text{opt}}$ as

$$\boldsymbol{P}^{i}_{\text{opt}} = \arg \max_{\boldsymbol{P}^{i} \in \left\{ \begin{array}{c} (\bar{P}_1, 0), \\ \left(0, \min\left\{\bar{P}_2,\, P^{i}_{2}\big|_{(\boldsymbol{l}_{Y_2}, P^{i}_{1}=0)}\right\}\right) \end{array} \right\}} R_{sum}(\boldsymbol{P}^{i}). \tag{2.47}$$

As before, after including the case that the slope of $\boldsymbol{l}_{Y_1} \geq$ that of $\boldsymbol{l}_{Y_2}$, the result can be generalized to (2.48).

$$\boldsymbol{P}^i_{\text{opt}} = \begin{cases} \arg\max\limits_{\boldsymbol{P^i} \in \left\{ \begin{array}{c} (\bar{P}_1, 0), \\ \left(0, \min\left\{\bar{P}_2,\, P_2^i\big|_{(\boldsymbol{l}_{Y_2}, P_1^i=0)}\right\}\right) \end{array} \right\}} R_{sum}(\boldsymbol{P}^i) & \text{if the slope of } \boldsymbol{l}_{Y_1} < \text{that of } \boldsymbol{l}_{Y_2}, \\ \arg\max\limits_{\boldsymbol{P^i} \in \left\{ \begin{array}{c} (\bar{P}_1, 0), \\ \left(0, \min\left\{\bar{P}_2,\, P_2^i\big|_{(\boldsymbol{l}_{Y_1}, P_1^i=0)}\right\}\right) \end{array} \right\}} R_{sum}(\boldsymbol{P}^i) & \text{if the slope of } \boldsymbol{l}_{Y_1} \geq \text{that of } \boldsymbol{l}_{Y_2}, \end{cases} \tag{2.48}$$

2.4.3.3 Scenario 3 (see Fig. 2.4(c))

This scenario is very similar to Scenario 2 above except now that line $\boldsymbol{l}_{Y_1}$ determines the feasible region and that the intersection $\boldsymbol{P}^{i,\times}_{\text{Y}}$ is located at the top or left side of Π. One possibility is that $\boldsymbol{l}_{Y_1}$ cuts $P_2^i = 0$ and $P_2^i = \bar{P}_2$, which together with *Corollary 1* states that the optimal power control is $\boldsymbol{P}^i_{\text{opt}} = (0, \bar{P}_2)$. Another possible situation is that $\boldsymbol{l}_{Y_1}$ cuts $P_2^i = 0$ and $P_1^i = 0$. In this case, the optimal power control solution should be decided between $(P_1^i\big|_{(\boldsymbol{l}_{Y_1}, P_2^i=0)}, 0)$ and $(0, P_2^i\big|_{(\boldsymbol{l}_{Y_1}, P_1^i=0)})$. As such, combining the two cases, we have

$$\boldsymbol{P}^i_{\text{opt}} = \arg \max_{\boldsymbol{P^i} \in \left\{ \begin{array}{c} \left(P_1^i\big|_{(\boldsymbol{l}_{Y_1}, P_2^i=0)}, 0\right), \\ \left(0, \min\left\{\bar{P}_2,\, P_2^i\big|_{(\boldsymbol{l}_{Y_1}, P_1^i=0)}\right\}\right) \end{array} \right\}} R_{sum}(\boldsymbol{P}^i). \tag{2.49}$$

This result can also further be generalized to (2.50).

$$\boldsymbol{P}^i_{\text{opt}} = \begin{cases} \arg\max\limits_{\boldsymbol{P^i} \in \left\{ \begin{array}{c} \left(P_1^i\big|_{(\boldsymbol{l}_{Y_1}, P_2^i=0)}, 0\right), \\ \left(0, \min\left\{\bar{P}_2,\, P_2^i\big|_{(\boldsymbol{l}_{Y_1}, P_1^i=0)}\right\}\right) \end{array} \right\}} R_{sum}(\boldsymbol{P}^i) & \text{if the slope of } \boldsymbol{l}_{Y_1} < \text{that of } \boldsymbol{l}_{Y_2}, \\ \arg\max\limits_{\boldsymbol{P^i} \in \left\{ \begin{array}{c} \left(P_1^i\big|_{(\boldsymbol{l}_{Y_2}, P_2^i=0)}, 0\right), \\ \left(0, \min\left\{\bar{P}_2,\, P_2^i\big|_{(\boldsymbol{l}_{Y_2}, P_1^i=0)}\right\}\right) \end{array} \right\}} R_{sum}(\boldsymbol{P}^i) & \text{if the slope of } \boldsymbol{l}_{Y_1} \geq \text{that of } \boldsymbol{l}_{Y_2}, \end{cases} \tag{2.50}$$

2.4.4 With Both Data and Energy Harvesting Constraints

Here, we consider the most general case where both the rate and energy harvesting constraints are present in maximizing the sum-rate. As worked out in the above for the date-only or energy-harvesting-only constraints cases, it becomes a matter of

sorting out the feasible region (i.e., the intersection region of *Lemma 2*, *Lemma 4* and Π) and within which identify the point of power allocation $\boldsymbol{P}^i$ that delivers the maximum sum-rate. From Section III-B, we know that first the slope of $\boldsymbol{l}_{R_1}$ must be greater than that of $\boldsymbol{l}_{R_2}$ to be feasible, and that the intersection point $\boldsymbol{P}_{\mathrm{R}}^{i,\times}$ must be inside Π. Also, there will be three possible cases of how the feasible region is made out, as far as the data rate constraints are concerned. On the other hand, it is known from Section III-C that in the case of the energy harvesting constraints, there will be 8, 4 and 4 possible cases for Scenario 1, 2 and 3, respectively. Actually, altogether, there are more than 48 possible shapes of the feasible region depending upon how the lines combine within Π, if both rate and energy harvesting constraints are considered.[1]

To begin our analysis, the following points are of interest:

$$\mathsf{R}_{1,|} = \left(\bar{P}_1, P_2|_{(\boldsymbol{l}_{R_1}, P_1^i=\bar{P}_1)}\right), \tag{2.51}$$

$$\mathsf{R}_{1,-} = \left(P_1|_{(\boldsymbol{l}_{R_1}, P_2^i=\bar{P}_2)}, \bar{P}_2\right), \tag{2.52}$$

$$\mathsf{R}_{2,|} = \left(\bar{P}_1, P_2|_{(\boldsymbol{l}_{R_2}, P_1^i=\bar{P}_1)}\right), \tag{2.53}$$

$$\mathsf{R}_{2,-} = \left(P_1|_{(\boldsymbol{l}_{R_2}, P_2^i=\bar{P}_2)}, \bar{P}_2\right), \tag{2.54}$$

$$\mathsf{Y}_{1,|} = \left(\bar{P}_1, P_2|_{(\boldsymbol{l}_{Y_1}, P_1^i=\bar{P}_1)}\right), \tag{2.55}$$

$$\mathsf{Y}_{1,-} = \left(P_1|_{(\boldsymbol{l}_{Y_1}, P_2^i=\bar{P}_2)}, \bar{P}_2\right), \tag{2.56}$$

$$\mathsf{Y}_{2,|} = \left(\bar{P}_1, P_2|_{(\boldsymbol{l}_{Y_2}, P_1^i=\bar{P}_1)}\right), \tag{2.57}$$

$$\mathsf{Y}_{2,-} = \left(P_1|_{(\boldsymbol{l}_{Y_2}, P_2^i=\bar{P}_2)}, \bar{P}_2\right). \tag{2.58}$$

The above points basically mark the locations where lines $\boldsymbol{l}_{R_1}$, $\boldsymbol{l}_{R_2}$, $\boldsymbol{l}_{Y_1}$ and $\boldsymbol{l}_{Y_2}$ cut on the lines $P_1^i = \bar{P}_1$ and $P_2^i = \bar{P}_2$. The points may appear on the edges of the box Π or sometimes outside Π. Furthermore, there are five points inside Π that are important. Four of those are the intersection points among the four constraint lines, which we

[1] The actual total number of combinations is 76. For details, see Appendix I.

write them as

$$\begin{aligned}\mathsf{RY}_{1,1} &= \left(P_1|_{(\boldsymbol{l}_{R_1},\boldsymbol{l}_{Y_1})}, P_2|_{(\boldsymbol{l}_{R_1},\boldsymbol{l}_{Y_1})}\right) \\ &= \left(\frac{\left(2^{\frac{1}{T-\tau}}-1\right)\frac{\mathscr{W}_1}{\tau}}{G_{1,1}2^{\frac{1}{T-\tau}}}, \frac{\frac{\mathscr{W}_1}{\tau}-\sigma_1^2 2^{\frac{\mathscr{D}_1}{T-\tau}}}{G_{1,2}2^{\frac{\mathscr{D}_1}{T-\tau}}}\right),\end{aligned} \tag{2.59}$$

$$\begin{aligned}\mathsf{RY}_{2,1} &= \left(P_1|_{(\boldsymbol{l}_{R_2},\boldsymbol{l}_{Y_1})}, P_2|_{(\boldsymbol{l}_{R_2},\boldsymbol{l}_{Y_1})}\right) \\ &= \Bigg(\frac{G_{2,2}\left(\frac{\mathscr{W}_1}{\tau}-\sigma_1^2\right)-G_{1,2}\left(2^{\frac{\mathscr{D}_2}{T-\tau}}-1\right)\sigma_2^2}{G_{1,1}G_{2,2}+G_{1,2}G_{2,1}\left(2^{\frac{\mathscr{D}_2}{T-\tau}}-1\right)}, \\ &\quad \frac{\left(2^{\frac{\mathscr{D}_2}{T-\tau}}-1\right)\left[G_{2,1}\left(\frac{\mathscr{W}_1}{\tau}-\sigma_1^2\right)+G_{1,1}\sigma_2^2\right]}{G_{1,1}G_{2,2}+G_{1,2}G_{2,1}\left(2^{\frac{\mathscr{D}_2}{T-\tau}}-1\right)}\Bigg),\end{aligned} \tag{2.60}$$

$$\begin{aligned}\mathsf{RY}_{1,2} &= \left(P_1|_{(\boldsymbol{l}_{R_1},\boldsymbol{l}_{Y_2})}, P_2|_{(\boldsymbol{l}_{R_1},\boldsymbol{l}_{Y_2})}\right) \\ &= \Bigg(\frac{\left(2^{\frac{\mathscr{D}_1}{T-\tau}}-1\right)\left[G_{1,2}\left(\frac{\mathscr{W}_2}{\tau}-\sigma_2^2\right)+G_{2,2}\sigma_1^2\right]}{G_{1,1}G_{2,2}+G_{1,2}G_{2,1}\left(2^{\frac{\mathscr{D}_1}{T-\tau}}-1\right)},\end{aligned} \tag{2.61}$$

$$\frac{G_{1,1}\left(\frac{\mathscr{W}_2}{\tau}-\sigma_2^2\right)-G_{2,1}\left(2^{\frac{\mathscr{D}_1}{T-\tau}}-1\right)\sigma_1^2}{G_{1,1}G_{2,2}+G_{1,2}G_{2,1}\left(2^{\frac{\mathscr{D}_1}{T-\tau}}-1\right)}\Bigg), \tag{2.62}$$

and

$$\begin{aligned}\mathsf{RY}_{2,2} &= \left(P_1|_{(\boldsymbol{l}_{R_2},\boldsymbol{l}_{Y_2})}, P_2|_{(\boldsymbol{l}_{R_2},\boldsymbol{l}_{Y_2})}\right) \\ &= \left(\frac{\frac{\mathscr{W}_2}{\tau}-\sigma_2^2 2^{\frac{\mathscr{D}_2}{T-\tau}}}{G_{2,1}2^{\frac{2}{T-\tau}}}, \frac{\left(2^{\frac{\mathscr{D}_2}{T-\tau}}-1\right)\frac{\mathscr{W}_2}{\tau}}{G_{2,2}2^{\frac{\mathscr{D}_2}{T-\tau}}}\right).\end{aligned} \tag{2.63}$$

Lastly, the intersection point $\boldsymbol{P}_{\mathrm{Y}}^{i,\times}$ is particularly useful, as we will use its location to analyze the optimal power allocation, $\boldsymbol{P}_{\mathrm{opt}}^{i}$, just like what we did in Section III-B.

In the following, we will study the optimal power allocation $\boldsymbol{P}_{\mathrm{opt}}^{i}$ by consider-

ing three possible scenarios based on where $\boldsymbol{P}_{\mathrm{Y}}^{i,\times}$ would locate. The first scenario (i) investigates the case when $\boldsymbol{P}_{\mathrm{Y}}^{i,\times}$ appears inside Π, while scenario (ii) considers the case when $\boldsymbol{P}_{\mathrm{Y}}^{i,\times}$ is outside and on the right of Π, and scenario (iii) looks into the case when $\boldsymbol{P}_{\mathrm{Y}}^{i,\times}$ is at the top or left side of Π. Each of the scenarios will be discussed next. Also, notice that in order for the problem to be feasible, the intersection of the regions specified in *Lemma 2* and *Lemma 4* must not be empty, which we will assume when we proceed. In addition, for convenience, we will assume that the slope of $\boldsymbol{l}_{Y_1}$ is less than that of $\boldsymbol{l}_{Y_2}$, but our analysis can be easily extended by swapping the indices corresponding to lines $\boldsymbol{l}_{Y_1}$ and $\boldsymbol{l}_{Y_2}$.

2.4.4.1 Scenario (i)

Even within the case where $\boldsymbol{P}_{\mathrm{Y}}^{i,\times}$ is inside Π, there are many possibilities which would affect the finding of $\boldsymbol{P}_{\mathrm{opt}}^{i}$. To start with, we study the mixing of Fig. 2.4(a) and the various possible shapes of the feasible region of the rate constraints. In fact, Fig. 2.4(a) represents as many as 8 possible cases ($\boldsymbol{l}_{Y_2}$ cuts either $P_1^i = 0$ or $P_2^i = \bar{P}_2$; $\boldsymbol{l}_{Y_1}$ cuts $P_2^i = 0$ or $P_1^i = \bar{P}_1$; and $\boldsymbol{l}_{Y_1}$ and $\boldsymbol{l}_{Y_2}$ swap). Let us first restrict ourselves to the case (a) if $\boldsymbol{l}_{Y_2}$ cuts $P_2^i = \bar{P}_2$ and $\boldsymbol{l}_{Y_1}$ cuts $P_1^i = \bar{P}_1$, so the feasible region due to the energy harvesting constraints makes out a hexagon, with 4 sides there to be cut by $\boldsymbol{l}_{R_1}$ and $\boldsymbol{l}_{R_2}$. As shown in the appendix, there are 10 ways of lines $\boldsymbol{l}_{R_1}$ and $\boldsymbol{l}_{R_2}$ landing on the four edges, which we will list below. Before we do so, note that in all the cases, the optimal power allocation pairs $\boldsymbol{P}_{\mathrm{opt}}^{i}$ can be commonly obtained by

$$\boldsymbol{P}_{\mathrm{opt}}^{i} = \arg\max_{\boldsymbol{P}^i \in \Pi^*} R_{sum}(\boldsymbol{P}^i), \tag{2.64}$$

where Π^* denotes the set of points with potential to be the optimum. Thus, henceforth, our focus is on finding the set Π^*.

Now, we list the 10 cases for scenario (i) as follows:

- $(1,1)$, i.e., $P_2|_{\mathsf{RY}_{1,2}} > \bar{P}_2$ and $P_2|_{\mathsf{RY}_{2,2}} > \bar{P}_2$.[2] In this case, the rate constraints dominate (i.e., satisfying the rate constraints implies satisfaction of the energy harvesting constraints) and the optimal $\boldsymbol{P}_{\mathrm{opt}}^{i}$ is given by (2.40).

[2]Here, the notation $P_m|_{\mathsf{X}}$ indicates the P_m coordinate for point X.

- $(1,2)$, i.e., $P_2|_{\mathsf{RY}_{1,2}} > \bar{P}_2$ and $P_2|_{\boldsymbol{P}_{\mathrm{Y}}^{i,\times}} < P_2|_{\mathsf{RY}_{2,2}} < \bar{P}_2$. As a result, the set Π^* can be found as

$$\Pi^* = \left\{\mathsf{R}_{1,-}, \mathsf{Y}_{2,-}, \mathsf{RY}_{2,2}\right\}. \tag{2.65}$$

- $(1,3)$: $P_2|_{\mathsf{RY}_{1,2}} > \bar{P}_2$ and $P_2|_{\mathsf{Y}_{1,|}} < P_2|_{\mathsf{RY}_{2,1}} < P_2|_{\boldsymbol{P}_{\mathrm{Y}}^{i,\times}}$. Therefore, Π^* is determined as

$$\Pi^* = \left\{\mathsf{R}_{1,-}, \mathsf{Y}_{2,-}, \boldsymbol{P}_{\mathrm{Y}}^{i,\times}, \mathsf{RY}_{2,1}\right\}. \tag{2.66}$$

- $(1,4)$: $P_2|_{\mathsf{RY}_{1,2}} > \bar{P}_2$ and $P_2|_{\mathsf{R}_{2,|}} < P_2|_{\mathsf{Y}_{1,|}}$, which gives

$$\Pi^* = \left\{\mathsf{R}_{1,-}, \mathsf{Y}_{2,-}, \boldsymbol{P}_{\mathrm{Y}}^{i,\times}, \mathsf{Y}_{1,|}, \mathsf{R}_{2,|}\right\}. \tag{2.67}$$

- $(2,2)$: That is, $P_2|_{\boldsymbol{P}_{\mathrm{Y}}^{i,\times}} < P_2|_{\mathsf{RY}_{1,2}} < \bar{P}_2$ and $P_2|_{\boldsymbol{P}_{\mathrm{Y}}^{i,\times}} < P_2|_{\mathsf{RY}_{2,2}} < \bar{P}_2$. In this case, we have

$$\Pi^* = \left\{\mathsf{RY}_{1,2}, \mathsf{RY}_{2,2}\right\}. \tag{2.68}$$

- $(2,3)$: That is, $P_2|_{\boldsymbol{P}_{\mathrm{Y}}^{i,\times}} < P_2|_{\mathsf{RY}_{1,2}} < \bar{P}_2$ and $P_2|_{\mathsf{Y}_{1,|}} < P_2|_{\mathsf{RY}_{2,1}} < P_2|_{\boldsymbol{P}_{\mathrm{Y}}^{i,\times}}$. Then Π^* is given by

$$\Pi^* = \left\{\mathsf{RY}_{1,2}, \boldsymbol{P}_{\mathrm{Y}}^{i,\times}, \mathsf{RY}_{2,1}\right\}. \tag{2.69}$$

- $(2,4)$: That is, $P_2|_{\boldsymbol{P}_{\mathrm{Y}}^{i,\times}} < P_2|_{\mathsf{RY}_{1,2}} < \bar{P}_2$ and $P_2|_{\mathsf{R}_{2,|}} < P_2|_{\mathsf{Y}_{1,|}}$. Consequently, we have Π^* given by

$$\Pi^* = \left\{\mathsf{RY}_{1,2}, \boldsymbol{P}_{\mathrm{Y}}^{i,\times}, \mathsf{Y}_{1,|}, \mathsf{R}_{2,|}\right\}. \tag{2.70}$$

- $(3,3)$: That is, $P_2|_{\mathsf{Y}_{1,|}} < P_2|_{\mathsf{RY}_{1,1}}, P_2|_{\mathsf{RY}_{2,1}} < P_2|_{\boldsymbol{P}_{\mathrm{Y}}^{i,\times}}$. As such, the set Π^* is found as

$$\Pi^* = \left\{\mathsf{RY}_{1,1}, \mathsf{RY}_{2,1}\right\}. \tag{2.71}$$

- $(3,4)$: That is, $P_2|_{\mathsf{Y}_{1,|}} < P_2|_{\mathsf{RY}_{1,1}} < P_2|_{\boldsymbol{P}_{\mathrm{Y}}^{i,\times}}$ as well as $P_2|_{\mathsf{R}_{2,|}} < P_2|_{\mathsf{Y}_{1,|}}$. As a result, we get

$$\Pi^* = \left\{\mathsf{RY}_{1,1}, \mathsf{Y}_{1,|}, \mathsf{R}_{2,|}\right\}. \tag{2.72}$$

- $(4,4)$: That is, $P_2|_{\mathsf{R}_{1,|}}, P_2|_{\mathsf{R}_{2,|}} < P_2|_{\mathsf{Y}_{1,|}}$. Hence,

$$\Pi^* = \left\{\mathsf{R}_{1,|}, \mathsf{R}_{2,|}\right\}. \tag{2.73}$$

Note that $\boldsymbol{l}_{Y_2}$ may cut $P_1^i = 0$ instead of $P_2^i = \bar{P}_2$, while $\boldsymbol{l}_{Y_1}$ still cuts $P_1^i = \bar{P}_1$. We refer to this case as (b). In this case, we will have a pentagon feasible region made out by the energy harvesting constraints and have the following 6 situations:

- $(1,1)$: This case is same as $(2,2)$ in case (a) above.
- $(1,2)$: This case is same as $(2,3)$ in case (a) above.
- $(1,3)$: This case is same as $(2,4)$ in case (a) above.
- $(2,2)$: This case is same as $(3,3)$ in case (a) above.
- $(2,3)$: This case is same as $(3,4)$ in case (a) above.
- $(3,3)$: This case is same as $(4,4)$ in case (a) above.

We can also have the case (c) that $\boldsymbol{l}_{Y_2}$ may cut $P_2^i = \bar{P}_2$, but $\boldsymbol{l}_{Y_1}$ cuts $P_2^i = 0$ instead. In this case, we will have a pentagon feasible region and have the following 6 situations:

- $(1,1)$: This case is same as $(1,1)$ in case (a) above.
- $(1,2)$: This case is same as $(1,2)$ in case (a) above.
- $(1,3)$: This case is same as $(1,3)$ in case (a) above.
- $(2,2)$: This case is same as $(2,2)$ in case (a) above.
- $(2,3)$: This case is same as $(2,3)$ in case (a) above.
- $(3,3)$: This case is same as $(3,3)$ in case (a) above.

The last case (d) is that $\boldsymbol{l}_{Y_2}$ may cut $P_1^i = 0$, and $\boldsymbol{l}_{Y_1}$ cuts $P_2^i = 0$. In this case, we will only have 3 situations:

- $(1,1)$: This case is same as $(2,2)$ in case (a) above.
- $(1,2)$: This case is same as $(2,3)$ in case (a) above.
- $(2,2)$: This case is same as $(3,3)$ in case (a) above.

2.4.4.2 Scenario (ii)

Here, we address the case when $\boldsymbol{P}_{\mathrm{Y}}^{i,\times}$ is outside and on the right of Π. There are two possible cases in scenario (ii). We first look at case (a) if $\boldsymbol{l}_{Y_2}$ cuts $P_2^i = \bar{P}_2$ and $P_1^i = \bar{P}_1$. In this case, we have a pentagon feasible region and have the following 6 situations:

- $(1,1)$: This case is same as $(1,1)$ in scenario $(i)(a)$.
- $(1,2)$: The condition needs to be changed to $P_2|_{\mathsf{RY}_{1,2}} > \bar{P}_2$ and $P_2|_{\mathsf{Y}_{2,|}} < P_2|_{\mathsf{RY}_{2,2}} < \bar{P}_2$, although the optimal set Π^* is same as $(1,2)$ in scenario $(i)(a)$, or (2.65).
- $(1,3)$: That is, $P_2|_{\mathsf{RY}_{1,2}} > \bar{P}_2$ and $P_2|_{\mathsf{R}_{2,|}} < P_2|_{\mathsf{Y}_{2,|}}$. As a result, Π^* is given by

$$\Pi^* = \left\{\mathsf{R}_{1,-}, \mathsf{Y}_{2,-}, \mathsf{Y}_{2,|}, \mathsf{R}_{2,|}\right\}. \tag{2.74}$$

- $(2,2)$: The optimal set Π^* is given by the result of $(2,2)$ in scenario $(i)(a)$, i.e., (2.68), but the condition has now been revised to $P_2|_{\mathsf{Y}_{2,|}} < P_2|_{\mathsf{RY}_{1,2}}, P_2|_{\mathsf{RY}_{2,2}} < \bar{P}_2$.
- $(2,3)$: That is, $P_2|_{\mathsf{Y}_{2,|}} < P_2|_{\mathsf{RY}_{1,2}} < \bar{P}_2$ and $P_2|_{\mathsf{R}_{2,|}} < P_2|_{\mathsf{Y}_{2,|}}$. Then Π^* is given by

$$\Pi^* = \left\{\mathsf{RY}_{1,2}, \mathsf{Y}_{2,|}, \mathsf{R}_{2,|}\right\}. \tag{2.75}$$

- $(3,3)$: The condition is $P_2|_{\mathsf{R}_{1,|}}, P_2|_{\mathsf{R}_{2,|}} < P_2|_{\mathsf{Y}_{2,|}}$ but the set Π^* is same as $(4,4)$ in scenario $(i)(a)$ or (2.73).

Now, we move on to another case (b) in which $\boldsymbol{l}_{Y_2}$ still cuts $P_1^i = \bar{P}_1$ but opts to cut $P_1^i = 0$ instead of $P_2^i = \bar{P}_2$. In that case, we will only have 3 possibilities:

- $(1,1)$: This case is same as $(2,2)$ in scenario $(ii)(a)$.
- $(1,2)$: This case is same as $(2,3)$ in scenario $(ii)(a)$.
- $(2,2)$: This case is same as $(3,3)$ in scenario $(ii)(a)$.

2.4.4.3 Scenario (iii)

This scenario looks into the case when $\boldsymbol{P}_{\mathrm{Y}}^{i,\times}$ is at the top or left side of Π, which corresponds to the fact that (a) $\boldsymbol{l}_{Y_1}$ cuts $P_2^i = \bar{P}_2$ and $P_2^i = 0$, or (b) $\boldsymbol{l}_{Y_1}$ cuts $P_1^i = 0$ and $P_2^i = 0$. For (a), we have 3 situations:

- $(1,1)$: Same as in scenario $(i)(a)$, the optimal $\boldsymbol{P}_{\mathrm{opt}}^i$ can be found by (2.40), and Π^* is given by $\{\mathsf{R}_{1,-}, \mathsf{R}_{2,-}\}$ but the condition becomes $P_2|_{\mathsf{RY}_{1,1}}, P_2|_{\mathsf{RY}_{2,1}} > \bar{P}_2$.
- $(1,2)$: That is, $P_2|_{\mathsf{RY}_{1,1}} > \bar{P}_2$ and $P_2|_{\mathsf{RY}_{2,1}} < \bar{P}_2$. The set Π^* therefore can be obtained as
$$\Pi^* = \left\{\mathsf{R}_{1,-}, \mathsf{Y}_{1,-}, \mathsf{RY}_{2,1}\right\}. \tag{2.76}$$
- $(2,2)$: That is, $P_2|_{\mathsf{RY}_{1,1}}, P_2|_{\mathsf{RY}_{2,1}} < \bar{P}_2$. The optimal set Π^* is given by (2.71) in $(3,3)$ of scenario $(i)(a)$.

On the other hand, for scenario $(iii)(b)$, we will only have one possibility with a triangular feasible region from the energy harvesting constraints. In that case, the result is same as $(2,2)$ in scenario $(iii)(a)$ above for finding the optimal set Π^*.

2.5 Numerical Results

In this section, numerical examples are presented to illustrate how the optimal power allocation and its corresponding sum-rate vary w.r.t. the constraints, and how the feasible region changes its shape to validate our analysis. For convenience, we set $\bar{P}_1 = \bar{P}_2 = 2$ and $\sigma_1^2 = \sigma_2^2 = 0.01$, and as a reference, also define the signal-to-noise ratio (SNR) as

$$\mathrm{SNR} = 10\log_{10}\frac{\bar{P}_1}{\sigma_1^2} = 10\log_{10}\frac{2}{0.01} = 23\mathrm{dB}. \tag{2.77}$$

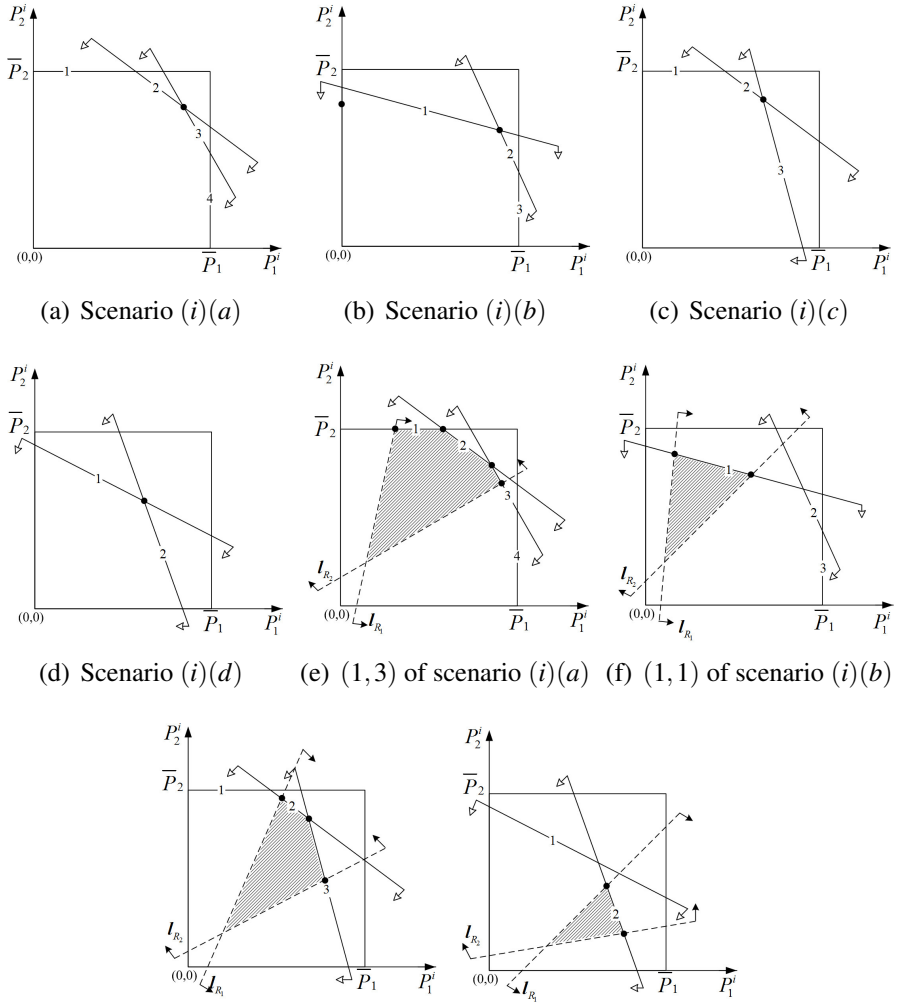

(a) Scenario $(i)(a)$ (b) Scenario $(i)(b)$ (c) Scenario $(i)(c)$

(d) Scenario $(i)(d)$ (e) $(1,3)$ of scenario $(i)(a)$ (f) $(1,1)$ of scenario $(i)(b)$

(g) $(2,3)$ of scenario $(i)(c)$ (h) $(2,2)$ of scenario $(i)(d)$

Figure 2.5: Illustration of the possible combinations of lines $\boldsymbol{l}_{R_1}$, $\boldsymbol{l}_{R_2}$, $\boldsymbol{l}_{l_1}$ and $\boldsymbol{l}_{l_2}$ for scenario (i) where $\boldsymbol{P}_{\mathrm{Y}}^{i,\times}$ is inside Π. In (a)–(d), it shows 4 possible ways $\boldsymbol{l}_{Y_1}$ and $\boldsymbol{l}_{Y_2}$ may cut Π to form the region due to the energy harvesting constraints with numbered edges, while (e)–(h) provide examples for each of the cases how $\boldsymbol{l}_{R_1}$ and $\boldsymbol{l}_{R_2}$ may cut the edges to form the feasible region.

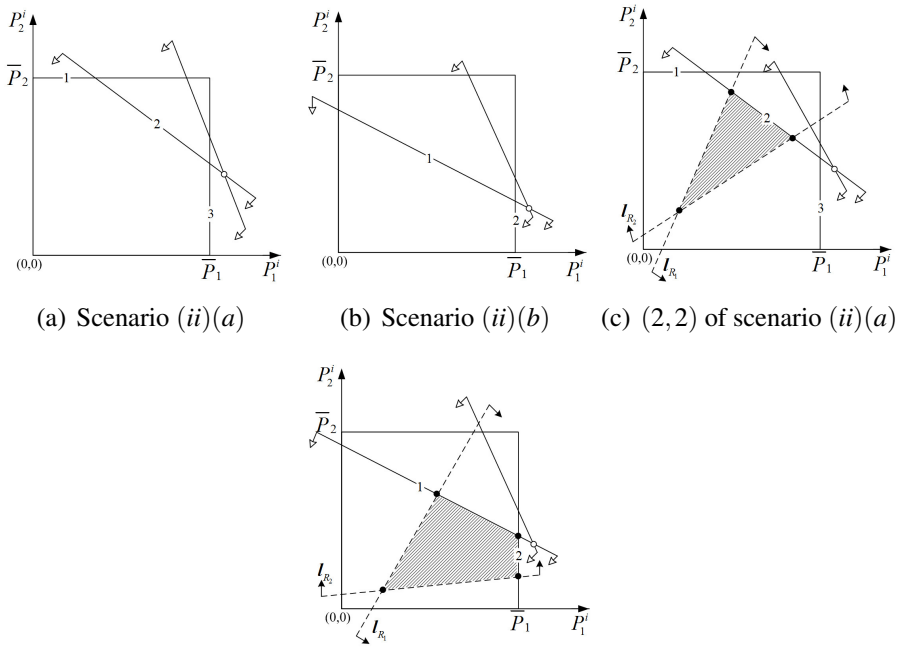

(a) Scenario $(ii)(a)$ (b) Scenario $(ii)(b)$ (c) $(2,2)$ of scenario $(ii)(a)$

(d) $(1,2)$ of scenario $(ii)(b)$

Figure 2.6: Illustration of the possible combinations of lines $\boldsymbol{l}_{R_1}$, $\boldsymbol{l}_{R_2}$, $\boldsymbol{l}_{l_1}$ and $\boldsymbol{l}_{l_2}$ for scenario (ii) where $\boldsymbol{P}_{\mathrm{Y}}^{i,\times}$ is outside and on the right of Π. In (a) and (b), it shows 2 possible ways $\boldsymbol{l}_{Y_1}$ and $\boldsymbol{l}_{Y_2}$ may cut Π while in (c) and (d), it shows examples of how $\boldsymbol{l}_{R_1}$, $\boldsymbol{l}_{R_2}$ cut the edges to form the feasible region.

Fig. 2.8 assumed the following channel gain matrix

$$\mathbf{G} = \begin{bmatrix} 0.7323 & 0.0451 \\ 0.0366 & 0.2600 \end{bmatrix}, \tag{2.78}$$

and considered the constraints $\frac{\mathscr{D}_1}{T-\tau} = 2.5$, $\frac{\mathscr{D}_2}{T-\tau} = 2.8$, $\frac{\mathscr{W}_1}{\tau} = 0.25$, and $\frac{\mathscr{W}_2}{\tau} = 0.4$. The optimal points with and without the constraints are marked in the figure. Fig. 2.9 provided similar results but with a different channel gain matrix

$$\mathbf{G} = \begin{bmatrix} 0.1942 & 0.0213 \\ 0.0229 & 0.8234 \end{bmatrix} \tag{2.79}$$

and $\frac{\mathscr{D}_1}{T-\tau} = 2.2$, $\frac{\mathscr{D}_2}{T-\tau} = 2.8$, $\frac{\mathscr{W}_1}{\tau} = 0.2$, $\frac{\mathscr{W}_2}{\tau} = 0.4$. As we can see, without rate and energy-harvesting constraints, the optimal point for the example in Fig. 2.8 appears as $(\bar{P}_1, 0)$, while for Fig. 2.9, it appears as $(\bar{P}_1, \bar{P}_2)$, which aligns with our analysis.

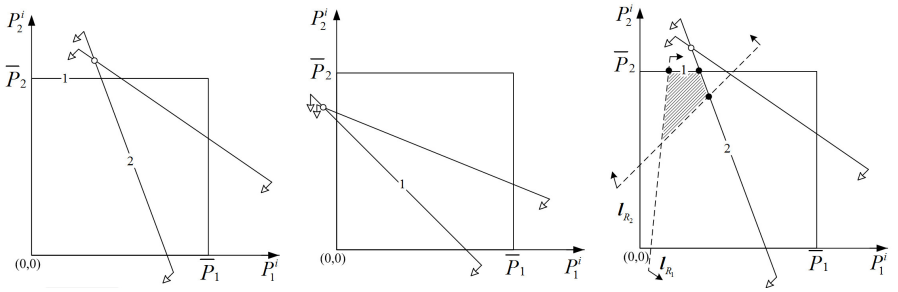

(a) Scenario $(iii)(a)$ (b) Scenario $(iii)(b)$ (c) $(1,2)$ of scenario $(iii)(a)$

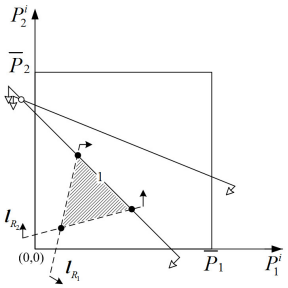

(d) $(1,1)$ of scenario $(iii)(b)$

Figure 2.7: Illustration of the possible combinations of lines $\boldsymbol{l}_{R_1}$, $\boldsymbol{l}_{R_2}$, $\boldsymbol{l}_{l_1}$ and $\boldsymbol{l}_{l_2}$ for scenario (iii) where $\boldsymbol{P}_{\mathrm{Y}}^{i,\times}$ is at the top or left side of Π. In (a) and (b), it shows 2 possible ways $\boldsymbol{l}_{Y_1}$ and $\boldsymbol{l}_{Y_2}$ may cut Π while in (c) and (d), it shows examples of how $\boldsymbol{l}_{R_1}$, $\boldsymbol{l}_{R_2}$ cut the edges to form the feasible region.

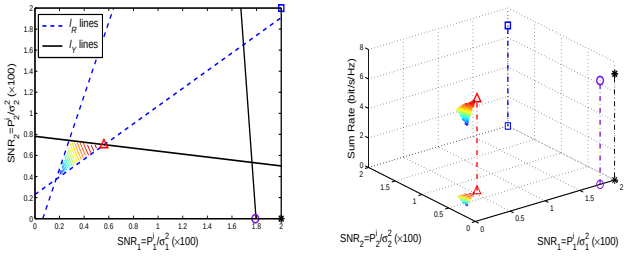

(a) The resulting feasible region (b) Comparison of sum-rates

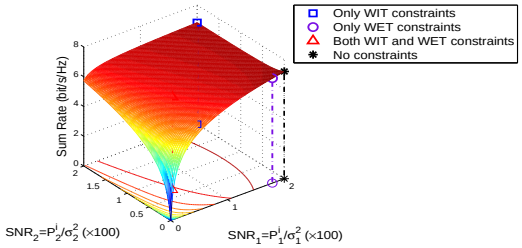

(c) Sum-rate versus SNR

Figure 2.8: Results for the time-switching SWIPT system for a given **G**.

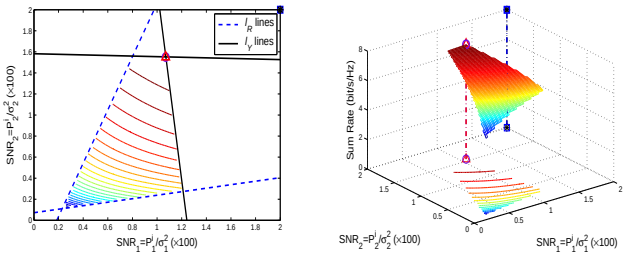

(a) The resulting feasible region (b) Comparison of sum-rates

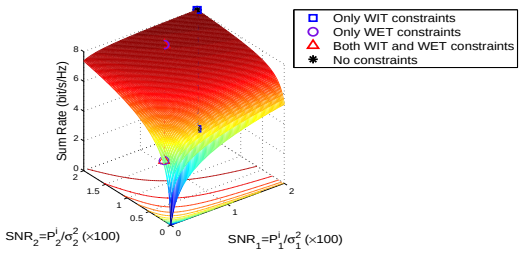

(c) Sum-rate versus SNR

Figure 2.9: Results for the time-switching SWIPT system for another **G**.

Table 2.3: Sum-rates for the time-switching SWIPT system.

Sum-rate (bits/s/Hz)	No constraint	Only WIT constraints	Only WET constraints	All constraints
Fig. 2.8	7.2043	6.8210 (94.7%)	7.0454 (97.8%)	6.2408 (86.6%)
Fig. 2.9	7.9973	7.9973 (100%)	7.7866 (97.3%)	7.7866 (97.3%)

Table 2.3 provides the sum-rates for the two examples.

We now proceed to illustrate how the feasible region varies w.r.t. the time allocation parameter τ. The results are shown in Fig. 2.10 in which we have assumed that

$$\mathbf{G} = \begin{bmatrix} 0.3252 & 0.0172 \\ 0.0221 & 0.2379 \end{bmatrix}, \tag{2.80}$$

and $\underline{\mathscr{D}}_1 = 0.5$, $\underline{\mathscr{D}}_2 = 0.8$, $\underline{\mathscr{W}}_1 = 0.015$, and $\underline{\mathscr{W}}_2 = 0.014$, assuming $T = 1$. Results for $\tau = 0.3, 0.25, 0.2$ are shown. It can be observed that the feasible region as well as the sum-rate optimal point change with τ. An optimization of τ can only be achieved using numerical methods.

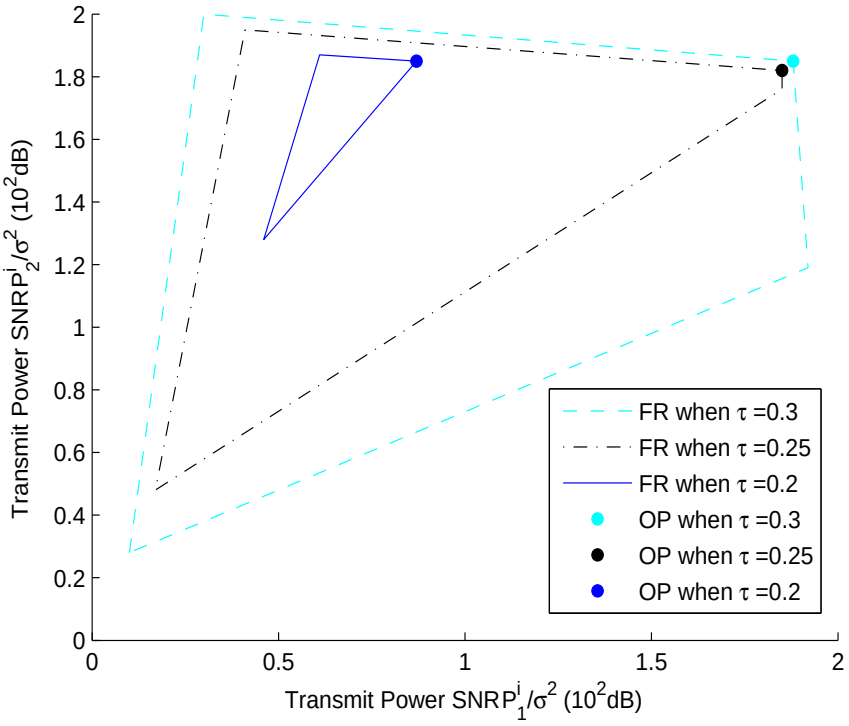

Figure 2.10: Feasible region versus τ.

Even though the joint optimization of the power allocation strategy and τ does not admit any closed-form solution, our derived closed-form power allocation solution greatly facilitates the optimization using a simple one-dimensional search. To help illustrate the joint optimization with τ, Fig. 2.11 shows the sum-rate against the various value of τ using an example assuming the channel gain matrix

$$\mathbf{G} = \begin{bmatrix} 0.9404 & 0.0273 \\ 0.0410 & 0.6250 \end{bmatrix}, \tag{2.81}$$

and with the constraints being $\underline{\mathscr{D}}_1 = 1$, $\underline{\mathscr{D}}_2 = 1$, $\underline{\mathscr{W}}_1 = 0.5$, and $\underline{\mathscr{W}}_2 = 0.5$. The results demonstrate how the sum-rates may vary with and without the rate and energy harvesting constraints. In this particular example, with both rate and energy harvesting constraints, it can be observed that the sum-rate attains its maximum $R_{sum} = 4.389$ when $\tau = 0.427$.

While this chapter focuses mainly on the interference channels with time-switching WIT and WPT, one may presume that for the two-user channel, the sum-

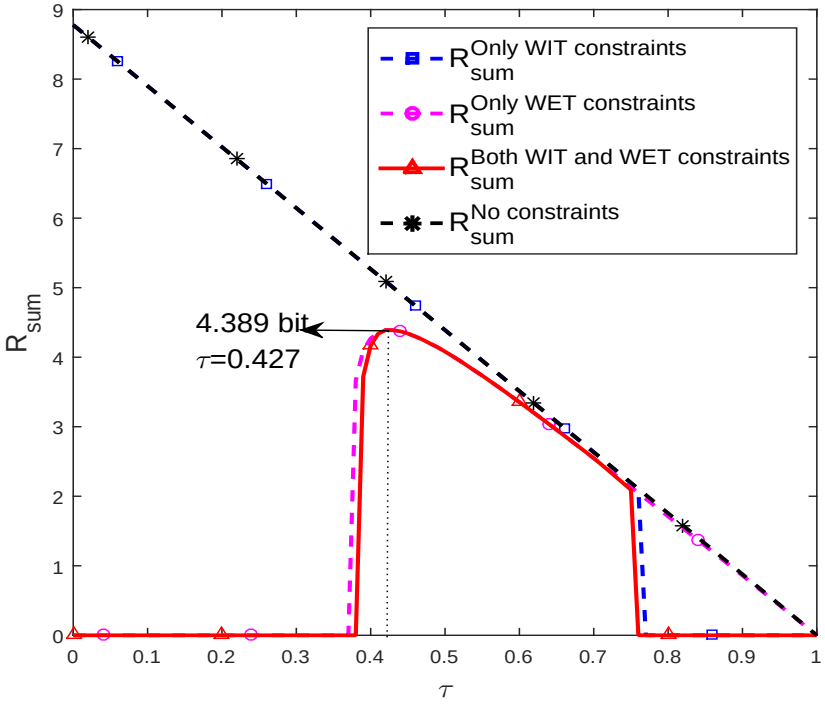

Figure 2.11: The sum-rates versus the time-switching factor τ.

rates can be furthermore maximized by alternating WIT and WPT between the two users. That is to say, when user 1 adopts WIT, user 2 operates in the WPT mode, and vice versa. Nonetheless, it is not clear that the alternating approach would definitely perform better in the sum-rate maximization problem with rate and energy harvesting constraints than our considered approach.

In order to gain more insights, we consider the alternating approach and note that for the first time instance with duration $T-\tau$, it would have

$$\begin{cases} \mathscr{D}_1 &= (T-\tau)\log_2\left(1+\frac{P_1^i G_{1,1}}{\sigma_n^2+P_2^e G_{1,2}}\right), \\ \mathscr{W}_2 &= (T-\tau)(P_2^e G_{2,2}+\sigma_2^2+P_1^i G_{2,1}). \end{cases} \tag{2.82}$$

Then for the second instance with duration τ, it has

$$\begin{cases} \mathscr{W}_1 &= \tau(P_1^e G_{1,1}+\sigma_1^2+P_2^i G_{1,2}), \\ \mathscr{D}_2 &= \tau\log_2\left(1+\frac{P_2^i G_{2,2}}{\sigma_n^2+P_1^e G_{2,1}}\right). \end{cases} \tag{2.83}$$

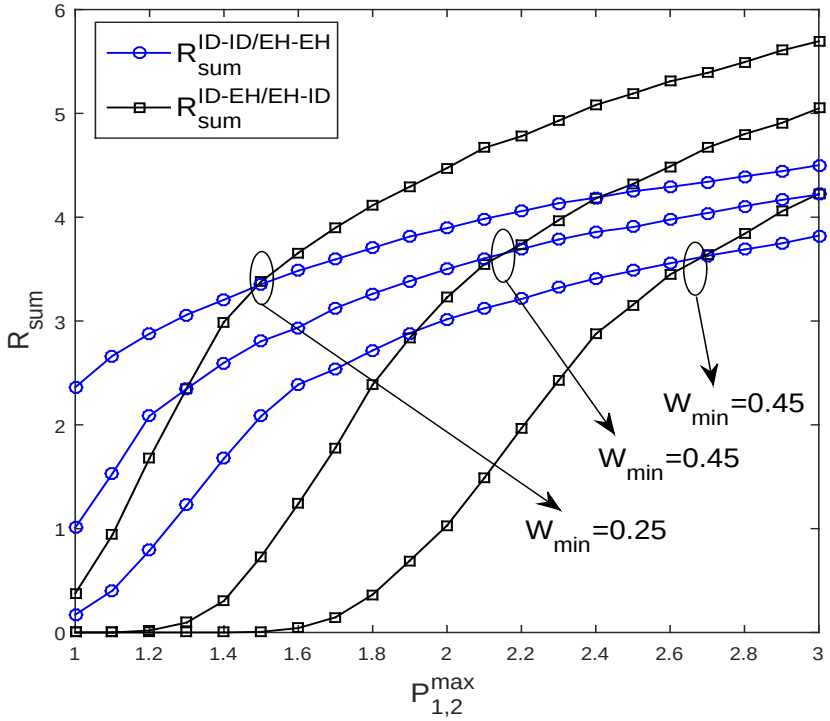

Figure 2.12: The sum rates with both rate and energy harvesting constraints against the power budget $\bar{P}_{1,2}$, with $\tau = 0.5$.

In Fig. 2.12, we illustrate the average sum-rates over 1000 independent channel realizations with $\underline{\mathscr{D}}_{1,2} = 1.2$, and compare them with our optimal solution for the interference system. As can be observed, for smaller peak power, the interference system indeed has higher sum-rates than the alternating model, although as the peak power increases, the sum-rates for the alternating model begin to benefit and result in higher rates. In addition, the crossover points will appear later, or at larger peak power, as the energy harvesting constraints become more stringent. The numerical results have now confirmed that the alternating model is actually not necessarily more beneficial than the interference model in the chapter.

Chapter 3

Wireless Power Transfer in Massive MIMO Aided HetNets with User Association

3.1 Introduction

HetNets are identified as one of the key enablers for 5G, in HetNets, small cells are densely deployed [19, 68], which shortens the distances between the mobile devices and the BSs. Recently, there is an interesting integration between WPT and HetNets, suggesting that stations, referred to as PBs, be deployed in cellular networks for powering users via WPT [7].

On the other hand, massive-MIMO systems using a large number of antennas at the BSs, promise an ultra-high spectral efficiency by accommodating a large number of users in the same radio channel [30]. Additional, the exceptional spatial selectivity means that very sharp signal beams can be formed [69, 70] and of great importance to WPT. Motivated by these research efforts, in this chapter, we explore the potential benefits of massive MIMO HetNets for WPT and WIT, which has not been conducted yet.

Different from the aforementioned literature such as [31, 71, 72] where WPT and WIT were only considered in a single cell, we studied that massive MIMO antennas are harnessed in the macrocells, and employ a stochastic geometry approach

to model the K-tier HetNets. In particular, the users first harvest energy from downlink WPT, and then use the harvested energy for WIT in the uplink. In this scenario, user association plays a defining role in the overall performance. As a matter of fact, user association in massive MIMO HetNets has been recently investigated for optimizing the throughput [22**?** , 23] and energy efficiency [73].

3.2 Contribution

To be specific, we consider two simple user association methods: (1) downlink received signal power (DRSP) based for maximum harvested energy, and (2) uplink received signal power (URSP) based for minimum uplink path loss. One of our aims is to find out which scheme is better for uplink WIT. We have made the following contributions:

- We provide a tractable framework to examine the implementation of downlink WPT and uplink WIT in massive MIMO aided HetNets by using a stochastic geometric model. As the intra-tier interference is the source of energy, interference avoidance is not required and maximal-ratio transmission (MRT) beamforming is used for WPT for multiple users in the macrocells.

- We investigate the impacts of massive MIMO on the user association of the HetNets, and examine both DRSP-based and URSP-based algorithms by deriving the exact and asymptotic expressions for the probability of a user associated with a macrocell or a small cell in the HetNet.

- We derive the exact and asymptotic expressions for the average harvested energy. We show that the asymptotic expressions can well approximate the exact ones. The implementation of massive MIMO can significantly increase the harvested energy in the HetNets, since it provides larger power gain for users served in the macrocells, and enables that users with higher received power are offloaded to the small cells.[1] In addition, DRSP-based user association scheme outperforms URSP-based in terms of harvested energy, which means

[1]Note that power gain is also referred to as array gain in the literature.

Table 3.1: Notation

Φ_{M}, λ_{M}	Macrocells PPP and density
Φ_i, λ_i	i-th tier PPP and density
T, τ	One block time and time allocation factor
N	Number of antennas
S	Number of single-antenna users served by a MBS
P_{M}, P_i	MBS and i-th tier transmit power
α_{M}, α_i	MBS and i-th tier pass loss exponent
G_a^{D}, G_a^{U}	Downlink and uplink power gain
d	Reference distance
h, g	Small-scale fading channel power gain
$\Gamma(\vartheta,\theta)$	Gamma distribution with shape ϑ and scale θ
$\exp(z)$	Exponential distribution with the parameter z
$\widetilde{\mathscr{U}}_{\mathrm{M}}$, $\widetilde{\mathscr{U}}_i$	Interfering users PPP in the MBS tier and the i-th tier
P_{u_o}	Typical user's transmit power
$\mathbf{1}(\cdot)$	Indicator function
$\mathbb{E}\{\cdot\}$	Expectation operator

that it supports higher user transmit power for uplink information transmission.

- We derive the average uplink achievable rate powered by the harvested energy. Our results demonstrate that the uplink performance is enhanced by increasing the number of antennas at the macrocell BS, but serving more users in the macrocells decreases the average achievable rate because of lower uplink transmit power and severer uplink interference. Furthermore, although DRSP-based user association scheme harvests more energy to provide larger uplink transmit power, URSP-based can achieve better WIT performance in the uplink.

The notation of this thesis is shown in Table 3.1.

3.3 Network Description

This chapter considers a K-tier time-division duplex (TDD) HetNet including macrocells and small cells such as picocells and relays, etc. Each user first harvests the energy from its serving BS in the downlink, and uses the harvested energy for WIT in the uplink. Let T be the duration of a communication block. The first and second sub-blocks of duration τT and $(1-\tau)T$ are allocated to the downlink

WPT and uplink WIT, respectively, where $\tau\,(0 \leq \tau \leq 1)$ is the time allocation factor. We assume that the first tier represents the class of MBSs, each of which is equipped with a large antenna array [74]. The locations of the MBSs are modelled using a homogeneous Poisson point process (HPPP) Φ_{M} with density λ_{M}. The locations of the SBSs in the i-th tier ($i = 2, \ldots, K$) are modelled by an independent HPPP Φ_i with density λ_i. It is assumed that the density of users is much greater than that of BSs so that there always will be one active mobile user at each time slot in every small cell and hence multiple active mobile users in every macrocell.[2] In the macrocell, S single-antenna users communicate with an N-antenna MBS (assuming $N \gg S \geq 1$) in the uplink over the same time slot and frequency band, while in the small cell, only one single-antenna user is allowed to communicate with a single-antenna SBS at a time slot. We assume that perfect CSI is known at the BS,[3] and universal frequency reuse is employed such that all of the tiers share the same bandwidth. In addition, all the channels are assumed to undergo independent identically distributed (i.i.d.) quasi-static Rayleigh block fading.

3.3.1 User Association

We introduce two user association algorithms: (1) a user is associated with the BS based on the maximum DRSP at the user, which results in the largest average received power; and (2) a user is associated with the BS based on the maximum URSP at the BS, which will reduce the user's power consumption.[4]

Considering the effect of massive MIMO with equal power allocation, the average received power at a user that is connected with the ℓ-th MBS ($\ell \in \Phi_{\mathrm{M}}$) can be expressed as

$$P_{r,\ell} = G_a^{\mathrm{D}} \frac{P_{\mathrm{M}}}{S} L\left(\left|X_{\ell,\mathrm{M}}\right|\right), \tag{3.1}$$

[2] In reality, there may be more than one active users in a small cell and this can be dealt with using multiple access techniques.

[3] In the practical TDD massive MIMO systems, the downlink CSI can be obtained through channel reciprocity based on uplink training.

[4] Although user association for the downlink and uplink can be decoupled to maximize both the DRSP and URSP, the main drawback for the decoupling is that channel reciprocity in massive MIMO systems will be lost [75].

where G_a^{D} denotes the power gain (or array gain) obtained by the user associated with the MBS, P_{M} is the MBS's transmit power, $L\left(\left|X_{\ell,\mathrm{M}}\right|\right) = \beta\left|X_{\ell,\mathrm{M}}\right|^{-\alpha_{\mathrm{M}}}$ is the path loss function, β is the frequency dependent constant value, $\left|X_{\ell,\mathrm{M}}\right|$ denotes the distance, and α_{M} is the path loss exponent. In the small cell, the average received power at a user that is connected with the j-th SBS ($j \in \Phi_i$) in the i-th tier is expressed as

$$P_{r,i} = P_i L\left(\left|X_{j,i}\right|\right), \tag{3.2}$$

where P_i denotes the SBS's transmit power in the i-th tier and as above $L\left(\left|X_{j,i}\right|\right) = \beta\left(\left|X_{j,i}\right|\right)^{-\alpha_i}$ is the path loss function with distance $\left|X_{j,i}\right|$ and path loss exponent α_i.

For DRSP-based user association, the aim is to maximize the average received power. Thus, the serving BS for a typical user is selected according to the following criterion:

$$\mathrm{BS} : \arg \max_{k \in \{\mathrm{M},2,\ldots,K\}} P_{r,k}^*, \tag{3.3}$$

where

$$P_{r,\mathrm{M}}^* = \max_{\ell \in \Phi_{\mathrm{M}}} P_{r,\ell}, \text{ and } P_{r,i}^* = \max_{j \in \Phi_i} P_{r,i}. \tag{3.4}$$

By contrast, for URSP-based user association, the objective is to minimize the uplink path loss, and as such, the serving BS for a typical user is selected by

$$\mathrm{BS} : \arg \max_{k \in \{\mathrm{M},2,\ldots,K\}} L^*\left(|X_k|\right), \tag{3.5}$$

where

$$L^*\left(|X_{\mathrm{M}}|\right) = G_a^{\mathrm{U}} \max_{\ell \in \Phi_{\mathrm{M}}} L\left(\left|X_{\ell,\mathrm{M}}\right|\right), \tag{3.6}$$

$$L^*\left(|X_i|\right) = \max_{j \in \Phi_i} L(\left|X_{j,i}\right|). \tag{3.7}$$

Here, G_a^{U} is the power gain of the serving MBS and $L^*\left(|X_{\mathrm{M}}|\right)$ can be viewed as compensated path loss due to the power gain.

3.3.2 Downlink WPT Model

For wireless energy harvesting, the RF signals are interpreted as energy. Therefore, in the macrocell, we adopt the low-complexity linear MRT beamforming to transfer the power towards its S intended users with equal-time sharing.[5] The allocated time for power transfer for each intended user is $\frac{\tau T}{S}$. We use the short-range propagation model [7, 76] to avoid singularity caused by proximity between the BSs and the users. This will ensure that users receive finite average power.

As the energy harvested from the noise is negligible, during the energy harvesting phase, the total harvested energy at a typical user o that is associated with the MBS is given by

$$\begin{aligned}\mathrm{E}_{o,\mathrm{M}} = &\underbrace{\eta P_{\mathrm{M}} h_o L\left(\max\left\{\left|X_{o,\mathrm{M}}\right|, d\right\}\right) \times \frac{\tau T}{S}}_{\mathrm{E}^1_{o,\mathrm{M}}} \\ &+ \underbrace{\eta P_{\mathrm{M}} h'_o L\left(\max\left\{\left|X_{o,\mathrm{M}}\right|, d\right\}\right) \times \frac{(S-1)\,\tau T}{S}}_{\mathrm{E}^2_{o,\mathrm{M}}} \\ &+ \underbrace{\eta\left(I_{\mathrm{M},1} \times \tau T + I_{\mathrm{S},1} \times \tau T\right)}_{\mathrm{E}^3_{o,\mathrm{M}}}, \quad (3.8)\end{aligned}$$

where $\mathrm{E}^1_{o,\mathrm{M}}$ is the energy from the directed WPT, $\mathrm{E}^2_{o,\mathrm{M}}$ is the energy from the isotropic WPT, and $\mathrm{E}^3_{o,\mathrm{M}}$ is the energy from the ambient RF, as illustrated in Fig. 3.1. Here, $0 < \eta < 1$ is the RF-to-DC conversion efficiency, d denotes the reference distance, $h_o \sim \Gamma(N,1)$ and $\left|X_{o,\mathrm{M}}\right|$ are, respectively, the small-scale fading channel power gain and the distance when the serving MBS recharges the typical user, and $h'_o \sim \exp(1)$ is the small-scale fading channel power gain when the serving MBS directly transfers energy to other users in the same cell. In addition,

$$I_{\mathrm{M},1} = \sum_{\ell \in \Phi_{\mathrm{M}} \setminus \{o\}} P_{\mathrm{M}} h_\ell L\left(\max\left\{\left|X_{\ell,\mathrm{M}}\right|, d\right\}\right) \quad (3.9)$$

is the sum of interference from the interfering MBSs in the first tier, where $h_\ell \sim$

[5] In this way, user receives the largest transferred power in a short time, which means that the user's battery can be quickly recharged.

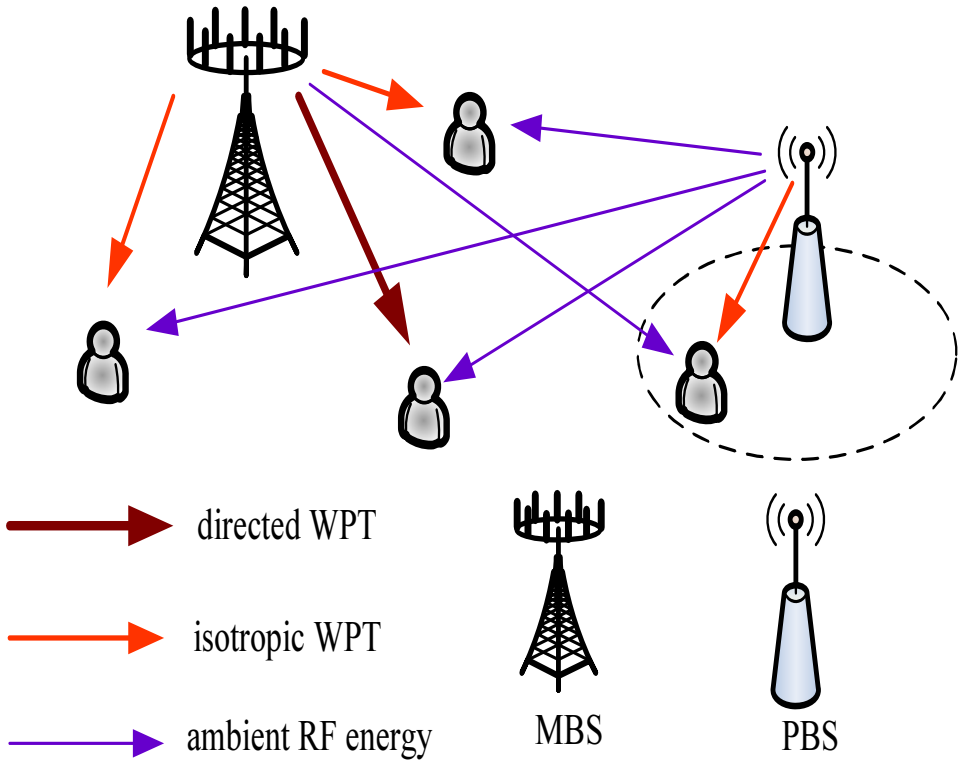

Figure 3.1: An illustration of wireless power transfer in the two-tier HetNet consisting of massive MIMO MBS and picocell base station (PBS).

$\Gamma(1,1)$ and $|X_{\ell,\mathrm{M}}|$ denote, respectively, the small-scale fading interfering channel gain and the distance between a typical user and MBS $\ell \in \Phi_{\mathrm{M}} \setminus \{o\}$ (except the typical user's serving MBS), and

$$I_{\mathrm{S},1} = \sum_{i=2}^{K} \sum_{j \in \Phi_i} P_i h_j L\left(\max\left\{|X_{j,i}|, d\right\}\right) \tag{3.10}$$

is the sum of interference from the SBSs in the first tier, where $h_j \sim \exp(1)$ and $|X_{j,i}|$ are, respectively, the small-scale fading interfering channel power gain and the distance between a typical user and SBS $j \in \Phi_i$. In each power transfer phase, the harvested energy at a typical user o associated with the SBS in the k-th tier can also be written as

$$\mathrm{E}_{o,k} = \underbrace{\eta P_k g_o L\left(\max\left\{|X_{o,k}|, d\right\}\right) \times \tau T}_{\mathrm{E}^1_{o,k}} + \underbrace{\eta\left(I_{\mathrm{M},k} + I_{\mathrm{S},k}\right) \times \tau T}_{\mathrm{E}^2_{o,k}}, \tag{3.11}$$

where $\mathrm{E}_{o,k}^{1}$ is the energy from the isotropic WPT and $\mathrm{E}_{o,k}^{2}$ is the energy from the ambient RF, $g_o \sim \Gamma(1,1)$ and $\left|X_{o,k}\right|$ are the small-scale fading channel power gain and the distance between a typical user and its associated MBS, respectively, and similar to the above, we also have

$$I_{\mathrm{M},k} = \sum_{\ell \in \Phi_{\mathrm{M}}} P_{\mathrm{M}} g_\ell L\left(\max\left\{\left|X_{\ell,\mathrm{M}}\right|, d\right\}\right), \tag{3.12}$$

in which $g_\ell \sim \Gamma(1,1)$ and $\left|X_{\ell,\mathrm{M}}\right|$ are, respectively, the small-scale fading interfering channel power gain and the distance between a typical user and MBS ℓ, and

$$I_{\mathrm{S},k} = \sum_{i=2}^{K} \sum_{j \in \Phi_i \setminus \{o\}} P_i g_{j,i} L\left(\max\left\{\left|X_{j,i}\right|, d\right\}\right), \tag{3.13}$$

in which $g_{j,i} \sim \Gamma(1,1)$ and $\left|X_{j,i}\right|$ are, respectively, the small-scale fading interfering channel power gain and the distance between a typical user and SBS $j \in \Phi_i \setminus \{o\}$.

3.3.3 Uplink WIT Model

After energy harvesting, user u_i transmits information signals to the serving BS with a specific transmit power P_{u_i}. In the uplink, each MBS uses linear zero-forcing beamforming (ZFBF) to simultaneously receive S data streams from its S intended users to cancel the intra-cell interference, which has been widely used in the massive MIMO literature [77–79].

For a typical user that is associated with its typical serving MBS, the received SINR at its typical serving MBS is given by

$$\mathrm{SINR}_{\mathrm{M}} = \frac{P_{u_o} h_{o,\mathrm{M}} L\left(\max\left\{\left|X_{o,\mathrm{M}}\right|, d\right\}\right)}{I_{u,\mathrm{M}} + I_{u,\mathrm{S}} + \delta^2}, \tag{3.14}$$

where

$$\begin{cases} I_{u,\mathrm{M}} = \displaystyle\sum_{i \in \widetilde{\mathscr{U}_{\mathrm{M}}} \setminus \{o\}} P_{u_i} h_i L\left(\max\left\{\left|X_i\right|, d\right\}\right), \\ I_{u,\mathrm{S}} = \displaystyle\sum_{i=2}^{K} \sum_{j \in \widetilde{\mathscr{U}_i}} P_{u_j} h_j L\left(\max\left\{\left|X_j\right|, d\right\}\right), \end{cases} \tag{3.15}$$

$h_{o,\mathrm{M}} \sim \Gamma(N-S+1,1)$ [79] and $\left|X_{o,\mathrm{M}}\right|$ are the small-scale fading channel power

gain and the distance between a typical user and its typical serving MBS, respectively, $h_i \sim \exp(1)$ and $|X_i|$ are the small-scale fading interfering channel power gain and the distance between the interfering user u_i and the typical serving MBS, respectively, $\widetilde{\mathscr{U}_{\mathrm{M}}}$ is the point process corresponding to the interfering users in the macrocells, while $\widetilde{\mathscr{U}_i}$ is the point process corresponding to the interfering users in the i-th tier, and δ^2 denotes the noise power.

Likewise, for a typical user associated with the typical serving SBS in the k-th tier, the received SINR is given by

$$\mathrm{SINR}_k = \frac{P_{u_o} g_{o,k} L\left(\max\left\{\left|X_{o,k}\right|, d\right\}\right)}{I_{u,\mathrm{M}} + I_{u,\mathrm{S}} + \delta^2}, \tag{3.16}$$

where

$$\begin{cases} I_{u,\mathrm{M}} = \sum\limits_{i \in \widetilde{\mathscr{U}_{\mathrm{M}}}} P_{u_i} g_i L\left(\max\left\{|X_i|, d\right\}\right), \\ I_{u,\mathrm{S}} = \sum\limits_{i=2}^{K} \sum\limits_{j \in \widetilde{\mathscr{U}_i} \setminus \{o\}} P_{u_j} g_j L\left(\max\left\{\left|X_j\right|, d\right\}\right), \end{cases} \tag{3.17}$$

$g_{o,k} \sim \exp(1)$ and $|X_o|$ are the small-scale fading channel gain and the distance between a typical user and its typical serving SBS, respectively, $g_i \sim \exp(1)$ and $|X_i|$ are the small-scale fading interfering channel gain and the distance between the interfering user u_i and the typical serving BS, respectively.

3.4 Energy Analysis

Here, the average harvested energy is derived assuming that users are equipped with large energy storage so that users can transmit reliably after energy harvesting. Considering the fact that the energy consumed for uplink information transmission should not exceed the harvested energy, the stable transmit power P_{u_o} for a typical user should satisfy [7]

$$P_{u_o} \leq \frac{\overline{\mathrm{E}}_o}{(1-\tau)T}, \tag{3.18}$$

where $\overline{\mathrm{E}}_o$ denotes the average harvested energy.

3.4.1 New Statistical Properties

Before deriving the average harvested energy, we find the following lemmas useful.

Lemma 6. *Under DRSP-based user association, the probability density functions (PDFs) of the distance $\left|X_{o,\mathrm{M}}\right|$ between a typical user and its serving MBS and the distance $\left|X_{o,k}\right|$ between a typical user and its serving SBS in the k-th tier are, respectively, given by*

$$f^{\mathrm{DRSP}}_{\left|X_{o,\mathrm{M}}\right|}(x) = \frac{2\pi\lambda_{\mathrm{M}}x}{\Psi^{\mathrm{DRSP}}_{\mathrm{M}}} \exp\left(-\pi\lambda_{\mathrm{M}}x^2 - \pi\sum_{i=2}^{K}\lambda_i\hat{r}^2_{\mathrm{MS}}x^{\frac{2\alpha_{\mathrm{M}}}{\alpha_i}}\right), \tag{3.19}$$

and

$$f^{\mathrm{DRSP}}_{\left|X_{o,k}\right|}(y) = \frac{2\pi\lambda_k y}{\Psi^{\mathrm{DRSP}}_{k}} \times \exp\left(-\pi\lambda_{\mathrm{M}}\hat{r}^2_{\mathrm{SM}}y^{\frac{2\alpha_k}{\alpha_{\mathrm{M}}}} - \pi\sum_{i=2}^{K}\lambda_i\hat{r}^2_{\mathrm{SS}}y^{\frac{2\alpha_k}{\alpha_i}}\right), \tag{3.20}$$

in which $\hat{r}_{\mathrm{MS}} = \left(G^{\mathrm{D}}_a\frac{P_{\mathrm{M}}}{SP_i}\right)^{\frac{-1}{\alpha_i}}$ with $G^{\mathrm{D}}_a = (N+S-1)$, $\hat{r}_{\mathrm{SM}} = \left(\frac{SP_k}{G^{\mathrm{D}}_a P_{\mathrm{M}}}\right)^{\frac{-1}{\alpha_{\mathrm{M}}}}$, and $\hat{r}_{\mathrm{SS}} = \left(\frac{P_k}{P_i}\right)^{\frac{-1}{\alpha_i}}$. Also, in (3.19), $\Psi^{\mathrm{DRSP}}_{\mathrm{M}}$ is the probability that a typical user is associated with the MBS, given by

$$\Psi^{\mathrm{DRSP}}_{\mathrm{M}} = 2\pi\lambda_{\mathrm{M}} \times \int_0^{\infty} r\exp\left(-\pi\lambda_{\mathrm{M}}r^2 - \pi\sum_{i=2}^{K}\lambda_i\hat{r}^2_{\mathrm{MS}}r^{\frac{2\alpha_{\mathrm{M}}}{\alpha_i}}\right)dr, \tag{3.21}$$

and Ψ^{DRSP}_{k} is the probability that a typical user is associated with the SBS in the k-th tier, which is given by

$$\Psi^{\mathrm{DRSP}}_{k} = 2\pi\lambda_k \times \int_0^{\infty} r\exp\left(-\pi\lambda_{\mathrm{M}}\hat{r}^2_{\mathrm{SM}}r^{\frac{2\alpha_k}{\alpha_{\mathrm{M}}}} - \pi\sum_{i=2}^{K}\lambda_i\hat{r}^2_{\mathrm{SS}}r^{\frac{2\alpha_k}{\alpha_i}}\right)dr. \tag{3.22}$$

Proof. See Appendix II-A. □

Based on (3.21), we obtain a simplified asymptotic expression for the probability in the following corollary.

Corollary 5. *For large number of antennas with $N \to \infty$, using the Taylor series expansion truncated to the first order, the probability that a typical user is associated*

with the MBS given by (3.21) *is asymptotically derived as*

$$\Psi_{\mathrm{M}_\infty}^{\mathrm{DRSP}} = 2\pi\lambda_{\mathrm{M}} \times \left(\int_0^\infty r \exp\left(-\pi\lambda_{\mathrm{M}} r^2\right) dr - \pi \sum_{i=2}^{K} \lambda_i \hat{r}_{\mathrm{MS}}^2 \int_0^\infty r^{1+\frac{2\alpha_{\mathrm{M}}}{\alpha_i}} \exp\left(-\pi\lambda_{\mathrm{M}} r^2\right) dr \right), \tag{3.23}$$

which can be expressed as

$$\Psi_{\mathrm{M}_\infty}^{\mathrm{DRSP}} = 1 - \pi \sum_{i=2}^{K} \lambda_i \hat{r}_{\mathrm{MS}}^2 \frac{\Gamma\left(1+\frac{\alpha_{\mathrm{M}}}{\alpha_i}\right)}{\left(\pi\lambda_{\mathrm{M}}\right)^{\frac{\alpha_{\mathrm{M}}}{\alpha_i}}}. \tag{3.24}$$

Note that the probability for a user associated with the SBS is $1 - \Psi_{\mathrm{M}_\infty}^{\mathrm{DRSP}}$. *From* (3.24)*, it is explicitly shown that the probability for a user associated with the MBS increases with the density of MBS but decreases with the density of SBS.*

Likewise, in the case of the URSP-based user association, we have the following lemma and corollary. As the approaches are similar, their proofs are omitted.

Lemma 7. *Under URSP-based user association, the PDFs of the distance* $\left|X_{o,\mathrm{M}}\right|$ *between a typical user and its serving MBS and the distance* $\left|X_{o,k}\right|$ *between a typical user and its serving SBS in the k-th tier are, respectively, given by*

$$f_{\left|X_{o,\mathrm{M}}\right|}^{\mathrm{URSP}}(x) = \frac{2\pi x}{\Psi_{\mathrm{M}}^{\mathrm{URSP}}} \lambda_{\mathrm{M}} \times \exp\left(-\pi\lambda_{\mathrm{M}} x^2 - \pi \sum_{i=2}^{K} \lambda_i \widetilde{r}_{\mathrm{MS}}^2 x^{\frac{2\alpha_{\mathrm{M}}}{\alpha_i}} \right), \tag{3.25}$$

and

$$f_{\left|X_{o,k}\right|}^{\mathrm{URSP}}(y) = \frac{2\pi y}{\Psi_{k}^{\mathrm{URSP}}} \lambda_k \times \exp\left(-\pi\lambda_{\mathrm{M}} \widetilde{r}_{\mathrm{SM}}^2 y^{\frac{2\alpha_k}{\alpha_{\mathrm{M}}}} - \pi \sum_{i=2}^{K} \lambda_i y^{\frac{2\alpha_k}{\alpha_i}} \right), \tag{3.26}$$

where $\widetilde{r}_{\mathrm{MS}} = \left(G_a^{\mathrm{U}}\right)^{\frac{-1}{\alpha_i}}$ *with* $G_a^{\mathrm{U}} = (N - S + 1)$*, and* $\widetilde{r}_{\mathrm{SM}} = \left(\frac{1}{G_a^{\mathrm{U}}}\right)^{\frac{-1}{\alpha_{\mathrm{M}}}}$. *Also, in the above expressions, we have*

$$\Psi_{\mathrm{M}}^{\mathrm{URSP}} = 2\pi\lambda_{\mathrm{M}} \times \int_0^\infty r \exp\left(-\pi\lambda_{\mathrm{M}} r^2 - \pi \sum_{i=2}^{K} \lambda_i \widetilde{r}_{\mathrm{MS}}^2 r^{\frac{2\alpha_{\mathrm{M}}}{\alpha_i}} \right) dr, \tag{3.27}$$

$$\widetilde{\mathrm{E}}_{o,\mathrm{M}}^{\mathrm{DRSP}}(x)=\tau T\eta\times\Bigg\{(N+S-1)\frac{P_{\mathrm{M}}}{S}\beta\left(\mathbf{1}(x\leq d)\,d^{-\alpha_{\mathrm{M}}}+\mathbf{1}(x>d)\,x^{-\alpha_{\mathrm{M}}}\right)$$
$$+P_{\mathrm{M}}\beta 2\pi\lambda_{\mathrm{M}}\left(\mathbf{1}(x\leq d)\left(d^{-\alpha_{\mathrm{M}}}\frac{(d^2-x^2)}{2}-\frac{d^{2-\alpha_{\mathrm{M}}}}{2-\alpha_{\mathrm{M}}}\right)-\mathbf{1}(x>d)\,\frac{x^{2-\alpha_{\mathrm{M}}}}{2-\alpha_{\mathrm{M}}}\right)$$
$$+\sum_{i=2}^{K}P_i\beta 2\pi\lambda_i\left(\mathbf{1}(x\leq d_o)\left(d^{-\alpha_i}\frac{\left(d^2-\hat{r}_{\mathrm{MS}}^2x^{\frac{2\alpha_{\mathrm{M}}}{\alpha_i}}\right)}{2}-\frac{d^{2-\alpha_i}}{2-\alpha_i}\right)-\mathbf{1}(x>d_o)\,\frac{\hat{r}_{\mathrm{MS}}^{(2-\alpha_i)}x^{\frac{\alpha_{\mathrm{M}}(2-\alpha_i)}{\alpha_i}}}{2-\alpha_i}\right)\Bigg\}, \tag{3.30}$$

and

$$\Psi_k^{\mathrm{URSP}}=2\pi\lambda_k\times\int_0^{\infty}r\exp\left(-\pi\lambda_{\mathrm{M}}\widetilde{r}_{\mathrm{SM}}^2r^{\frac{2\alpha_k}{\alpha_{\mathrm{M}}}}-\pi\sum_{i=2}^{K}\lambda_ir^{\frac{2\alpha_k}{\alpha_i}}\right)dr. \tag{3.28}$$

Corollary 6. *For URSP-based user association, with large N, the asymptotic expression for the probability that a typical user is associated with the MBS given by* (3.27) *can be expressed as*

$$\Psi_{\mathrm{M}_\infty}^{\mathrm{URSP}}=1-\pi\sum_{i=2}^{K}\lambda_i\widetilde{r}_{\mathrm{MS}}^2\frac{\Gamma\left(1+\frac{\alpha_{\mathrm{M}}}{\alpha_i}\right)}{(\pi\lambda_{\mathrm{M}})^{\frac{\alpha_{\mathrm{M}}}{\alpha_i}}}. \tag{3.29}$$

In addition, the probability that a user is associated with the SBS can be directly found by $1-\Psi_{\mathrm{M}_\infty}^{\mathrm{URSP}}$.

3.4.2 Average Harvested Energy

Using DRSP-based user association, the maximum average harvested energy can be achieved. Here, we first derive the conditional expression of the average harvested energy given the distance between a typical user and its serving BS.

Theorem 1. *For the case of DRSP-based user association, given the distances* $\left|X_{o,\mathrm{M}}\right|=x$ *and* $\left|X_{o,k}\right|=y$*, the conditional expressions of the average harvested energy for a typical user that is associated with an MBS and that for a typical user that is associated with an SBS in the k-th tier are, respectively, given by* (3.30)

$$\widetilde{\mathrm{E}}_{o,k}^{\mathrm{DRSP}}(y)=\tau T\eta\times\Bigg\{P_k\beta\left(\mathbf{1}(y\le d)\,d^{-\alpha_k}+\mathbf{1}(y>d)\,y^{-\alpha_k}\right)$$
$$+P_{\mathrm{M}}\beta 2\pi\lambda_{\mathrm{M}}\left(\mathbf{1}(y\le d_1)\left(d^{-\alpha_{\mathrm{M}}}\frac{\left(d^2-\hat{r}_{\mathrm{SM}}^2y^{\frac{2\alpha_k}{\alpha_{\mathrm{M}}}}\right)}{2}-\frac{d^{2-\alpha_{\mathrm{M}}}}{2-\alpha_{\mathrm{M}}}\right)-\mathbf{1}(y>d_1)\,\frac{\hat{r}_{\mathrm{SM}}^{2-\alpha_{\mathrm{M}}}y^{\frac{\alpha_k(2-\alpha_{\mathrm{M}})}{\alpha_{\mathrm{M}}}}}{2-\alpha_{\mathrm{M}}}\right)$$
$$+\sum_{i=2}^{K}\beta 2\pi\lambda_i\left(\mathbf{1}(y\le d_2)\left(d^{-\alpha_i}\frac{\left(d^2-\hat{r}_{\mathrm{SS}}^2y^{\frac{2\alpha_k}{\alpha_i}}\right)}{2}-\frac{d^{2-\alpha_i}}{2-\alpha_i}\right)-\mathbf{1}(y>d_2)\,\frac{\hat{r}_{\mathrm{SS}}^{2-\alpha_i}y^{\frac{\alpha_k(2-\alpha_i)}{\alpha_i}}}{2-\alpha_i}\right)\Bigg\},\tag{3.31}$$

$$\overline{\mathrm{E}}_{o,\mathrm{M}_\infty}^{\mathrm{DRSP}}=\tau T\eta\times\Big\{(N+S-1)\,\frac{P_{\mathrm{M}}}{S}\beta\left(\Xi_1(d)\,d^{-\alpha_{\mathrm{M}}}+\Xi_2(d,-\alpha_{\mathrm{M}})\right)$$
$$+P_{\mathrm{M}}\beta 2\pi\lambda_{\mathrm{M}}\left(d^{2-\alpha_{\mathrm{M}}}\frac{\alpha_{\mathrm{M}}}{2(\alpha_{\mathrm{M}}-2)}\Xi_1(d)-\frac{d^{-\alpha_{\mathrm{M}}}}{2}\Xi_3(d,2)+\frac{\Xi_2(d,2-\alpha_{\mathrm{M}})}{\alpha_{\mathrm{M}}-2}\right)$$
$$+\sum_{i=2}^{K}P_i\beta 2\pi\lambda_i\times$$
$$\left(d^{2-\alpha_i}\frac{\alpha_i}{2(\alpha_i-2)}\Xi_1(d_o)-\frac{d^{-\alpha_i}\hat{r}_{\mathrm{MS}}^2}{2}\Xi_3\left(d_o,\frac{2\alpha_{\mathrm{M}}}{\alpha_i}\right)+\frac{\hat{r}_{\mathrm{MS}}^{(2-\alpha_i)}}{\alpha_i-2}\Xi_2\left(d_o,\frac{\alpha_{\mathrm{M}}(2-\alpha_i)}{\alpha_i}\right)\right)\Big\},\tag{3.32}$$

---

and (3.31) *at the top of next page,* $d_o=(\hat{r}_{\mathrm{MS}})^{-\frac{\alpha_i}{\alpha_{\mathrm{M}}}}d^{\alpha_i/\alpha_{\mathrm{M}}}$, $d_1=(\hat{r}_{\mathrm{SM}})^{\frac{-\alpha_{\mathrm{M}}}{\alpha_k}}d^{\alpha_{\mathrm{M}}/\alpha_k}$, *and* $d_2=(\hat{r}_{\mathrm{SS}})^{\frac{-\alpha_i}{\alpha_k}}d^{\alpha_i/\alpha_k}$. $\mathbf{1}(\cdot)$ *denotes the indicator function, and* $\mathbb{E}\{\cdot\}$ *denotes the expectation operator.*

Proof. See Appendix II-B. □

Based on Theorem 1, the average harvested energy for a user that is associated with an MBS and that a user that is associated with an SBS in the k-th tier are found as

$$\overline{\mathrm{E}}_{o,\mathrm{M}}^{\mathrm{DRSP}}=\int_0^\infty\widetilde{\mathrm{E}}_{o,\mathrm{M}}^{\mathrm{DRSP}}(x)\,f^{\mathrm{DRSP}}_{|X_{o,\mathrm{M}}|}(x)dx,\tag{3.33}$$

and

$$\overline{\mathrm{E}}_{o,k}^{\mathrm{DRSP}} = \int_0^{\infty} \widetilde{\mathrm{E}}_{o,k}^{\mathrm{DRSP}}(y)\, f_{|X_{o,k}|}^{\mathrm{DRSP}}(y) dy. \tag{3.34}$$

Corollary 7. *When the number of antennas at the MBS grows large, we obtain the asymptotic expression for* $\overline{\mathrm{E}}_{o,\mathrm{M}}^{\mathrm{DRSP}}$ *in* (3.33) *as* (3.32) *(see next page), where* $\Xi_1(\cdot)$, $\Xi_2(\cdot,\cdot)$ *and* $\Xi_3(\cdot,\cdot)$ *are, respectively, given by*

$$\Xi_1(x) = \frac{1}{\Psi_{\mathrm{M}_\infty}^{\mathrm{DRSP}}} \times \left(1 - e^{-\pi\lambda_{\mathrm{M}}x^2} - \pi \sum_{i=2}^{K} \lambda_i \hat{r}_{\mathrm{MS}}^2 \frac{\gamma\left(1+\frac{\alpha_{\mathrm{M}}}{\alpha_i}, \pi\lambda_{\mathrm{M}}x^2\right)}{(\pi\lambda_{\mathrm{M}})^{\frac{\alpha_{\mathrm{M}}}{\alpha_i}}}\right), \tag{3.35}$$

$$\Xi_2(a,b) = \frac{1}{\Psi_{\mathrm{M}_\infty}^{\mathrm{DRSP}}} \left(\frac{\Gamma\left(1+\frac{b}{2}, \pi\lambda_{\mathrm{M}}a^2\right)}{(\pi\lambda_{\mathrm{M}})^{\frac{b}{2}}} - \pi \sum_{i=2}^{K} \lambda_i \hat{r}_{\mathrm{MS}}^2 \frac{\Gamma\left(1+\frac{\alpha_{\mathrm{M}}}{\alpha_i}+\frac{b}{2}, \pi\lambda_{\mathrm{M}}a^2\right)}{(\pi\lambda_{\mathrm{M}})^{\frac{\alpha_{\mathrm{M}}}{\alpha_i}+\frac{b}{2}}}\right), \tag{3.36}$$

and

$$\Xi_3(c,d) = \frac{1}{\Psi_{\mathrm{M}_\infty}^{\mathrm{DRSP}}} \left(\frac{\gamma\left(1+\frac{d}{2}, \pi\lambda_{\mathrm{M}}c^2\right)}{(\pi\lambda_{\mathrm{M}})^{\frac{d}{2}}} - \pi \sum_{i=2}^{K} \lambda_i \hat{r}_{\mathrm{MS}}^2 \frac{\gamma\left(1+\frac{\alpha_{\mathrm{M}}}{\alpha_i}+\frac{d}{2}, \pi\lambda_{\mathrm{M}}c^2\right)}{(\pi\lambda_{\mathrm{M}})^{\frac{\alpha_{\mathrm{M}}}{\alpha_i}+\frac{d}{2}}}\right), \tag{3.37}$$

where $\gamma(\cdot,\cdot)$ *and* $\Gamma(\cdot,\cdot)$ *are the upper and lower incomplete gamma functions, respectively [80, (8.350)],* $\Gamma(\vartheta,\theta)$ *denotes the gamma distribution with shape* ϑ *and scale* θ, $\exp(z)$ *denotes the exponential distribution with the parameter z.*

Proof. See Appendix II-C. □

Overall, for a user in the massive MIMO aided HetNets with DRSP-based user association, its average harvested energy can be calculated as

$$\overline{\mathrm{E}}_{o,\mathrm{HetNet}}^{\mathrm{DRSP}} = \Psi_{\mathrm{M}}^{\mathrm{DRSP}} \overline{\mathrm{E}}_{o,\mathrm{M}}^{\mathrm{DRSP}} + \sum_{k=2}^{K} \Psi_k^{\mathrm{DRSP}} \overline{\mathrm{E}}_{o,k}^{\mathrm{DRSP}}. \tag{3.38}$$

Similarly, for the case of URSP-based user association, the average harvested energy for a typical user that is associated with an MBS and that for a typical user that is associated with an SBS in the k-th tier are, respectively, given by

$$\overline{\mathrm{E}}_{o,\mathrm{M}}^{\mathrm{URSP}} = \int_0^{\infty} \widetilde{\mathrm{E}}_{o,\mathrm{M}}^{\mathrm{URSP}}(x)\, f_{\left|X_{o,\mathrm{M}}\right|}^{\mathrm{URSP}}(x)dx, \tag{3.39}$$

and

$$\overline{\mathrm{E}}_{o,k}^{\mathrm{URSP}} = \int_0^{\infty} \widetilde{\mathrm{E}}_{o,k}^{\mathrm{URSP}}(y)\, f_{\left|X_{o,k}\right|}^{\mathrm{URSP}}(y)dy, \tag{3.40}$$

where $\widetilde{\mathrm{E}}_{o,\mathrm{M}}^{\mathrm{URSP}}(x)$ and $\widetilde{\mathrm{E}}_{o,k}^{\mathrm{URSP}}(y)$ are obtained by interchanging the parameters $\hat{r}_{\mathrm{MS}} \to \widetilde{r}_{\mathrm{MS}}$, $\hat{r}_{\mathrm{SM}} \to \widetilde{r}_{\mathrm{SM}}$ and $\hat{r}_{\mathrm{SS}} \to 1$ in (3.30) and (3.31), respectively, $f_{\left|X_{o,\mathrm{M}}\right|}^{\mathrm{URSP}}(x)$ and $f_{\left|X_{o,k}\right|}^{\mathrm{URSP}}(y)$ are given by (3.25) and (3.26), respectively.

Corollary 8. *If the number of antennas at the MBS is large for URSP-based user association, then we obtain the asymptotic expression for* $\overline{\mathrm{E}}_{o,\mathrm{M}}^{\mathrm{URSP}}$ *by interchanging* $\Psi_{\mathrm{M}_\infty}^{\mathrm{DRSP}} \to \Psi_{\mathrm{M}_\infty}^{\mathrm{URSP}}$ *and* $\hat{r}_{\mathrm{MS}} \to \widetilde{r}_{\mathrm{MS}}$ *in* (3.32).

Overall, for a user in the massive MIMO aided HetNets with URSP-based user association, its average harvested energy is calculated as

$$\overline{\mathrm{E}}_{o,\mathrm{HetNet}}^{\mathrm{URSP}} = \Psi_{\mathrm{M}}^{\mathrm{URSP}} \overline{\mathrm{E}}_{o,\mathrm{M}}^{\mathrm{URSP}} + \sum_{k=2}^{K} \Psi_k^{\mathrm{URSP}} \overline{\mathrm{E}}_{o,k}^{\mathrm{URSP}}. \tag{3.41}$$

3.5 Uplink Performance Evaluation

After harvesting the energy, users transmit their messages to the serving BSs with a stable transmit power constrained by (3.18).[6] In this section, we analyze the uplink WIT performance in terms of average achievable rate. On the one hand, given a specific user's transmit power, URSP-based user association outperforms the DRSP-based in the uplink by maximizing the uplink received signal power. On the other hand, compared to URSP-based user association, DRSP-based user association allows users to set a higher stable transmit power due to more harvested

[6]It is indicated from (3.18) that the power transfer time allocation factor τ has to be large enough, in order to avoid the power outage.

energy. Thus, it is necessary to evaluate the uplink achievable rate under these two user association schemes.

We assume that each user intends to set the maximum stable transmit power to achieve the maximum achievable rate. For DRSP-based user association, the transmit power for user i in a macrocell is $P_{u_i}^{\mathrm{DRSP}} = P_{u_{\mathrm{M}}}^{\mathrm{DRSP}} = \frac{\overline{\mathrm{E}}_{o,\mathrm{M}}^{\mathrm{DRSP}}}{(1-\tau)T}$, and the transmit power for user j in a small cell of the k-th tier is $P_{u_j}^{\mathrm{DRSP}} = P_{u_k}^{\mathrm{DRSP}} = \frac{\overline{\mathrm{E}}_{o,k}^{\mathrm{DRSP}}}{(1-\tau)T}$, where $\overline{\mathrm{E}}_{o,\mathrm{M}}^{\mathrm{DRSP}}$ and $\overline{\mathrm{E}}_{o,k}^{\mathrm{DRSP}}$ are given by (3.33) and (3.34), respectively. For URSP-based user association, the transmit power for user i in a macrocell is $P_{u_i}^{\mathrm{URSP}} = P_{u_{\mathrm{M}}}^{\mathrm{URSP}} = \frac{\overline{\mathrm{E}}_{o,\mathrm{M}}^{\mathrm{URSP}}}{(1-\tau)T}$, and the transmit power for user j in a small cell of the k-th tier is $P_{u_j}^{\mathrm{URSP}} = P_{u_k}^{\mathrm{URSP}} = \frac{\overline{\mathrm{E}}_{o,k}^{\mathrm{URSP}}}{(1-\tau)T}$, in which $\overline{\mathrm{E}}_{o,\mathrm{M}}^{\mathrm{URSP}}$ and $\overline{\mathrm{E}}_{o,k}^{\mathrm{URSP}}$ are given by (3.39) and (3.40), respectively.

3.5.1 Average Uplink Achievable Rate

We first present the achievable rate for the massive MIMO HetNet uplink with DRSP-based user association and have the following theorems.

Theorem 2. *Given a distance $\left|X_{o,\mathrm{M}}\right| = x$, a tractable lower bound for the conditional average uplink achievable rate between a typical user and its serving MBS can be found as*

$$R_{\mathrm{DRSP,M}}^{\mathrm{low}}(x) = (1-\tau)\log_2\left(1 + P_{u_{\mathrm{M}}}^{\mathrm{DRSP}}(N-S+1)\frac{\Delta_1(x)}{\Lambda_{\mathrm{DRSP}}}\right), \tag{3.42}$$

where $\Delta_1(x) = \beta\left(\mathbf{1}(x \le d)\, d^{-\alpha_{\mathrm{M}}} + \mathbf{1}(x > d)\, x^{-\alpha_{\mathrm{M}}}\right)$ and

$$\Lambda_{\mathrm{DRSP}} = 2\pi\beta\left(P_{u_{\mathrm{M}}}^{\mathrm{DRSP}}(S\lambda_{\mathrm{M}}) + \sum_{i=2}^{K} P_{u_i}^{\mathrm{DRSP}}\lambda_i\right) \times \left(\frac{d^{2-\alpha_{\mathrm{M}}}}{2} + \frac{d^{2-\alpha_{\mathrm{M}}}}{\alpha_{\mathrm{M}}-2}\right) + \delta^2. \tag{3.43}$$

Proof. See Appendix II-D. □

Theorem 3. *Given a distance $\left|X_{o,k}\right| = y$, the conditional average uplink achievable rate between a typical user and its serving SBS in the k-th tier is given by*

$$R_{\mathrm{DRSP},k}(y) = \frac{(1-\tau)}{\ln 2}\int_0^{\infty} \frac{\bar{F}_{\mathrm{SINR}}(x)}{1+x}dx, \tag{3.44}$$

$$\Omega(s)=\pi(S\lambda_{\mathrm{M}})\frac{sP_{u_{\mathrm{M}}}^{\mathrm{DRSP}}\beta d^{-\alpha_i}}{1+sP_{u_{\mathrm{M}}}^{\mathrm{DRSP}}\beta d^{-\alpha_i}}d^2+2\pi(S\lambda_{\mathrm{M}})sP_{u_{\mathrm{M}}}^{\mathrm{DRSP}}\beta\frac{d^{2-\alpha_i}}{\alpha_i-2}{}_2F_1\left[1,\frac{\alpha_i-2}{\alpha_i};2-\frac{2}{\alpha_i};-sP_{u_{\mathrm{M}}}^{\mathrm{DRSP}}\beta d^{-}\right.$$
$$\left.+\sum_{i=2}^{K}\pi\lambda_i\frac{sP_{u_i}^{\mathrm{DRSP}}\beta d^{-\alpha_i}}{1+sP_{u_i}^{\mathrm{DRSP}}\beta d^{-\alpha_i}}d^2+\sum_{i=2}^{K}2\pi\lambda_i sP_{u_i}^{\mathrm{DRSP}}\beta\frac{d^{2-\alpha_i}}{\alpha_i-2}{}_2F_1\left[1,\frac{\alpha_i-2}{\alpha_i};2-\frac{2}{\alpha_i};-sP_{u_i}^{\mathrm{DRSP}}\beta d^{-\alpha_i}\right]\right. \tag{3.47}$$

---

where

$$\bar{F}_{\mathrm{SINR}}(x)=e^{-\frac{x\delta^2}{P_{u_k}^{\mathrm{DRSP}}\Delta_2(y)}-\Omega\left(\frac{x}{P_{u_k}^{\mathrm{DRSP}}\Delta_2(y)}\right)} \tag{3.45}$$

is the complementary cumulative distribution function (CCDF) of the received SINR, in which

$$\Delta_2(y)=\beta\left(\mathbf{1}(y\le d)d^{-\alpha_k}+\mathbf{1}(y>d)x^{-\alpha_k}\right), \tag{3.46}$$

and $\Omega(\cdot)$ *is given by* (3.47) *(see next page). In* (3.47), ${}_2F_1[\cdot,\cdot;\cdot;\cdot]$ *is the Gauss hypergeometric function [80, (9.142)].*

Proof. See Appendix II-E. □

With the help of Theorem 2 and Theorem 3, the lower bound for the average uplink achievable rate between a typical user and its serving MBS can be expressed as

$$\overline{R}_{\mathrm{DRSP,M}}^{\mathrm{low}}=\int_0^{\infty}R_{\mathrm{DRSP,M}}^{\mathrm{low}}(x)\,f_{|X_{o,\mathrm{M}}|}^{\mathrm{DRSP}}(x)dx, \tag{3.48}$$

and the average uplink achievable rate between a typical user and its serving SBS in the k-th tier is given by

$$\overline{R}_{\mathrm{DRSP},k}=\int_0^{\infty}R_{\mathrm{DRSP},k}(y)\,f_{|X_{o,k}|}^{\mathrm{DRSP}}(y)dy. \tag{3.49}$$

Overall, a lower bound on the average uplink achievable rate for a user in the

massive MIMO aided HetNets with DRSP-based user association is calculated as

$$\overline{R}^{\text{low}}_{\text{DRSP,HetNet}} = \Psi^{\text{DRSP}}_{\text{M}} \overline{R}^{\text{low}}_{\text{DRSP,M}} + \sum_{k=2}^{K} \Psi^{\text{DRSP}}_{k} \overline{R}_{\text{DRSP},k}. \tag{3.50}$$

For URSP-based user association, the lower bound for the average uplink achievable rate between a typical user and its serving MBS $\overline{R}^{\text{low}}_{\text{URSP,M}}$ can be directly determined by interchanging the transmit power parameters $P^{\text{DRSP}}_{u_{\text{M}}} \to P^{\text{URSP}}_{u_{\text{M}}}$, $P^{\text{DRSP}}_{u_i} \to P^{\text{URSP}}_{u_i}$, and the PDF $f^{\text{DRSP}}_{|X_{o,\text{M}}|}(x) \to f^{\text{URSP}}_{|X_{o,\text{M}}|}(x)$ in (3.48), and the average uplink achievable rate between a typical user and its serving SBS in the k-th tier $\overline{R}_{\text{URSP},k}$ is obtained by interchanging the transmit power parameters $P^{\text{DRSP}}_{u_{\text{M}}} \to P^{\text{URSP}}_{u_{\text{M}}}$, $P^{\text{DRSP}}_{u_i} \to P^{\text{URSP}}_{u_i}$, and the PDF $f^{\text{DRSP}}_{|X_{o,k}|}(y) \to f^{\text{URSP}}_{|X_{o,k}|}(y)$ in (3.49). As such, a lower bound on the average uplink achievable rate for a user in the massive MIMO aided HetNets with URSP-based user association is obtained as

$$\overline{R}^{\text{low}}_{\text{URSP,HetNet}} = \Psi^{\text{URSP}}_{\text{M}} \overline{R}^{\text{low}}_{\text{URSP,M}} + \sum_{k=2}^{K} \Psi^{\text{URSP}}_{k} \overline{R}_{\text{URSP},k}. \tag{3.51}$$

3.6 Numerical Results

In this section, we present numerical results to examine the impact of different user association schemes and key system parameters on the harvested energy and the uplink achievable rate. We consider a two-tier HetNet consisting of macrocells and picocells. The network is assumed to operate at $f_c = 1$GHz (f_c is the carrier frequency); the bandwidth (BW) is assumed 10MHz, the density of MBSs is $\lambda_{\text{M}} = 10^{-3}$; the density of pico BSs (PBSs) λ_2 is proportional to λ_{M}; the MBS's transmit power is $P_{\text{M}} = 46$dBm; the noise figure is Nf $= 10$dB, the noise power is $\sigma^2 = -170 + 10\log_{10}(\text{BW}) + \text{Nf} = -90$dBm; the frequency dependent value $\beta = (\frac{\text{c}}{4\pi f_c})^2$ with $c = 3 \times 10^8 \text{m/s}$; and the energy conversion efficiency is $\eta = 0.9$. In the figures, Monte Carlo simulations are marked with '$\circ$'.

3.6.1 User Association

Results in Fig. 3.2 are provided for the association probability that a user is associated with MBS for various number of MBS antennas. In the results, the path loss

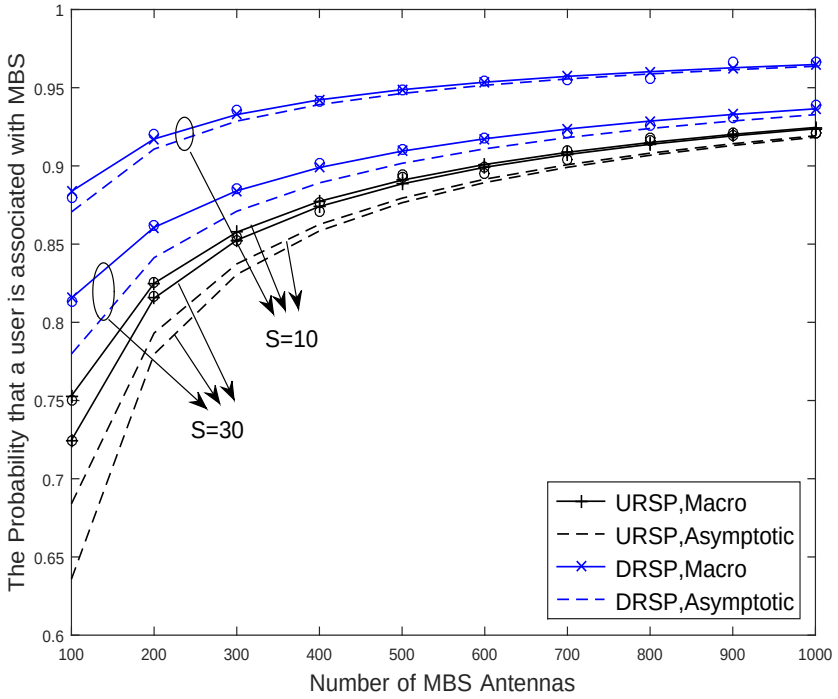

Figure 3.2: Association probability versus the number of antennas for the MBS.

exponents were set to $\alpha_{\mathrm{M}} = 3.5$, $\alpha_2 = 4$, and $\lambda_2 = 5 \times \lambda_{\mathrm{M}}$. The solid curves are obtained from (3.21) and (3.27) for the DRSP-based and URSP-based user association schemes, respectively, and the dash curves are obtained from the corresponding (3.24) and (3.29), respectively. As we see, our asymptotic expressions can well approximate the exact ones. Also, compared to the URSP-based user association, users are more likely to be served in the macrocells by using DRSP-based user association. The reason is that for DRSP-based user association, MBS provides larger received power. The probability that a user is associated with an MBS increases with the number of MBS antennas, due to the increase of power gain. By increasing S, the probability that a user is served by an MBS is reduced due to the decrease of MBS transmit power allocated to each user $\left(\frac{P_{\mathrm{M}}}{S}\right)$.

3.6.2 Downlink Energy Harvesting

In this subsection, we investigate the energy harvesting performance for different user association schemes presented in Section 3.4. In the simulations, the block time T is normalized to 1, while the time allocation factor is $\tau = 0.6$, and the path

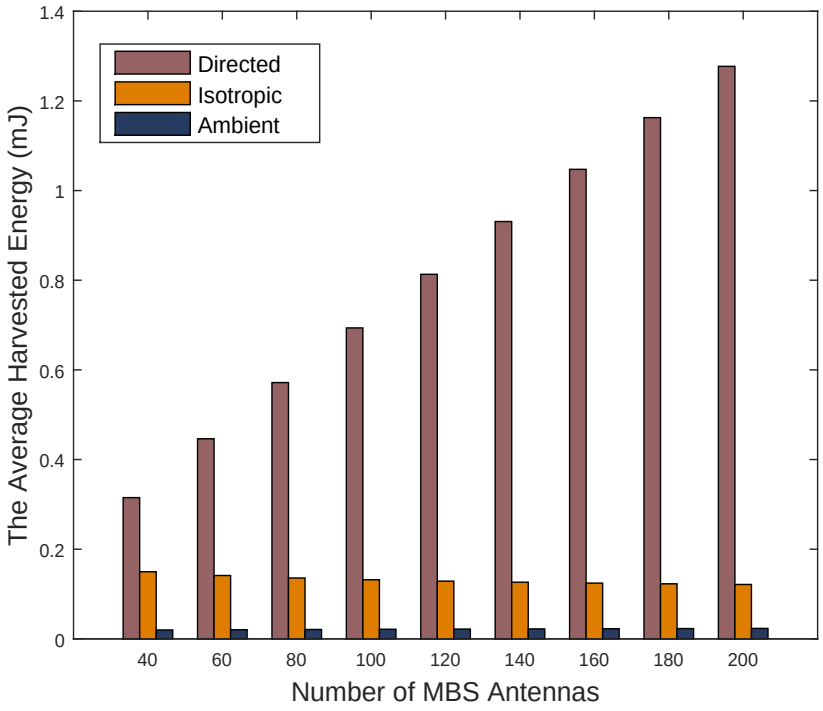

Figure 3.3: The average harvested energy against the number of antennas.

loss exponents are $\alpha_{\mathrm{M}} = 3$ and $\alpha_2 = 3.5$.

Fig. 3.3 shows the average energy harvested from the directed WPT, isotropic WPT, and ambient RF for a user associated with MBS based on the DRSP-based user association. The PBS transmit power is $P_2 = 30$ dBm, the density of PBSs is $\lambda_2 = 20 \times \lambda_{\mathrm{M}}$, and $S = 20$. We observe that compared to isotropic WPT and ambient RF, the directed WPT plays a dominate role in harvesting energy. The average energy harvested from the directed WPT increases with the number of antennas, due to more power gains. The amount of harvested energy from the ambient RF is nearly unaltered when increasing the MBS antennas. However, the average energy harvested from the isotropic WPT slightly decreases with MBS antennas. The reason is that the coverage of the macrocell is expanded by adding more MBS antennas, and the distance between a user and its associated MBS becomes larger on average, which has an adverse effect on the isotropic WPT.

Fig. 3.4 shows the average harvested energy of a user associated with the MBS versus the number of MBS antennas. The PBS transmit power is $P_2 = 30$dBm and

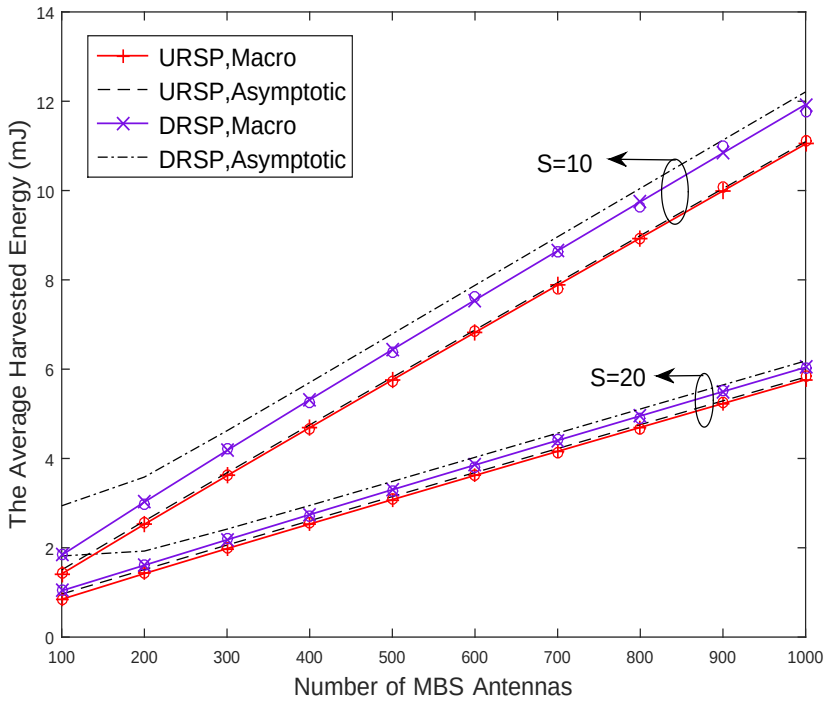

Figure 3.4: The average harvested energy against the number of antennas for the MBS.

the density of PBSs is $\lambda_2 = 20 \times \lambda_{\mathrm{M}}$. The solid curves are obtained from (3.33) and (3.39), while the dash curves are obtained from (3.32) and Corollary 4. We see that the asymptotic expressions can well predict the exact ones. The average harvested energy increases with the number of MBS antennas, but decreases with the number of users served by one MBS. This is because the power gain obtained by the user increases with the number of antennas, but the directed power transfer time allocated to each user decreases with the number of users served by the MBS. In addition, by URSP-based user association, user in the macrocell harvests more energy than in the case of the DRSP-based user association. The reason is that with DRSP-based user association, more users with low received power are loaded to the macrocells with increasing number of the MBS antennas.

Fig. 3.5 shows the average harvested energy of a user associated with the PBS versus the number of MBS antennas. Here we set $\lambda_2 = 20 \times \lambda_{\mathrm{M}}$ and $S = 5$. The solid curves are obtained from (3.34) and (3.40). We observe that the harvested energy increases with the number of MBS antennas, due to the fact that users with

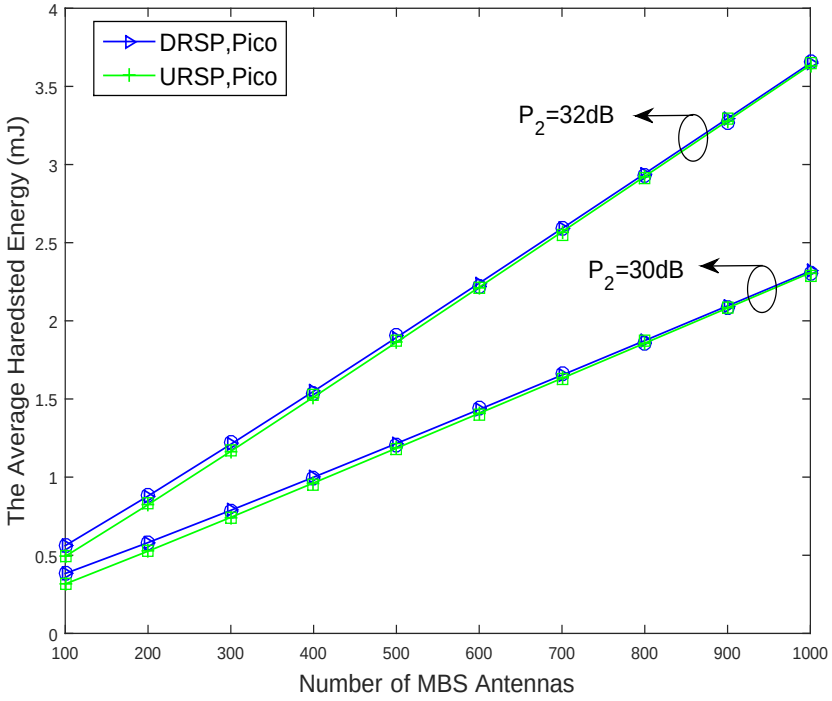

Figure 3.5: The average harvested energy against the number of antennas for the PBS.$\lambda_2 = 20 \times \lambda_{\mathrm{M}}$, $\lambda_3 = 30 \times \lambda_{\mathrm{M}}$,$S = 5$,$P_2 = 38$dBm,$P_3 = 35$dBm, $\alpha_3 = 3.8$

higher received power are connected to the picocells. Evidently, increasing the PBS transmit power brings an increase on the harvested energy. Moreover, the DRSP based user association outperforms the URSP-based one, since users loaded to the picocells have higher received power through DRSP based user association.

Fig. 5.2 provides the results for the average harvested energy of a user in the massive MIMO HetNet. Same as before, the solid curves are obtained from (3.38) and (3.41). It is observed that overall, DRSP-based user association harvests more energy than the URSP-based method, since DRSP-based user association seeks to maximize the received power for a user in the HetNet. In addition, serving more users in the macrocells decreases the harvested energy due to the shorter directed power transfer time allocated to each user.

Fig 3.7 shows the average harvested energy of a user in a three-tier massive MIMO HetNet. In the second and third tier, the densities of BSs are $\lambda_2 = 20\lambda_{\mathrm{M}}$ and $\lambda_3 = 50\lambda_{\mathrm{M}}$, and the BS transmit power are $P_2 = 30$ dBm, $P_3 = 20$ dBm, respec-

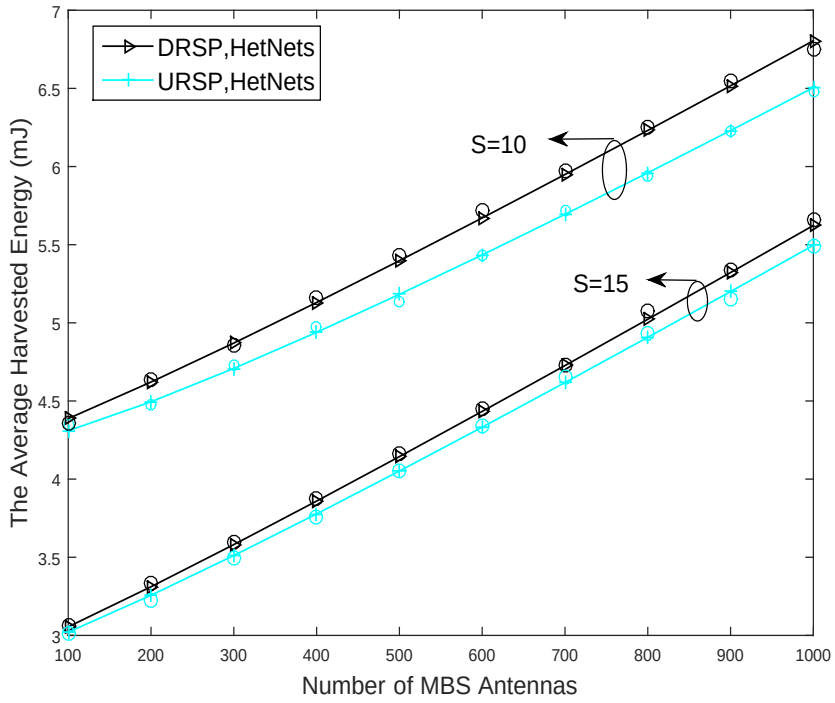

Figure 3.6: The average harvested energy against the number of antennas in the massive MIMO HetNet.

tively. We find that the amount of average harvested energy for users in the third tier including dense low-power base stations (BSs) is comparable with that in the second tier with high-power BSs, because the distances between the BSs and users are shortened. In addition, when adding the number of MBS antennas, the average harvested energy of a user in the second and third tier increases due to the fact that users with low received power are offloaded to macrocells.

3.6.3 Average Uplink Achievable Rate

In this section, we evaluate the average achievable rate in the uplink, as presented in Section 3.5. In the simulations, the time allocation factor is $\tau = 0.3$, and the path loss exponents are $\alpha_{\mathrm{M}} = 2.8$ and $\alpha_2 = 2.5$, $P_2 = 30$dBm and $S = 10$.

Fig. 3.8 shows the average uplink achievable rate of a user associated with the MBS versus the number of MBS antennas. The solid curves are obtained from (3.48) and its URSP-based counterpart. We observe that the average achievable rate increases with the number of MBS antennas, due to the increase of the power gain.

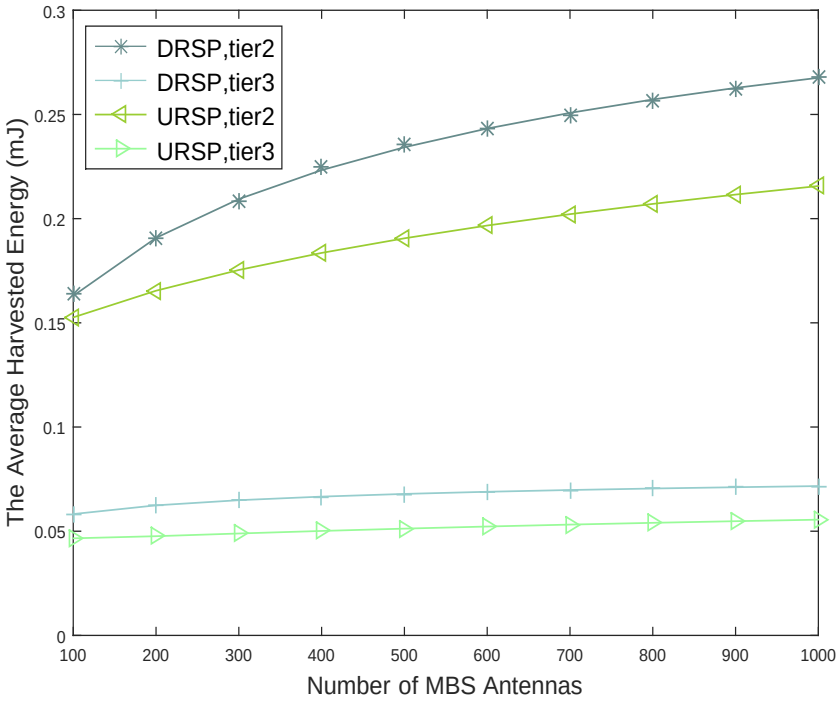

Figure 3.7: The average harvested energy against the number of antennas in a three-tier massive MIMO HetNet.$\lambda_2 = 20 \times \lambda_{\mathrm{M}}$, $\lambda_3 = 30 \times \lambda_{\mathrm{M}}$,$S = 5$,$P_2 = 38$dBm,$P_3 = 35$dBm, $\alpha_3 = 3.8$

For URSP-based user association, the average achievable rate also significantly increases with the density of PBSs. The reason is that when the PBSs become more dense, the distance between the user and the PBS is shorter and more users are associated with the PBS, and users with higher received power can be associated with the MBS. However, denser PBSs do not imply a bigger impact on the DRSP-based user association.

Fig. 3.9 shows the average uplink achievable rate of a user associated with the PBS versus the number of MBS antennas. The solid curves are obtained from (3.49) and its URSP-based counterpart. It is seen that the average achievable rate decreases with increasing the number of MBS antennas. The reason is that users in the macrocells harvest more energy and have higher transmit power, resulting in severer interference to the uplink in the picocells. In contrast to the performance in the macrocells, DRSP-based user association actually outperforms the URDP-based strategy in the picocells.

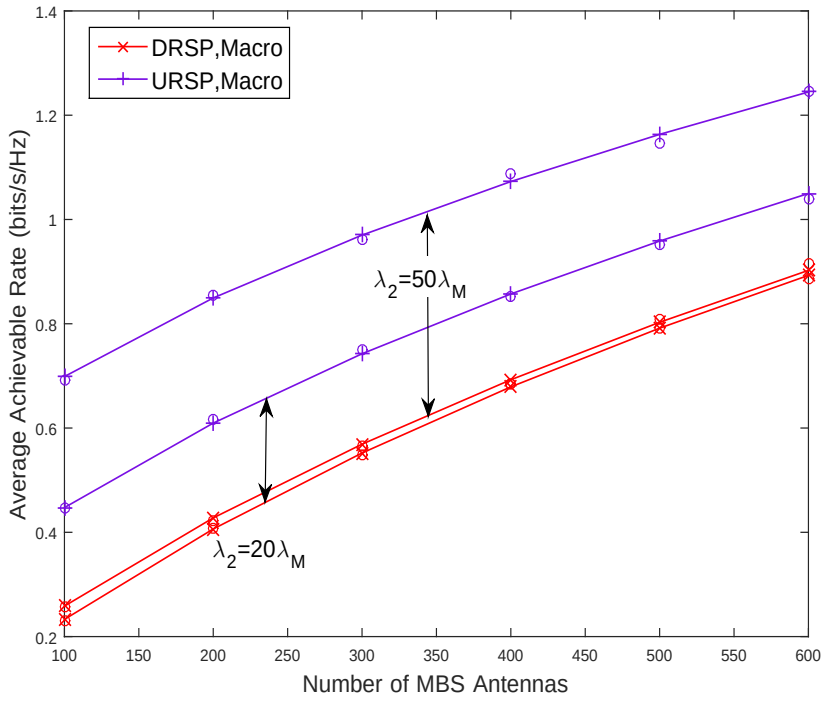

Figure 3.8: The average uplink achievable rate against the number of antennas for the MBS.

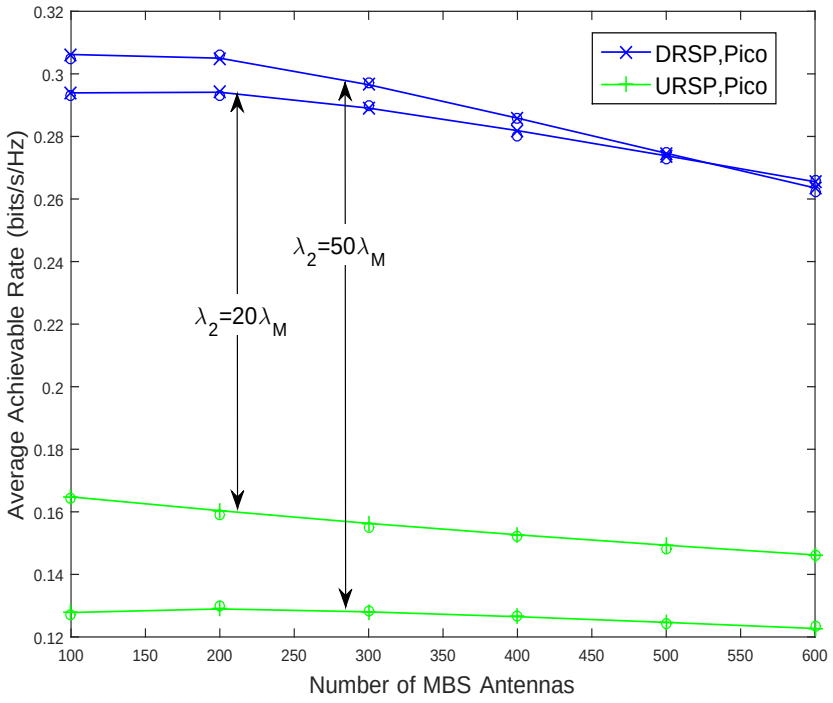

Figure 3.9: The average uplink achievable rate against the number of MBS antennas.

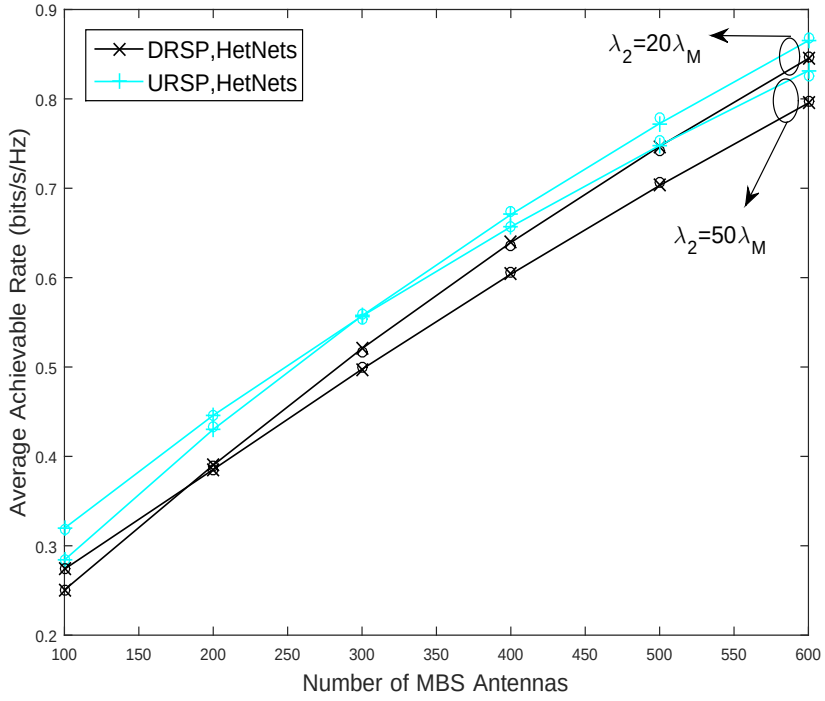

Figure 3.10: The average uplink achievable rate against the number of antennas in the massive MIMO HetNet.

Fig. 3.10 demonstrates the results for the average uplink achievable rate in the HetNet. The solid curves are obtained from (3.50) and (3.51). Results illustrate that the average rate increases with the number of MBS antennas. Nevertheless, without interference mitigation in the uplink, the deployment of more PBSs deteriorates the uplink performance, since more users are served and more uplink interference exists in the uplink WIT. More importantly, it is indicated that URSP-based user association can achieve better performance than the DRSP-based method, since it seeks to minimize the uplink path loss. An interesting phenomenon is observed that there is a crossover point, beyond which deploying more PBSs deteriorates the uplink performance due to more uplink interference.

Finally, Fig. 3.11 shows the average uplink achievable rate in the HetNet versus S. We see that URSP-based user association scheme outperforms the DRSP-based method, and increasing S decreases the average rate, due to more uplink interference and lower harvested energy as suggested in Fig 5.2.

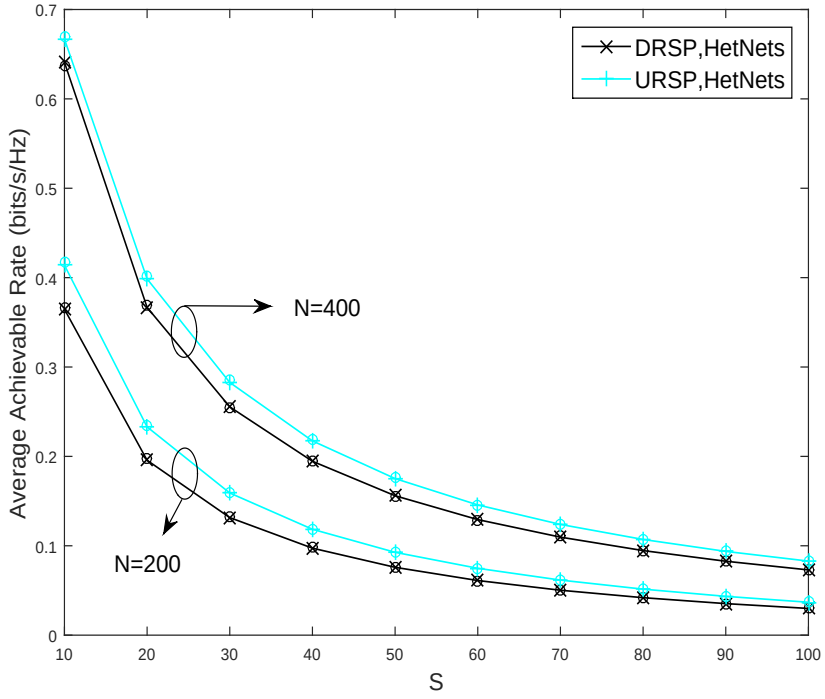

Figure 3.11: The average uplink achievable rate against the number of users in the massive MIMO HetNet.

3.7 Conclusions

In this chapter, we considered WPT in the massive MIMO enabled HetNets. A stochastic geometry approach was adopted to model the K-tier HetNets where massive MIMO antennas were employed in the macrocells. The effect of massive MIMO antennas on user association was investigated, and two specific user association schemes were analyzed. The downlink energy harvesting and uplink information transmission were evaluated in terms of average harvested energy and average achievable rate, respectively. Important insights were obtained.

Therefore, it is crucial to propose downlink WIT and downlink energy efficiency for performance enhancement, which could be our further work.

Chapter 4

Secure Communications in Millimeter Wave Ad Hoc Networks

4.1 Introduction

Wireless ad hoc networks have been widely applied in several areas including tactical networks, device-to-device, and personal area networking. Unfortunately, interference from nearby transmitters severely deteriorate the throughput of ad hoc networks either through reducing the link quality, or reducing the number of links that can operate simultaneously. Due to the lack of central coordination, beamforming or directional antennas are one approach for suppressing interference [35]. Recently, millimeter wave (mmWave) has been viewed as a promising technology for supporting high-speed data rate in the mobile cellular systems [36]. MmWave with directional transmissions and large bandwidths provides rich opportunities for ad hoc networks. Compared to the lower frequency counterpart, mmWave ad hoc networks experience less interference and achieve greater rate coverage [37].

Security in ad hoc networks is important [52]. The traditional higher-layer key distribution and management may increase the burden of transmitting confidential messages in such decentralized networks. Recent developments have shown that by leveraging the randomness inherent in wireless channels, physical layer security can be a low-complexity alternative for safeguarding complex wireless networks [53]. By taking advantage of unique mmWave channel features, this Chapter establishes

the potential of physical layer security in mmWave ad hoc networks.

4.2 Contribution

This Chapter studies physical layer security in mmWave ad hoc networks. Our analysis accounts for the key features of mmWave channel and the effects of different antenna array gains and node densities. The detailed contributions and insights are summarized as follows.

- We model the mmWave ad hoc networks with the help of stochastic geometry, to characterize the random spatial locations of transmitting nodes and eavesdroppers. The effect of blockage is also incorporated such that links are either line-of-sight (LoS) or non-line-of-sight (NLoS). The average achievable secrecy rate is derived to quantify the impacts of key system parameters such as antenna gain, transmitting node and eavesdropper densities on the secrecy performance. Our results show that with increasing transmit power, a transition from low mmWave frequency to high mmWave frequency is needed for achieving better secrecy performance. Compared to eavesdropping, the performance is dominated by the surrounding interference in the high node density case. The use of different mmWave frequencies has a big impact on the secrecy performance, which needs to be carefully selected in practice.

- We develop an approach to evaluate the average achievable secrecy rate when utilizing uniform linear array (ULA). Our results show that adding more antennas at the transmitting node degrades the signal strength at the eavesdroppers.

- We examine the impact of artificial noise on the secrecy rate. Our results show that in mmWave ad hoc networks, the use of artificial noise can still enhance the secrecy when power allocation between the information signal and artificial noise is properly set. Moreover, the use of artificial noise may have an adverse effect on the secrecy rate in the low node density scenarios, where more transmit power should be allocated to improve the transmission rate between the transmitting node and its intended receiver.

The remainder of this chapter is organized as follows. Section 4.3 presents the network and the mmWave channel model. Section 4.4 evaluates the average achievable secrecy rate of this network and also discusses the implementation of uniform linear array. Section 4.5 analyzes the use of artificial noise on the secrecy performance. Numerical results are provided in Section 4.6 and conclusion is drawn in Section 4.7.

4.3 System Description

Consider a mmWave ad hoc network, where a group of transmitting nodes are randomly distributed following a homogeneous Poisson point process (PPP) Φ with λ. The dipole model is adopted [81], where the distance for a typical transmitting node-receiver is fixed at r, and the typical receiver is assumed to be located at the origin. Both the transmitting node and its corresponding receiver use directional beamforming for data transmission, which is intercepted by multiple eavesdroppers. We consider the case of passive eavesdropping without any active attacks to deteriorate the information transmission. The locations of eavesdroppers are modeled following an independent homogeneous PPP Φ_e with λ_e. We use a sectored model to analyze the beam pattern [37, 82–84] (See Fig. 1 in [37]), i.e., the effective antenna gain for an interferer i seen by the typical receiver is expressed as

$$G_i = \begin{cases} G_{\mathrm{M}}^2, & \Pr_{\mathrm{MM}} = \left(\frac{\theta}{2\pi}\right)^2, \\ G_{\mathrm{M}} G_{\mathrm{m}}, & \Pr_{\mathrm{Mm}} = \frac{\theta(2\pi-\theta)}{(2\pi)^2}, \\ G_{\mathrm{m}} G_{\mathrm{M}}, & \Pr_{\mathrm{Mm}} = \frac{\theta(2\pi-\theta)}{(2\pi)^2}, \\ G_{\mathrm{m}}^2, & \Pr_{\mathrm{mm}} = \left(\frac{2\pi-\theta}{2\pi}\right)^2, \end{cases} \tag{4.1}$$

where G_{M} denotes the main-lobe gain with the beamwidth θ, G_{m} denotes the side-lobe gain, and $\Pr_{\ell k}$ ($\ell, k \in \{\mathrm{M}, \mathrm{m}\}$) denotes the probability that the antenna gain $G_\ell G_k$ occurs. We assume that the maximum array gain $G_{\mathrm{M}} G_{\mathrm{M}}$ is obtained for the typical transmitting node-receiver.

In light of the blockage effects in the outdoor scenario, the signal path can be LoS or NLoS. We denote $f_{\Pr}(R)$ as the probability that a link at a distance R

is LoS, while the NLoS probability of a link is $1 - f_{\Pr}(R)$. The LoS probability function $f_{\Pr}(R)$ can be obtained from field measurements or stochastic blockage models [83].

We employ a short-range propagation model in which given a distance $|X_i|$, the path loss function is denoted as $L(|X|) = \beta(\max(d, |X|))^{-\alpha}$ with a reference distance d [76], where β is the frequency independent constant parameter of the path loss, and α is the path loss exponent depending on the LoS or NLoS link, namely $\alpha = \alpha_{\text{LoS}}$ for LoS link and $\alpha = \alpha_{\text{NLoS}}$ for NLoS link. Note that the sparse scattering mmWave environment makes many traditional fading distributions invalid for the modeling of the mmWave channel [85]. For tractability, we neglect small scale fading as [86] argues that fading is not significant in LOS links with significant beamforming. Hence the signal-to-interference-plus-noise ratio (SINR) at a typical receiver is written as

$$\gamma_o = \frac{P_t G_{\text{M}}^2 L(r)}{\sum_{i \in \Phi/o} P_t G_i L(|X_i|) + \sigma_o^2}, \tag{4.2}$$

where P_t denotes the transmit power, $|X_i|$ is the distance between the typical receiver and the interferer $i \in \Phi/o$ (except the typical transmitting node), and σ_o^2 is the noise power.

When the eavesdropping channel is degraded under the effect of interference, secrecy indeed becomes better. In this chapter, we focus on the worst-case eavesdropping scenario, where all the eavesdroppers can mitigate the interference. In fact, eavesdroppers are usually assumed to have strong ability, and they may cooperate with each other to cancel the interference, as seen in [87]. In such a scenario, the most malicious eavesdropper that has the largest SINR of the received signal dominates the secrecy rate [88]. Thus, the SINR at the most malicious eavesdropper is written as

$$\gamma_{e^*} = \max_{e \in \Phi_e} \left\{ \frac{P_t G_e L(|X_e|)}{\sigma_e^2} \right\}, \tag{4.3}$$

where $|X_e|$ is the distance between the typical transmitting node and the eavesdrop-

per $e \in \Phi_e$, σ_e^2 is the power of noise and weak interference, and G_e is the antenna gain seen from the eavesdropper $e \in \Phi_e$ described by

$$G_e = \begin{cases} G_{\mathrm{M}} G_{\mathrm{M}}^e, & \Pr_{\mathrm{MM}} = \frac{\theta\phi}{(2\pi)^2}, \\ G_{\mathrm{M}} G_{\mathrm{m}}^e, & \Pr_{\mathrm{Mm}} = \frac{\theta(2\pi-\phi)}{(2\pi)^2}, \\ G_{\mathrm{m}} G_{\mathrm{M}}^e, & \Pr_{\mathrm{Mm}} = \frac{(2\pi-\theta)\phi}{(2\pi)^2}, \\ G_{\mathrm{m}} G_{\mathrm{m}}^e, & \Pr_{\mathrm{mm}} = \frac{(2\pi-\theta)(2\pi-\phi)}{(2\pi)^2}, \end{cases} \tag{4.4}$$

in which ϕ, G_{M}^e and G_{m}^e are the beamwidth of the main-lobe, main-lobe gain and side-lobe gain of the beam pattern used by the eavesdropper $e \in \Phi_e$, respectively.

4.4 Secrecy Evaluation

In this section, we analyze the average achievable secrecy rate in mmWave ad hoc networks. As shown in [89], physical layer security is commonly characterized by the secrecy rate R_{s}, which is defined as

$$R_{\mathrm{s}} = \left[\log_2(1+\gamma_o) - \log_2(1+\gamma_{e^*})\right]^+. \tag{4.5}$$

Based on (4.5), we have the following proposition.

Proposition 1. *In mmWave ad hoc networks, the average achievable secrecy rate is given by*

$$\overline{R}_{\mathrm{s}}^{\mathrm{L}} = \left[\overline{R} - \overline{R}_{e^*}\right]^+, \tag{4.6}$$

where $[x]^+ = \max\{x, 0\}$, $\overline{R} = \mathbb{E}\left[\log_2(1+\gamma_o)\right]$ *is the average rate of the channel between the typical transmitting node and its receiver, and* $\overline{R}_{e^*} = \mathbb{E}\left[\log_2(1+\gamma_{e^*})\right]$ *is the average rate of the channel between the typical transmitting node and the most malicious eavesdropper.*

Proof. We first show that the average rate $\overline{R}$ is achievable by considering the following two facts: 1) For low-mobility scenario, the received SINR γ_o is stationary during a certain period, since the small scale fading is negligible in mmWave net-

works. The transmission rate of a typical node can be set as $R_t = \log_2(1+\gamma_o)$ and thus the average rate $\overline{R}$ is achievable; and 2) for high-mobility scenario, the coherence time in mmWave frequencies is around an order of magnitude lower than that at sub-6 GHz as the Doppler shift linearly scales with frequency [90, 91], and coding over many coherence intervals is possible, thus, the average rate $\overline{R}$ can also be achievable.

On the other hand, the malicious eavesdroppers only intercept the secrecy massages passively without any transmissions, the channel state information (CSI) of the eavesdropping channels cannot be obtained by the transmitting node. Therefore, the transmission rate of a typical transmitting node is only dependent on the CSI of the channel between itself and the typical receiver. In addition, the maximum average rate in an arbitrary wiretap channel cannot exceed $\overline{R}_{e^*}$. As such, we obtain the average achievable secrecy rate in mmWave ad hoc networks as (4.6). □

To evaluate the average achievable secrecy rate, we first derive the average rate $\overline{R}$, which is given by the following theorem.

Theorem 4. *The exact average rate between the typical transmitting node and its intended receiver is given by*

$$\overline{R} = \frac{1}{\ln 2}\int_0^\infty \frac{1}{z}(1-\Xi_1(z))\Xi_2(z)e^{-z\sigma_o^2}dz, \tag{4.7}$$

where $\Xi_1(z)$ *and* $\Xi_2(z)$ *are respectively given by* (4.8) *and* (4.9) *at the top of next page.*

Proof. See Appendix A. □

The exact average rate given in (4.7) can be lower bounded as a simple expression, which is as follows.

Theorem 5. *The lower bound of the average rate* $\overline{R}$ *is given by*

$$\overline{R}_1^{\mathrm{L}} = \log_2\left(1+\frac{G_M^2\beta r^{-\overline{\alpha}}}{\lambda\bar{G}\Lambda+\frac{N_o}{P_t}}\right), \tag{4.10}$$

$$\Xi_1(z) = f_{\mathrm{Pr}}(r)\, e^{-zP_t G_{\mathrm{M}}^2 \beta (\max\{r,d\})^{-\alpha_{\mathrm{LoS}}}} + (1 - f_{\mathrm{Pr}}(r)) e^{-zP_t G_{\mathrm{M}}^2 \beta (\max\{r,d\})^{-\alpha_{\mathrm{NLoS}}}} \quad (4.8)$$

$$\Xi_2(z) = \exp\Big(-2\pi\lambda \int_0^{\infty} f_{\mathrm{Pr}}(u)\,(1 - \Omega_1(z,u)) u du - 2\pi\lambda \int_0^{\infty} (1 - f_{\mathrm{Pr}}(u))(1 - \Omega_2(z,u)) u du \Big) \quad (4.9)$$

with

$$\begin{cases} \Omega_1(z,u) = \sum\limits_{\ell,k\in\{\mathrm{M,m}\}} \mathrm{Pr}_{\ell k} \times e^{-zP_t G_\ell G_k \beta (\max\{u,d\})^{-\alpha_{\mathrm{LoS}}}} \\ \Omega_2(z,u) = \sum\limits_{\ell,k\in\{\mathrm{M,m}\}} \mathrm{Pr}_{\ell k} \times e^{-zP_t G_\ell G_k \beta (\max\{u,d\})^{-\alpha_{\mathrm{NLoS}}}} \end{cases}$$

---

where $\overline{\alpha} = (\alpha_{LoS} - \alpha_{NLoS}) f_{\mathrm{Pr}}(r) + \alpha_{NLoS}$, *the average antenna gain* $\bar{G} = \sum_{\ell,k\in\{M,m\}} G_\ell G_k Pr_{\ell k}$, *and* Λ *is*

$$\begin{aligned} \Lambda = \beta 2\pi \Big(& \int_0^d \big((d^{-\alpha_{LoS}} - d^{-\alpha_{NLoS}}) r f_{Pr}(r) + d^{-\alpha_{NLoS}} r \big) dr \\ & + \int_d^{\infty} \big((r^{1-\alpha_{LoS}} - r^{1-\alpha_{NLoS}}) f_{Pr}(r) + r^{1-\alpha_{NLoS}} \big) dr \Big). \end{aligned} \quad (4.11)$$

When the LoS probability is $f_{\mathrm{Pr}}(R) = e^{-\rho R}$ *[83],* (4.10) *reduces to a closed-form expression with*

$$\begin{aligned} \Lambda = {} & \beta 2\pi \times \\ & \Big[\frac{1 - e^{-d\rho}(1 + d\rho)}{\rho^2} \Big(\frac{1}{d^{\alpha_{LoS}}} - \frac{1}{d^{\alpha_{NLoS}}} \Big) + \frac{\Gamma(2 - \alpha_{LoS}, d\rho)}{\rho^{2-\alpha_{LoS}}} \\ & + \frac{\alpha_{NLoS} \cdot d^{2-\alpha_{NLoS}}}{2(\alpha_{NLoS} - 2)} - \frac{\Gamma(2 - \alpha_{NLoS}, d\rho)}{\rho^{2-\alpha_{NLoS}}} \Big]. \end{aligned} \quad (4.12)$$

Proof. See Appendix B. □

From **Theorem 2**, we find that as the transmit power grows large, the average rate is asymptotically lower bounded as $\overline{R}_1^{\mathrm{L}} \to \log_2\Big(1 + \frac{G_{\mathrm{M}}^2 \beta r^{-\overline{\alpha}}}{\lambda \bar{G} \Lambda}\Big)$. It is explicitly shown from (4.10) that the average rate between the typical transmitting node and its receiver is a decreasing function of transmitting node density, and increases with narrower beam due to the lower average interfering antenna gain. In addition, we

$$\mathscr{P}_1(x) = \exp\left\{-2\pi\lambda_e \int_0^\infty f_{\Pr}(r_e) r_e \sum_{\ell,n\in\{\mathrm{M,m}\}} \mathbf{1}\left(\max\{r_e,d\} < \left(\frac{P_t G_\ell G_n^e \beta}{x\sigma_e^2}\right)^{\frac{1}{\alpha_{\mathrm{LoS}}}}\right) \Pr_{\ell n} dr_e\right\} \tag{4.15}$$

$$\mathscr{P}_2(x) = \exp\left\{-2\pi\lambda_e \int_0^\infty (1-f_{\Pr}(r_e)) r_e \sum_{\ell,n\in\{\mathrm{M,m}\}} \mathbf{1}\left(\max\{r_e,d\} < \left(\frac{P_t G_\ell G_n^e \beta}{x\sigma_e^2}\right)^{\frac{1}{\alpha_{\mathrm{NLoS}}}}\right) \Pr_{\ell n} dr_e\right\} \tag{4.16}$$

have the following important corollary.

Corollary 9. *Given a required average rate $\overline{R}_{\mathrm{th}}$ between the typical transmitting node and its receiver, it is achievable when the transmitting node density in the mmWave ad hoc network satisfies*

$$\lambda \le \left(\frac{G_M^2 \beta r^{-\overline{\alpha}}}{2^{\overline{R}_{\mathrm{th}}} - 1} - \frac{N_o}{P_t}\right) \bar{G}^{-1} \Lambda^{-1}. \tag{4.13}$$

From (4.13)*, we see that narrower beams allow mmWave ad hoc networks to accommodate more transmitting nodes.*

We next derive the average rate between the typical transmitting node and the most malicious eavesdropper, which is given by the following theorem.

Theorem 6. *The exact average rate between the typical transmitting node and the most malicious eavesdropper is given by*

$$\overline{R}_{e^*} = \frac{1}{\ln 2} \int_0^\infty \frac{(1 - \mathscr{P}_1(x)\,\mathscr{P}_2(x))}{1+x} dx, \tag{4.14}$$

where $\mathscr{P}_1(x)$ and $\mathscr{P}_2(x)$ are given in (4.15) *and* (4.16) *with $\mathbf{1}(A)$ representing the indicator function that returns one if the condition A is satisfied.*

Proof. See Appendix C. □

Substituting (4.7) and (4.14) into (4.5), we can thus evaluate the average achievable secrecy rate in this network.

4.4.1 Simplified LoS MmWave Model

The aforementioned analysis is derived by considering an arbitrary LoS probability, which is general. In this subsection, we employ a simplified LoS mmwave model, as mentioned in [83, 92]. In this model, the mmWave link is LoS if the distance for a typical transmitting node-receiver is not larger than the maximum LoS distance $\mathrm{D}_{\mathrm{LoS}}$, and otherwise it is outage. When a LoS link between a typical transmitting node and its receiver is built (i.e., $r < \mathrm{D}_{\mathrm{LoS}}$), the exact average rate between the typical transmitting node and its intended receiver given in **Theorem 1** can be simplified as

$$\hat{R} = \frac{1}{\ln 2}\int_0^{\infty} \frac{1}{z}(1-e^{-zP_t G_{\mathrm{M}}^2 L(r)})\hat{\Xi}_2(z)e^{-z\sigma_o^2}dz, \tag{4.17}$$

where $\hat{\Xi}_2(z)$ is calculated as

$$\begin{aligned}\hat{\Xi}_2(z) = \exp\Bigg\{ &-2\pi\lambda\Bigg[\frac{\mathrm{D}_{\mathrm{LoS}}^2}{2} - \sum_{\ell,k\in\{\mathrm{M,m}\}} \mathrm{Pr}_{\ell k}\Big(\\ &\frac{d^2}{2}e^{-zP_t G_{\mathrm{M}}^2 \beta d^{-\alpha_{\mathrm{LoS}}}} + \alpha_{\mathrm{LoS}}^{-1}(zP_t G_\ell G_k \beta)^{2/\alpha_{\mathrm{LoS}}} \\ &\Big(\Gamma\Big(-\frac{2}{\alpha_{\mathrm{LoS}}}, zP_t G_\ell G_k \beta \mathrm{D}_{\mathrm{LoS}}^{-\alpha_{\mathrm{LoS}}}\Big) \\ &-\Gamma\Big(-\frac{2}{\alpha_{\mathrm{LoS}}}, zP_t G_\ell G_k \beta d^{-\alpha_{\mathrm{LoS}}}\Big)\Big)\Big)\Bigg]\Bigg\}. \end{aligned} \tag{4.18}$$

Here, $\Gamma(\cdot,\cdot)$ is the upper incomplete gamma function [80, (8.350)].

It is explicitly shown from (4.17) that $\hat{R}$ is a decreasing function of λ, since adding more transmitting nodes results in larger interference.

Likewise, the exact average rate between the typical transmitting node and the most malicious eavesdropper given in **Theorem 3** can be simplified as

$$\overline{R}_{e^*} = \frac{1}{\ln 2}\int_0^{\infty} \frac{1-\exp\left(-2\pi\lambda_e \hat{F}_e(x)\right)}{1+x}dx, \tag{4.19}$$

where the cumulative distribution function

$$\hat{F}_e(x) = \sum_{\ell,n\in\{\mathrm{M,m}\}} \left(\mathbf{1}\left(d < \eta\left(G_\ell, G_n^e, x\right)\right) \frac{d^2}{2} + \frac{\rho^2 - d^2}{2} \right) \mathrm{Pr}_{\ell n} \tag{4.20}$$

with $\eta\left(G_\ell, G_n^e, x\right) = \left(\frac{P_t G_\ell G_n^e \beta}{x\sigma_e^2}\right)^{\frac{1}{\alpha_{\mathrm{LoS}}}}$ and $\rho = \min\left(\mathrm{D_{LoS}}, \eta\left(G_\ell, G_n^e, x\right)\right)$.

It is explicitly shown from (4.19) that $\overline{R}_{e^*}$ is an increasing function of λ_e, which means that the exact average rate between the typical transmitting node and the most malicious eavesdropper increases with the number of eavesdroppers.

Substituting (4.17) and (4.19) into (4.6), we can obtain the average achievable secrecy rate.

4.4.2 Uniform Linear Array

We proceed to evaluate the secrecy performance when all the nodes in this networks are equipped with ULA. Assume that the number of antennas possessed by each eavesdropper and the transmitting node are denoted by N_e and N, respectively, and each receiver has the same number of antennas as its transmitting node.

For ULA configuration with q antennas, the elements are placed along the y-axis of the propagation plane with $\Delta\tau$ spacing. Hence, the array steering and response vectors for the transmitting node and its receiver are written as [93]

$$\mathbf{a}_t(\varphi, q) = \left[1,\ e^{-j\frac{2\pi}{\omega}\Delta\tau\sin(\varphi)},\ldots,\ e^{-j\frac{2\pi}{\omega}(q-1)\Delta\tau\sin(\varphi)}\right]^T \tag{4.21}$$

and

$$\mathbf{a}_r(\xi, q) = \left[1,\ e^{-j\frac{2\pi}{\omega}\Delta\tau\sin(\xi)},\ldots,\ e^{-j\frac{2\pi}{\omega}(q-1)\Delta\tau\sin(\xi)}\right]^T, \tag{4.22}$$

respectively, where ω is the wavelength, $\varphi \sim U(0, 2\pi)$ and $\xi \sim U(0, 2\pi)$ are the azimuth angle of departure (AoD) and angle of arrival (AoA), respectively, and $(\cdot)^T$ denotes transpose. The channel model is established as $\mathbf{H} = \sqrt{L(R)}\mathbf{A}\left(\xi_r, \varphi_t\right)$ with the ULA steering matrix $\mathbf{A}\left(\xi_r, \varphi_t\right) = \mathbf{a}_r(\xi_r, q)\mathbf{a}_t^H(\varphi_t, q)$, where $(\cdot)^H$ is the conjugate transpose.

$$\mathscr{P}_1^{\mathrm{ULA}}(x)=\exp\left\{-2\pi\lambda_e\int_0^{\infty}\int_0^{2\pi}\mathbf{1}\left(\max\{r_e,d\}<\left(\frac{P_tG_e(\varphi_{t_{e,o}})\beta}{x\sigma_e^2}\right)^{\frac{1}{\alpha_{\mathrm{LoS}}}}\right)\frac{f_{\mathrm{Pr}}(r_e)}{2\pi}r_e d\varphi_{t_{e,o}}dr_e\right\} \tag{4.26}$$

$$\mathscr{P}_2^{\mathrm{ULA}}(x)=\exp\left\{-2\pi\lambda_e\int_0^{\infty}\int_0^{2\pi}\mathbf{1}\left(\max\{r_e,d\}<\left(\frac{P_tG_e(\varphi_{t_{e,o}})\beta}{x\sigma_e^2}\right)^{\frac{1}{\alpha_{\mathrm{NLoS}}}}\right)\frac{1-f_{\mathrm{Pr}}(r_e)}{2\pi}r_e d\varphi_{t_{e,o}}dr_e\right\} \tag{4.27}$$

We consider that matched filter (MF) beamforming is adopted at all the nodes including eavesdroppers, the transmitting nodes and their receivers for maximizing the received signal power. Note that MF is the optimal beamforming for eavesdroppers, since interference is negligible at the eavesdroppers. Hence, the antenna gain for a typical transmitting node seen by its receiver is

$$G_o=\left|\frac{\mathbf{a}_r^H(\xi_{r_o},N)}{\sqrt{N}}\mathbf{A}(\xi_{r_o},\varphi_{t_o})\frac{\mathbf{a}_t(\varphi_{t_o},N)}{\sqrt{N}}\right|^2=N^2, \tag{4.19}$$

and the antenna gain for an interferer i seen by the typical receiver is

$$G_i=\left|\frac{\mathbf{a}_r^H(\xi_{r_o},N)}{\sqrt{N}}\mathbf{A}\left(\xi_{r_{i,o}},\varphi_{t_{i,o}}\right)\frac{\mathbf{a}_t(\varphi_{t_i},N)}{\sqrt{N}}\right|^2. \tag{4.20}$$

Based on (4.21) and (4.22), after some manipulations, we have

$$G_i=\frac{1}{N^2}\frac{\left[1-\cos(N\mathscr{K}_1(\xi_{r_{i,o}}))\right]\left[1-\cos(N\mathscr{K}_2(\varphi_{t_{i,o}},\varphi_{t_i}))\right]}{\left[1-\cos(\mathscr{K}_1(\xi_{r_{i,o}}))\right]\left[1-\cos(\mathscr{K}_2(\varphi_{t_{i,o}},\varphi_{t_i}))\right]}, \tag{4.21}$$

where $\mathscr{K}_1\left(\xi_{r_{i,o}}\right)=2\pi\frac{\Delta\tau}{\omega}(\sin(\xi_{r_o})-\sin(\xi_{r_{i,o}}))$, $\mathscr{K}_2\left(\varphi_{t_{i,o}},\varphi_{t_i}\right)=2\pi\frac{\Delta\tau}{\omega}(\sin(\varphi_{t_{i,o}})-\sin(\varphi_{t_i}))$.

Based on **Theorem 2**, the average rate between the typical transmitting node and its intended receiver is lower bounded as

$$\overline{R}_{\mathrm{ULA}}^{\mathrm{L}}=\log_2\left(1+\frac{N^2\beta r^{-\overline{\alpha}}}{\lambda\bar{G}\Lambda_{\mathrm{ULA}}+\frac{N_o}{P_t}}\right), \tag{4.22}$$

where Λ_{ULA} is given from (4.11) with the average antenna gain

$$\bar{G} = \mathbb{E}[G_i] = \frac{1}{N^2}\mathbb{E}\left[\frac{1-\cos(N\mathscr{K}_1(\xi_{r_{i,o}}))}{1-\cos(\mathscr{K}_1(\xi_{r_{i,o}}))}\right]\times \mathbb{E}\left[\frac{1-\cos(N\mathscr{K}_2(\varphi_{t_{i,o}},\varphi_{t_i}))}{1-\cos(\mathscr{K}_2(\varphi_{t_{i,o}},\varphi_{t_i}))}\right]. \tag{4.23}$$

Since the beam-direction of the typical node and each interferer is a uniform random variable on $[0,2\pi]$, we can further obtain

$$\bar{G} = \frac{1}{N^2}\int_0^{2\pi}\frac{1-\cos(N\mathscr{K}_1(\xi_{r_{i,o}}))}{1-\cos(\mathscr{K}_1(\xi_{r_{i,o}}))}\frac{1}{2\pi}d\xi_{r_{i,o}}\times \int_0^{2\pi}\int_0^{2\pi}\frac{1-\cos(N\mathscr{K}_2(\varphi_{t_{i,o}},\varphi_{t_i}))}{1-\cos(\mathscr{K}_2(\varphi_{t_{i,o}},\varphi_{t_i}))}\frac{1}{4\pi^2}d\varphi_{t_{i,o}}d\varphi_{t_i}. \tag{4.24}$$

Likewise, the antenna gain G_e seen from the eavesdropper $e \in \Phi_e$ is

$$\begin{aligned} G_e\left(\varphi_{t_{e,o}}\right) &= \left|\frac{\mathbf{a}_r^H(\xi_{r_{e,o}},N_e)}{\sqrt{N}}\mathbf{A}\left(\xi_{r_{e,o}},\varphi_{t_{e,o}}\right)\frac{\mathbf{a}_t(\varphi_{t_o},N)}{\sqrt{N}}\right|^2 \\ &= \left(\frac{N_e}{N}\right)^2\frac{1-\cos(N\mathscr{K}_3(\varphi_{t_{e,o}}))}{1-\cos(\mathscr{K}_3(\varphi_{t_{e,o}}))}, \end{aligned} \tag{4.25}$$

where $\mathscr{K}_3\left(\varphi_{t_{e,o}}\right) = 2\pi\frac{\Delta\tau}{\omega}(\sin(\varphi_{t_{e,o}})-\sin(\varphi_{t_o}))$. From (4.25), we find that increasing the number of antennas at the transmitting node decreases the antenna gain obtained by the eavesdroppers, which is helpful for degrading the signal strength at the eavesdroppers. Based on **Theorem 3**, the exact average rate $\overline{R}_{e^*}^{\mathrm{ULA}}$ between the typical transmitting node and the most malicious eavesdropper is given from (4.14) by interchanging $\mathscr{P}_1(x) \to \mathscr{P}_1^{\mathrm{ULA}}(x)$ and $\mathscr{P}_2(x) \to \mathscr{P}_2^{\mathrm{ULA}}(x)$, where $\mathscr{P}_1^{\mathrm{ULA}}(x)$ and $\mathscr{P}_2^{\mathrm{ULA}}(x)$ are given by (4.26) and (4.27), respectively. Thus, by using ULA, the average achievable secrecy rate can at least reach

$$\overline{R}_{s,\mathrm{ULA}}^{L} = \left[\overline{R}_{\mathrm{ULA}}^{\mathrm{L}} - \overline{R}_{e^*}^{\mathrm{ULA}}\right]^+. \tag{4.28}$$

4.5 Artificial Noise Aided Transmission

In this section, we evaluate the secrecy performance for the artificial noise aided transmission [39]. For this case, the total power per transmission is $P_t = P_S + P_A$, where the power allocated to the information signal is $P_S = \mu P_t$, and the power allocated to the artificial noise is $P_A = (1-\mu)P_t$. Here, μ is the fraction of power assigned to the information signal. The effective antenna gain G_i^S for the information signal of an interfering i seen by the typical receiver is expressed as

$$G_i^S = \begin{cases} G_{\mathrm{M}}^S G_{\mathrm{M}}, & \Pr_{\mathrm{MM}}^S = \frac{\vartheta\theta}{(2\pi)^2}, \\ G_{\mathrm{M}}^S G_{\mathrm{m}}, & \Pr_{\mathrm{Mm}}^S = \frac{\vartheta(2\pi-\theta)}{(2\pi)^2}, \\ G_{\mathrm{m}}^S G_{\mathrm{M}}, & \Pr_{\mathrm{mM}}^S = \frac{(2\pi-\vartheta)\theta}{(2\pi)^2}, \\ G_{\mathrm{m}}^S G_{\mathrm{m}}, & \Pr_{\mathrm{mm}}^S = \frac{(2\pi-\vartheta)(2\pi-\theta)}{(2\pi)^2}, \end{cases} \tag{4.29}$$

where ϑ, G_{M}^S and G_{m}^S are the beamwidth of the main-lobe, main-lobe gain and side-lobe gain for the information signal of an interfering i, respectively. Likewise, the effective antenna gain for the artificial noise of an interfering i seen by the typical receiver is expressed as

$$G_i^A = \begin{cases} G_{\mathrm{M}}^A G_{\mathrm{M}}, & \Pr_{\mathrm{MM}}^A = \frac{\varsigma\theta}{(2\pi)^2}, \\ G_{\mathrm{M}}^A G_{\mathrm{m}}, & \Pr_{\mathrm{Mm}}^A = \frac{\varsigma(2\pi-\theta)}{(2\pi)^2}, \\ G_{\mathrm{m}}^A G_{\mathrm{M}}, & \Pr_{\mathrm{mM}}^A = \frac{(2\pi-\varsigma)\theta}{(2\pi)^2}, \\ G_{\mathrm{m}}^A G_{\mathrm{m}}, & \Pr_{\mathrm{mm}}^A = \frac{(2\pi-\varsigma)(2\pi-\theta)}{(2\pi)^2}, \end{cases} \tag{4.30}$$

where ς, G_{M}^A and G_{m}^A are the beamwidth of the main-lobe, main-lobe gain and side-lobe gain for the artificial noise of an interfering i, respectively. The effective antenna gain G_e^S and G_e^A for the information signal and artificial noise of the typical transmitting node seen by the eavesdropper $e \in \Phi_e$ can be respectively given from (4.29) and (4.30) by interchanging the parameters $G_{\mathrm{M}} \to G_{\mathrm{M}}^e$, $G_{\mathrm{m}} \to G_{\mathrm{m}}^e$ and $\theta \to \phi$.

Considering that the artificial noise sent by the typical transmitting node has negligible effect on the typical receiver [39], the SINR at the typical receiver is

given by

$$\widetilde{\gamma}_o = \frac{P_S G_{\mathrm{M}}^S G_{\mathrm{M}} L(r)}{\sum_{i\in\Phi/o}\left(P_S G_i^S + P_A G_i^A\right) L(|X_i|) + \sigma_o^2}. \tag{4.31}$$

The SINR at the most malicious eavesdropper is given by

$$\widetilde{\gamma}_{e^*} = \max_{e\in\Phi_e}\left\{\frac{P_S G_e^S L(|X_e|)}{P_A G_e^A L(|X_e|) + \sigma_e^2}\right\}. \tag{4.32}$$

Following (4.6), the average achievable secrecy rate for the artificial noise aided transmission is lower bounded as

$$\widetilde{R}_S^{\mathrm{L}} = \left[\widetilde{R} - \widetilde{R}_e^*\right]^+, \tag{4.33}$$

where $\widetilde{R} = \mathbb{E}\left[\log_2(1+\widetilde{\gamma}_o)\right]$ and $\widetilde{R}_e^* = \mathbb{E}\left[\log_2(1+\widetilde{\gamma}_{e^*})\right]$, $\widetilde{R}$ and $\widetilde{R}_e^*$ are given by the following theorems.

Theorem 7. *The exact average rate for the artificial noise aided transmission between the typical transmitting node and its intended receiver is given by*

$$\widetilde{R} = \frac{1}{\ln 2}\int_0^\infty \frac{1}{z}(1-\widetilde{\Xi}_1(z))\widetilde{\Xi}_2(z)e^{-z\sigma_0^2}dz, \tag{4.34}$$

where $\widetilde{\Xi}_1(z)$ *and* $\widetilde{\Xi}_2(z)$ *are respectively given by* (4.35) *and* (4.36) *at the top of next page. In* (4.36), $\mathrm{Pr}_{\mathrm{M}} = \frac{\theta}{2\pi}$ *and* $\mathrm{Pr}_{\mathrm{m}} = 1 - \mathrm{Pr}_{\mathrm{M}}$.

Proof. It can be proved by following a similar approach shown in the **Theorem** 1. □

Using the similar approach shown in the Appendix B, the exact average rate given in (4.34) can be lower bounded as a simple expression, which is given by the following theorem.

Theorem 8. *The lower bound of the average rate* $\widetilde{R}$ *is*

$$\widetilde{R}_1^{\mathrm{L}} = \log_2\left(1 + \frac{G_M^S G_M \beta r^{-\overline{\alpha}}}{\lambda\widetilde{\Lambda} + \frac{N_o}{\mu P_t}}\right), \tag{4.37}$$

$$\widetilde{\Xi}_1(z) = f_{\Pr}(r)\, e^{-zP_S G_{\mathrm{M}}^S G_{\mathrm{M}} \beta (\max\{r,d\})^{-\alpha_{\mathrm{LoS}}}} + (1 - f_{\Pr}(r)) e^{-zP_S G_{\mathrm{M}}^S G_{\mathrm{M}} \beta (\max\{r,d\})^{-\alpha_{\mathrm{NLoS}}}} \tag{4.35}$$

$$\widetilde{\Xi}_2(z) = \exp\Big(-2\pi\lambda \int_0^{\infty} f_{\Pr}(u)\,(1 - \widetilde{\Omega}_1(z,u)) u du - 2\pi\lambda \int_0^{\infty} (1 - f_{\Pr}(u))(1 - \widetilde{\Omega}_2(z,u)) u du \Big) \tag{4.36}$$

with

$$\begin{cases} \widetilde{\Omega}_1(z,u) = \sum_{\ell,\nu,k\in\{\mathrm{M,m}\}} \dfrac{\Pr_{\ell k}^S \Pr_{\nu k}^A}{\Pr_k} \times e^{-z(P_S G_\ell^S G_k + P_A G_\nu^A G_k)\beta (\max\{u,d\})^{-\alpha_{\mathrm{LoS}}}} \\ \widetilde{\Omega}_2(z,u) = \sum_{\ell,\nu,k\in\{\mathrm{M,m}\}} \dfrac{\Pr_{\ell k}^S \Pr_{\nu k}^A}{\Pr_k} \times e^{-z(P_S G_\ell^S G_k + P_A G_\nu^A G_k)\beta (\max\{u,d\})^{-\alpha_{\mathrm{NLoS}}}} \end{cases}$$

$$\widetilde{\mathscr{P}}_1(x) = \exp\Big\{ -2\pi\lambda_e \int_0^{\infty} f_{\Pr}(r_e) r_e \sum_{\ell,\nu,n\in\{\mathrm{M,m}\}} \frac{\Pr_{\ell n}^S \Pr_{\nu n}^A}{\Pr_n^e} \mathbf{1}\Big(\max\{r_e, d\} < \big(\frac{P_S G_\ell^S G_n^e \beta - P_A G_\nu^A G_n^e \beta x}{x\sigma_e^2} \tag{4.41}$$

$$\widetilde{\mathscr{P}}_2(x) = \exp\Big\{ -2\pi\lambda_e \int_0^{\infty} (1 - f_{\Pr}(r_e)) r_e \sum_{\ell,\nu,n\in\{\mathrm{M,m}\}} \frac{\Pr_{\ell n}^S \Pr_{\nu n}^A}{\Pr_n^e} \mathbf{1}\Big(\max\{r_e, d\} < \big(\frac{P_S G_\ell^S G_n^e \beta - P_A G_\nu^A G_n^e \beta x}{x\sigma_e^2} \tag{4.42}$$

---

where $\widetilde{\Lambda}$ *is*

$$\begin{aligned} \widetilde{\Lambda} &= \Big(\bar{G}_S + \frac{1-\mu}{\mu} \bar{G}_A \Big) \beta 2\pi \\ &\times \Big(\int_0^d (d^{-\alpha_{LoS}} - d^{-\alpha_{NLoS}}) r f_{Pr}(r) + d^{-\alpha_{NLoS}} r dr \\ &\quad + \int_d^{\infty} (r^{1-\alpha_{LoS}} - r^{1-\alpha_{NLoS}}) f_{Pr}(r) + r^{1-\alpha_{NLoS}} dr \Big). \end{aligned} \tag{4.38}$$

with

$$\bar{G}_S = \sum_{\ell,k\in\{M,m\}} G_\ell^S G_k Pr_{\ell k}^S, \bar{G}_A = \sum_{\nu,k\in\{M,m\}} G_\nu^A G_k Pr_{\nu k}^A.$$

Based on **Theorem** 5, we have the following important corollary.

Corollary 10. *The required average rate $\widetilde{R}_{\rm th}$ between the typical transmitting node and its receiver can be achieved when the transmitting node density satisfies*

$$\lambda \leq \left(\frac{G_M^S G_M \beta r^{-\overline{\alpha}}}{2^{\widetilde{R}_{\rm th}} - 1} - \frac{N_o}{\mu P_t} \right) \widetilde{\Lambda}^{-1}. \tag{4.39}$$

We next present the average rate between the typical transmitting node and the most malicious eavesdropper as follows.

Theorem 9. *The exact average rate for the artificial noise aided transmission between the typical transmitting node and the most malicious eavesdropper is given by*

$$\widetilde{R}_e^* = \frac{1}{\ln 2} \int_0^\infty \frac{\left(1 - \widetilde{\mathscr{P}}_1(x)\, \widetilde{\mathscr{P}}_2(x)\right)}{1+x} dx, \tag{4.40}$$

where $\widetilde{\mathscr{P}}_1(x)$ and $\widetilde{\mathscr{P}}_2(x)$ are respectively given by (4.41) *and* (4.42)*. In* (4.41) *and* (4.42)*, $\Pr_{\rm M}^e = \frac{\phi}{2\pi}$ and $\Pr_{\rm m}^e = 1 - \Pr_{\rm M}^e$.*

Proof. It can be proved by following a similar approach shown in the **Theorem** 2. □

Substituting (4.34) and (4.40) into (4.33), we obtain the average achievable secrecy rate for the artificial noise aided transmission.

4.6 Numerical Results

Numerical results are presented to understand the impact of mmWave channel characteristics and large antenna array on the achievable secrecy rate. We assume that the LoS probability function is $f_{\rm Pr}(R) = e^{-\rho R}$ with $1/\rho = 141.4$ m [83]. The mmWave bandwidth is BW = 2 GHz, the noise figure is Nf = 10 dB, the noise power is $\sigma_o^2 = \sigma_e^2 = -174 + 10\log 10({\rm BW}) + {\rm Nf}$ dBm, and the reference distance is $d = 1$.

We focus on the carrier frequency at 28 GHz, 38 GHz, 60 GHz, and 73GHz, in which their LoS and NLoS path loss exponents are shown in Table 4.1 based on the practical channel measurements [1, 2].

Table 4.1: Path loss exponent for mm-wave outdoor channels [1, 2].

Path loss exponent	28GHz	38 GHz	60 GHz	73 GHz
LOS	2	2	2.25	2
Strongest NLOS	3	3.71	3.76	3.4

Table 4.2: Antenna Pattern [3].

Number of antenna elements	N
Beamwidth θ	$\frac{2\pi}{\sqrt{N}}$
Main-lobe gain	N
Side-lobe gain	$\frac{1}{\sin^2(3\pi/2\sqrt{N})}$

4.6.1 Average Achievable Secrecy Rate

In this subsection, we consider the uniform planar array (UPA) with the antenna pattern shown in Table 4.2. The transmitting nodes and their receivers are equipped with N antennas each, and each eavesdropper is equipped with N_e antennas.

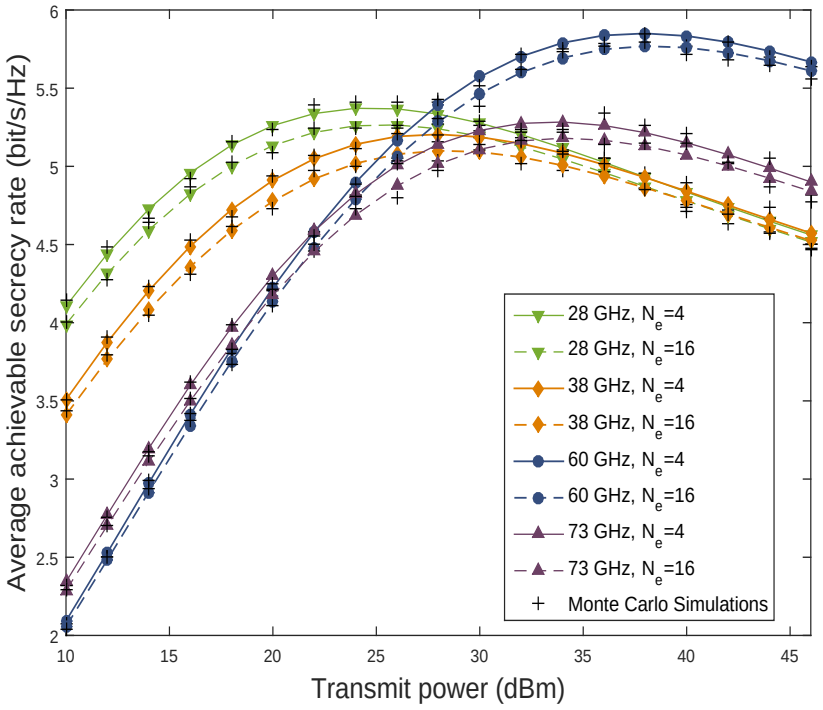

Figure 4.1: Effects of transmit power on the average achievable secrecy rate at 28 GHz, 38 GHz, 60 GHz and 73 GHz: $\lambda = 50/\text{km}^2$, $\lambda_e = 100/\text{km}^2$, $N = 16$, and $r = 15$ m.

Fig. 1 shows the effects of transmit power on the average achievable secrecy rate. The analytical curves are obtained from (4.6), which are validated by the Monte Carlo simulations marked by '+'. We observe that there exist optimal transmit power values for maximizing average achievable secrecy rate at all the commonly-considered mmWave frequencies. In the low transmit power regime, better secrecy performance is achieved at 28 GHz, and higher average achievable secrecy rate can be obtained in the higher mmWave frequency band (60 GHz and 73 GHz) as the transmit power becomes large. The reason is that in the low transmit power regime, mmWave ad hoc network tends to be noise-limited and less propagation loss at lower mmWave frequencies results in better performance, however, in the high transmit power regime, the transmitting node receives less interference at higher mmWave frequencies and achieves higher average achievable secrecy rate. Meanwhile, eavesdroppers will not obtain much information when adding transmit power at higher mmWave frequencies, compared to the lower mmWave frequencies. In addition, it is shown that the performance at 60GHz is better than that at 73 GHz when the transmit power is large enough, due to the fact that the atmospheric absorption at 60 GHz is more severe than that at 73 GHz, which leads to higher LoS pathloss exponent at 60 GHz.

Additionally, using the antenna pattern in Table 4.2, average achievable secrecy rate is a bit lower at $N_e = 16$ than that at $N_e = 4$, due to fact that more effective antenna gain obtained by eavesdroppers using UPA with $N_e = 16$, which deteriorates the secrecy performance.

Fig. 2 shows the effects of transmitting node density on the average achievable secrecy rate at 60 GHz. We see that when increasing the transmitting node density, the average achievable secrecy rate declines. The reason is that when the transmitting nodes are dense, mmWave ad hoc networks becomes interference-limited, and the interference caused by other transmitting nodes dominate the performance. It is confirmed that in the large-scale mmWave ad hoc networks, more eavesdroppers have a detrimental effect on the secrecy.

Fig. 3 shows the effects of different typical distances on the average rate at

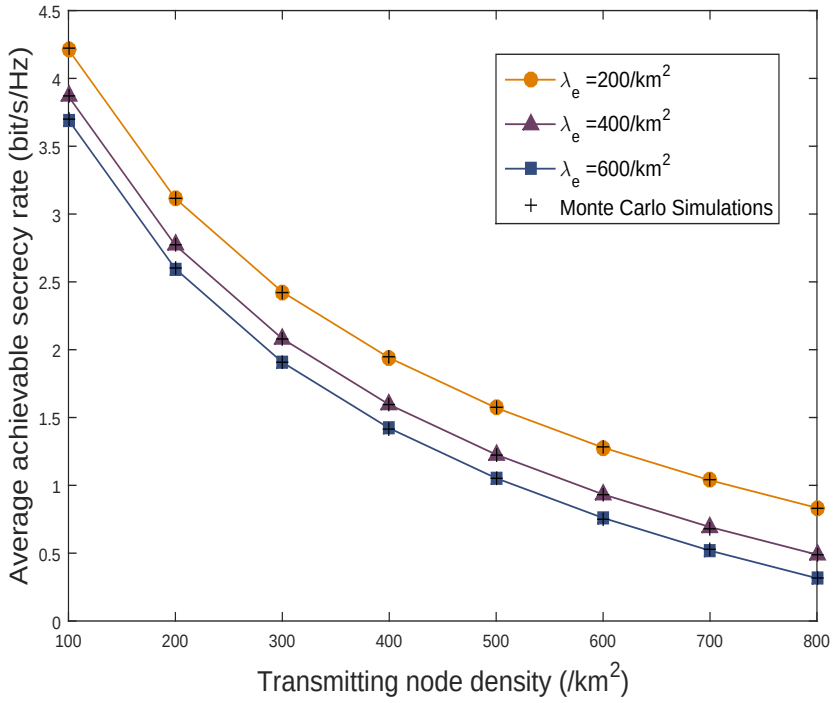

Figure 4.2: Effects of transmitting node density on the average achievable secrecy rate at 60 GHz: $N = 16$, $N_e = 16$, $r = 15$ m, and $P_t = 30$ dBm.

60 GHz. The green solid and dashed curves with triangles obtained from (4.7) and (4.10) represent the exact and lower-bound average rate between the typical transmitting node and its intended receiver, respectively, and the orange solid curve with circles obtained from (4.14) represents the average rate in the most malicious eavesdropping channel. We observe that the lower bound curves can efficiently predict the performance behavior. It is shown that when the communication distance grows large, there is a significant decrease in the average achievable secrecy rate, due to the fact that the average rate between the typical transmitting node and its receiver decreases while the average rate in the most malicious eavesdropper's channel is unaltered. This illustrates that the secrecy rate in mmWave ad hoc networks is highly dependent on the communication distance between the transmitting node and its receiver.

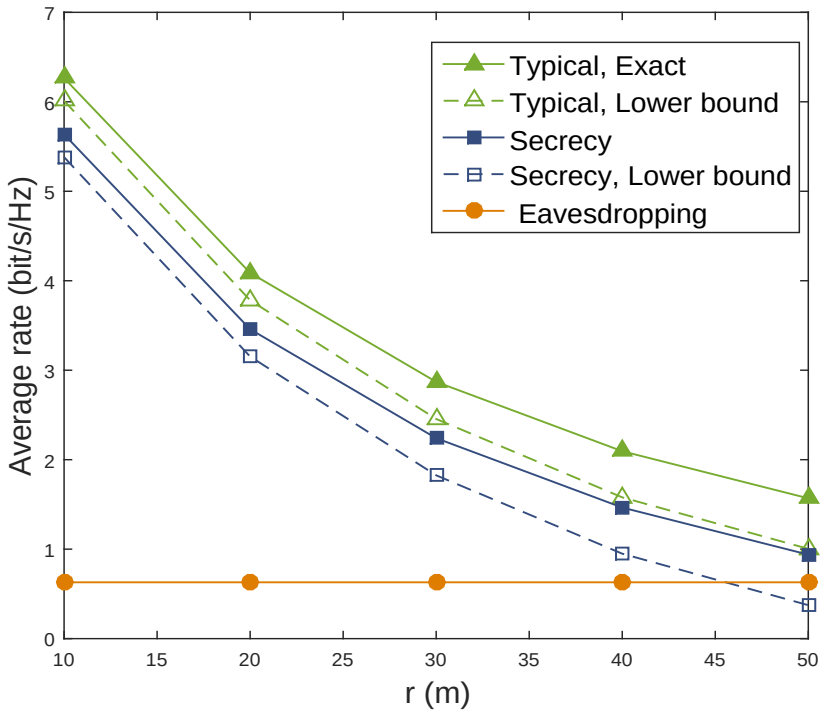

Figure 4.3: Effects of transmit power with different typical distances on the average rate at 28 GHz: $P_t = 10$ dBm, $\lambda = 10/\text{km}^2$, $\lambda_e = 100/\text{km}^2$, $N = 16$, and $N_e = 16$.

4.6.2 average achievable secrecy rate with ULA

In this subsection, we consider the ULA configuration, and choose the antenna spacing as $\triangle\tau = \frac{1}{2}\omega$. The results in Figs. 4 and 5 are obtained from (4.28).

Fig. 4 shows the average achievable secrecy rate with different number of antennas at the transmitting nodes and eavesdroppers. It is observed that the average achievable secrecy rate increases with the number of antennas at the transmitting nodes, and decreases when eavesdroppers are equipped with more antennas. Moreover, the average achievable secrecy rate becomes very small when the transmitting node only has a couple of antennas. The reason is that the information signal beam is not narrow and more eavesdroppers can receive strong signals when they have more receive antennas.

Fig. 5 shows the achievable average achievable secrecy rate for different node densities. We see that more eavesdroppers located in the networks are indeed harmful for secrecy. However, when the density of transmitting nodes increases, the

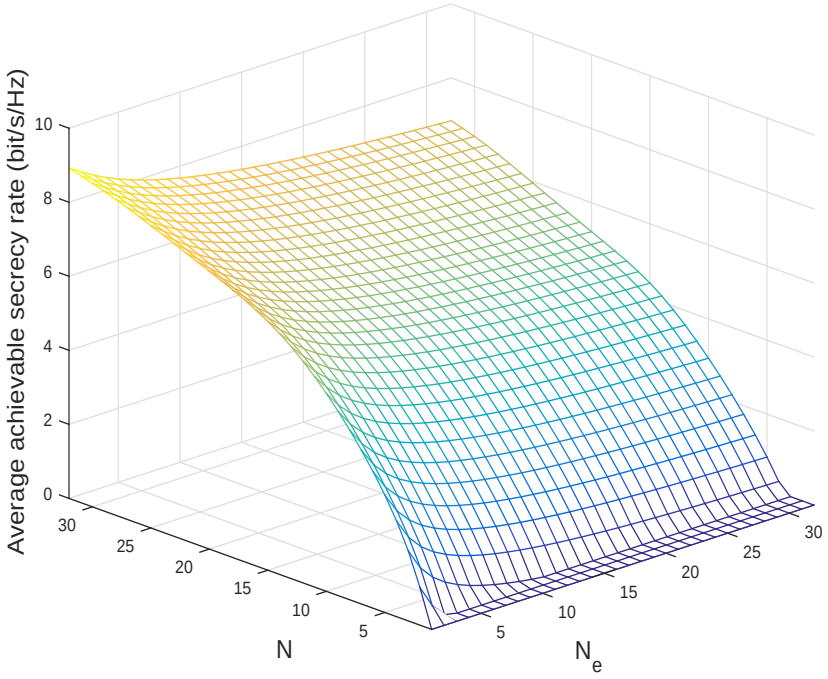

Figure 4.4: Effects of different antenna numbers on the average achievable secrecy rate at 38 GHz: $\lambda = 50/\text{km}^2$, $\lambda_e = 100/\text{km}^2$, $r = 20$ m, $P_t = 10$ dBm, $\xi_{r_o} = \pi/3$, $\varphi_{t_o} = \pi/3$.

secrecy performance also degrades, which indicates that interference can still be a concern for super dense transmitting nodes without highly directional antennas.

4.6.3 average achievable secrecy rate with Artificial Noise

In this subsection, we examine the effects of artificial noise (AN) on the secrecy performance.

Fig. 6 shows the effects of transmit power with/without AN at 60 GHz. We consider that the antenna beam patterns of sending information signal and AN at the transmitting node are $(G^S_{\text{M}}, G^S_{\text{m}}, \vartheta) = (3 \text{ dB}, -3 \text{ dB}, 45^o)$ and $(G^A_{\text{M}}, G^A_{\text{m}}, \varsigma) = (3 \text{ dB}, -3 \text{ dB}, 45^o)$, respectively, and the antenna beam pattern of only sending information signal without AN at the transmitting node is $(G_{\text{M}}, G_{\text{m}}, \theta) = (10 \text{ dB}, -10 \text{ dB}, 15^o)$, as seen in [37]. The analytical curves without/with AN are obtained from (4.6) and (4.33), respectively. We see that when the transmitting nodes are not dense ($\lambda = 20/\text{km}^2$ in this figure), the average achievable secrecy

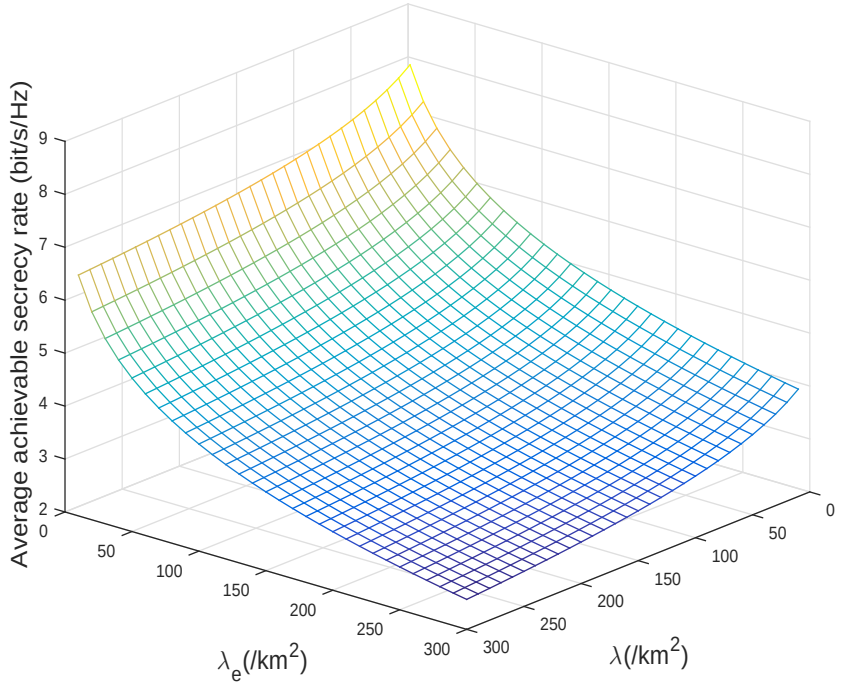

Figure 4.5: Effects of different node densities on the average achievable secrecy rate at 38 GHz: $N = 16$, $N_e = 4$, $r = 20$ m, $P_t = 10$ dBm, $\xi_{r_o} = \pi/3$, $\varphi_{t_o} = \pi/3$.

rate increases with the transmit power. In this case, the use of AN is unable to improve secrecy, and more power should be allocated to the information signal. Moreover, it is indicated that eavesdroppers using wide beam pattern can intercept more information.

Fig. 7 shows the effects of transmit power with/without AN in different frequency bands, i.e., 28 GHz and 38 GHz. The lower-bound results with/without AN are obtained by using (4.37) and (4.10) to calculate the average rate between the transmitting node and its receiver, respectively. We see that the lower bound results can well approximate the exact ones when the transmit power is not large ($<$ 30 dBm in this figure). The average achievable secrecy rate at 28 GHz is larger than that at 38 GHz, which indicates that the use of lower frequency bands could achieve better secrecy performance. The average achievable secrecy rate increases with transmit power, and the use of AN cannot improve the secrecy. The reason is that in this circumstance, more power should be used to enhance the transmission

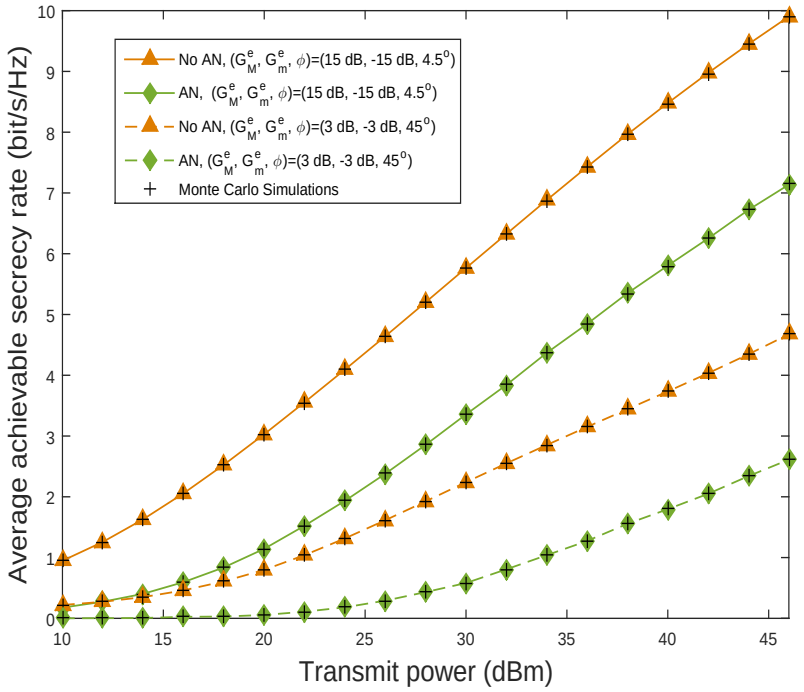

Figure 4.6: Effects of transmit power with/without AN on the average achievable secrecy rate at 60 GHz: $\lambda = 20/\text{km}^2$, $\lambda_e = 300/\text{km}^2$, $r = 50$ m, and $\mu = 0.85$.

rate between the transmitting node and its receiver.

Fig. 8 shows the effects of transmit power allocation factor on the average achievable secrecy rate. We see that there exists an optimal μ to maximize the average achievable secrecy rate, which reveals that AN can help enhance secrecy when the power allocation between the information signal and AN is properly set. Again, we see that larger communication distance r deteriorates the secrecy performance. In addition, for a given r, secrecy transmission at 28GHz is better than that at 38 GHz.

4.7 Conclusion

We concentrated on the secure communication in mmWave ad hoc networks by using physical layer security. We derived the average achievable secrecy rate without/with artificial noise. A tractable approach was developed to evaluate the average achievable secrecy rate when nodes are equipped with ULA. The results have highlighted the impacts of different mmWave frequencies, transmit power, node density

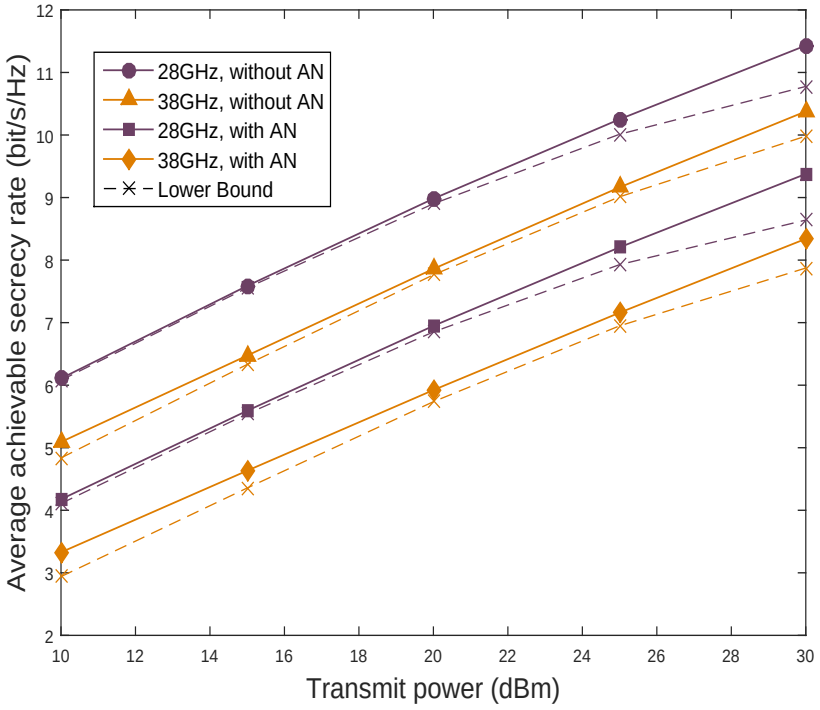

Figure 4.7: Effects of transmit power with AN on the average achievable secrecy rate at 28 and 38 GHz: $\lambda = 30/\text{km}^2$, $\lambda_e = 500/\text{km}^2$, $r = 20$ m, $\mu = 0.85$, $(G_{\text{M}}, G_{\text{m}}, \theta) = (15\text{ dB}, -15\text{ dB}, 4.5^\circ)$, $(G^S_{\text{M}}, G^S_{\text{m}}, \theta) = (10\text{ dB}, -10\text{ dB}, 15^\circ)$, $(G^A_{\text{M}}, G^A_{\text{m}}, \theta) = (3\text{ dB}, -3\text{ dB}, 45^\circ)$, $(G^e_{\text{M}}, G^e_{\text{m}}, \phi) = (3\text{ dB}, -3\text{ dB}, 45^\circ)$.

and antenna gains on the secrecy performance. Important insights have been provided into the interplay between transmit power and mmWave frequency. When the node density is dense, the interference from nearby nodes dominates the secrecy performance. It is shown that power allocation between the information signal and AN needs to be carefully determined for secrecy performance enhancement.

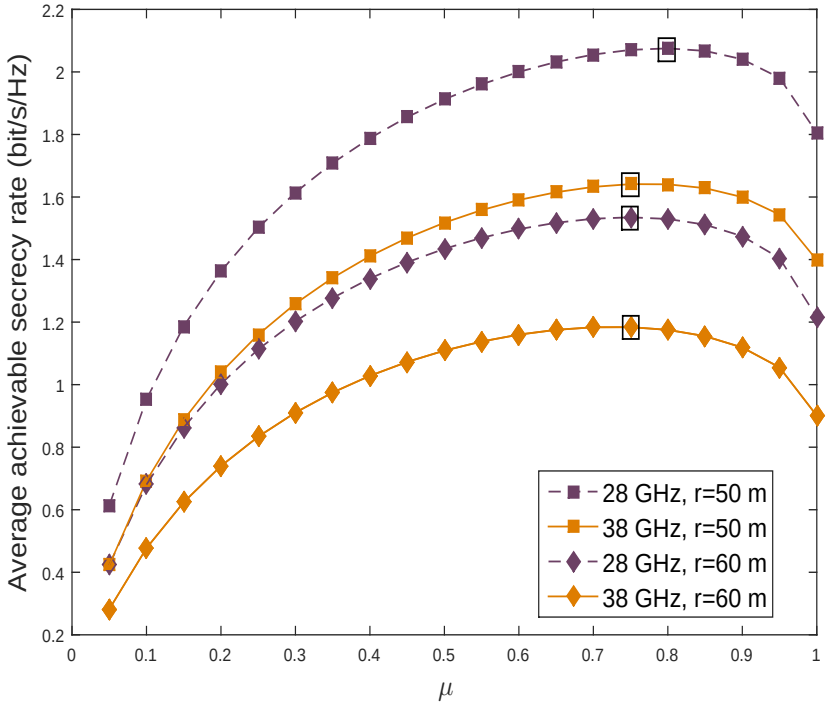

Figure 4.8: Effects of transmit power allocation factor on the average achievable secrecy rate at 28 and 38 GHz: $\lambda = 50/\text{km}^2$, $\lambda_e = 500/\text{km}^2$, $P_t = 30$ dBm, $(G_{\text{M}}, G_{\text{m}}, \theta) = (10\text{ dB}, -10\text{ dB}, 15^\circ)$, $(G^S_{\text{M}}, G^S_{\text{m}}, \vartheta) = (3\text{ dB}, -3\text{ dB}, 45^\circ)$, $(G^A_{\text{M}}, G^A_{\text{m}}, \varsigma) = (3\text{ dB}, -3\text{ dB}, 45^\circ)$.

Chapter 5

Conclusions and Future Work

5.1 Conclusions

In this chapter, the main contributions of this thesis are summarized, and some future research directions are also presented.

The aim of this thesis was to solve three specific challenges concerning energy-efficiency in 5G networks. A large part of the work concerns the two WPT issues, one being the optimization of power control for two-user interference channels and the other being the analysis of the potential implementation of wireless power transfer in HetNets. The rest concerns the introduction of secure communications in mmWave links to enhance the energy-efficiency of ad hoc networks.

Different aspects of system enhancement design are considered in each chapter.

The first contribution, presented in Chapter 2, studied the optimization problem for the power allocation for a 2-user interference channel for time-switching SWIPT. With both the rate and energy harvesting constraints, the sum-rate has been maximized by investigating the geometric properties of the constraints assuming perfect CSI.

The second contribution, presented in Chapter 3, considered WPT in the massive MIMO enabled HetNets. A stochastic geometry approach was adopted to model the K-tier HetNets where massive MIMO antennas were employed in the macrocells. The effect of massive MIMO antennas on user association was investigated, and two specific user association schemes were analyzed. The downlink

energy harvesting and uplink information transmission were evaluated in terms of average harvested energy and average achievable rate, respectively.

Finally, in Chapter 4, we focused on secure communication in mmWave ad hoc networks using physical layer security. The average achievable secrecy rate with/without artificial noise was derived. A tractable approach was developed to evaluate the average achievable secrecy rate when nodes are equipped with ULA. The results have highlighted the impacts of different mmWave frequencies, transmit power, node density and antenna gains on secrecy performance. Important insights have been provided into the interplay between transmit power and mmWave frequency.

In summary, this thesis provides a well-rounded set of contributions addressing the problem of enhancing building overall resource effectiveness in 5G wireless communication systems. These results provide new insights into the observation and analysis the effectiveness of networks using WPT, HetNets, Massive MIMO and mmwave technology. All the contributions in this thesis greatly advance the state of the art in the next generation wireless communication.

5.2 Possible Extensions

In this section, the potential extensions of the current three topics are investigated in the following.

5.2.1 Possible Extension 1: Geometric Programming Power Control for 3-pair Cells

5G systems usually contain a large number of links, while the two user link channel is only one special case. Groups of links transmitting the EH and ID can improve the sum rate is usually considered.

In paper [94], the author has considered allocating the transmit powers for a wireless multi-link system with $N > 2$, in order to maximize the total system throughput under interference and noise impairments and short term power constraints.

The solution for optimal the sum rate under multi-link is hard to find, but we

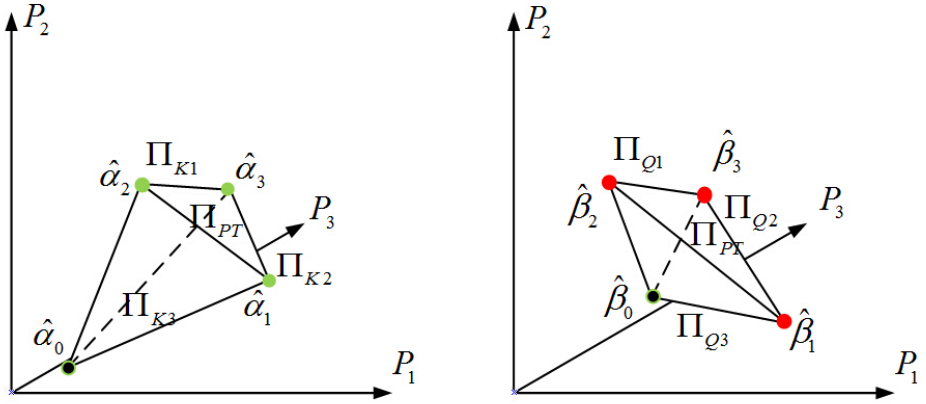

Figure 5.1: Illustration of the possible feasible regions. Optimal solution set under 3-cell model in ID scheme (right) and EH scheme (left), following the picture, each picture conclude three rate plane (express as $\prod_{K1}$,$\prod_{K2}$and $\prod_{K3}$) and EH constraints plane (express as $\prod_{Q1}$,$\prod_{Q2}$and $\prod_{Q3}$) and one sum power constraint plane, in the rate scheme red point is optimal solution of the EH, and in EH scheme green point is optimal solution of the rate received.

could propose a approximate approach with geometric power control or multi-point power control, this approach can reduce the complexity of exhaustively searching for obtain the best sum-rate point for large networks.

In this topic, we will consider the problem that how three transmitter/receiver pairs could share the power in IR and EH time slot, respectively.

We formulate the optimization problem under sum power limited in each slot like:

$$\begin{aligned} \underset{P_1,P_2,P_3}{max} \quad & R_{sum} = \sum_i R_i, Y_{sum} = \sum_i Y_i \ \forall i, i = 1,2,3 \\ \text{subject to} \quad & \sum_{i=1} P_i^{ID} \leqslant P_{Total}^{ID} \\ & \sum_{i=1} P_i^{EH} \leqslant P_{Total}^{EH} \\ & R_i \leqslant \underline{R}_i \ \forall i, i = 1,2 \\ & Y_i \leqslant \underline{Y}_i \ \forall i, i = 1,2 \end{aligned} \tag{5.1}$$

In Fig. 5.1, $\prod_{K1}$,$\prod_{K2}$ and $\prod_{K3}$ are express the constrains plane of minimum rate requirement $\underline{R}_i$. $\prod_{Q1}$,$\prod_{Q2}$ and $\prod_{Q3}$ are express the constrains plane of minimum energy harvesting requirement $\underline{Y}_i$. $\widehat{\alpha} = [\hat{\alpha}_0, \hat{\alpha}_1, \hat{\alpha}_2, \hat{\alpha}_3]$ and $\widehat{\beta} = [\hat{\beta}_0, \hat{\beta}_1, \hat{\beta}_2, \hat{\beta}_3]$

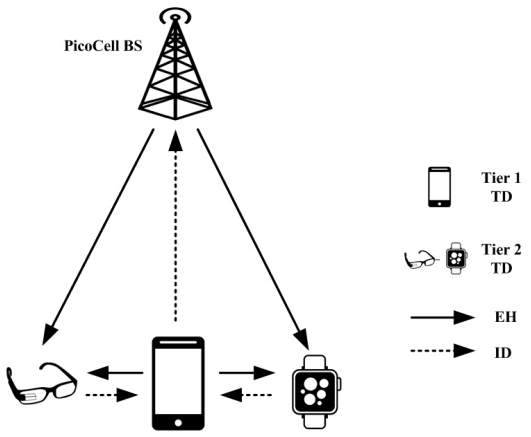

Figure 5.2: The system model show new type of HetNet, Tier 1 user help Tier 2 user upload the information, the dash arrows means uplink information transfer; the solid arrows means downlink energy harvesting.

are point of intersection with planes.

5.2.2 Possible Extension 2: Multi-hopping for Two-tier Heterogeneous-User in Wearable Devices Networks

Wearable communications networks are a new type of networks in wireless communications. Wearable terminals are revolutionizing people's life, especially low-power devices such as smart watch and smart glasses, often positioned as accessories to modern phones.

With the availability of newer commercial products, paper [95] claim many people will have between 3 and 10 wearable devices in the near future, including wearable fitness trackers, helmet mounted cameras and accessories.

A main challenge for wearable networks is supporting the huge amount of devices in dense environments. These wearable terminal devices can not always directly communication with MBS, which needs to be controlled by higher priority terminal devices.

This work will consider a 2-tier terminal devices in SBSs and relays networks. Tier 1 terminal device help tier 2 terminal devices upload the information, and all the users also need harvest the energy from its serving BS (we assume that only picocell BS server the 2-tier TD), and use the harvested energy to transmit data. The

entire communication consists of two different phases, namely, energy harvesting and information transmission phase.

Each one duration of a communications block is T. The first phase of duration is τT, where $\tau \in (0,1)$ is the time allocation factor, and tier 2 terminal devices harvest energy from tier 1 terminal devices and SBS. The remaining time of duration $(1-\tau)T$ is equally partitioned into two parts, during the first half period, the tier 2 terminal device transmits information to the tier 1 terminal device, and during the second half, the tier 1 terminal device forwards the information to SBS.

In this work, we will analyze the average available rate and average harvested energy in two-tier heterogeneous users, respectively.

Appendix A

Appendix A:Proof of Lemma 1

In this appendix, we will list the possible cases for making out the feasible region for the power allocation when both the rate and energy harvesting constraints are considered. We will also describe how we refer to particular cases by numbering the edges of $\boldsymbol{l}_{Y_1}$ and $\boldsymbol{l}_{Y_2}$. Note that throughout we will assume that the slope of $\boldsymbol{l}_{Y_2}$ is greater than that of $\boldsymbol{l}_{Y_1}$ for conciseness. All the results will apply naturally by swapping the indices corresponding to lines $\boldsymbol{l}_{Y_1}$ and $\boldsymbol{l}_{Y_2}$, if it is not.

Figs. 2.5(a)–(d) illustrate all 4 possible cases of the feasible region made out by the energy harvesting constraints when $\boldsymbol{P}_{\mathrm{Y}}^{i,\times}$ is inside Π^*, which we refer to them, respectively, as scenario $(i)(a)$ to $(i)(d)$, while Figs. 2.5(e)–(h) provide, for each of the cases, an example how lines $\boldsymbol{l}_{R_1}$ and $\boldsymbol{l}_{R_2}$ may cut on the edges of the region to form the resultant feasible region. To distinguish the various cases, we number the edges of the region made out by lines $\boldsymbol{l}_{Y_1}$ and $\boldsymbol{l}_{Y_2}$. For example, in Fig. 2.5(d), $\boldsymbol{l}_{R_1}$ cuts edge 1 and $\boldsymbol{l}_{R_2}$ cuts edge 3. Hence, it is referred to as the $(1,3)$ case in scenario $(i)(a)$. Other examples and cases can be understood in the same way. As a result, we can also see that Figs. 2.5(a)–(d) represent 25 cases in total.

Moreover, Figs. 2.6 and 2.7 provide the illustrations for scenario (ii) when $\boldsymbol{P}_{\mathrm{Y}}^{i,\times}$ is outside and on the right of Π^* and (iii) if $\boldsymbol{P}_{\mathrm{Y}}^{i,\times}$ is at the top or left side of Π^*. We can see that scenario (ii) create a total of 9 cases while scenario (iii) could make out 4 possible feasible regions. Scenarios (i)–(iii) altogether thus give a total of $38 \times 2 = 76$ possible cases, after we take into account of the fact that lines $\boldsymbol{l}_{Y_1}$ and $\boldsymbol{l}_{Y_2}$ can swap.

Appendix B

Appendix B: A proof of Lemma 2

Using DRSP-based user association in Section II-A, we first examine the power gain by using the proposed downlink power transfer design. As will be indicated by (C.1) in Appendix B, the downlink received power gain is $G_a^{\mathrm{D}} = (N+S-1)$, which is different from the conventional massive MIMO networks without energy harvesting, due to the fact that the interference is identified as an RF energy source.

Using the similar approach suggested by [96, Appendix A], we can then obtain the desired results (3.19) and (3.20).

Appendix C: A proof of Theorem 1 Based on (3.8), given $\left|X_{o,\mathrm{M}}\right| = x$, the average harvested energy for a typical user served by the MBS is written as

$$\begin{aligned}
&\widetilde{\mathrm{E}}_{o,\mathrm{M}}^{\mathrm{DRSP}}(x) \\
&= \mathbb{E}\left\{\mathrm{E}_{o,\mathrm{M}}^{1}\right\} + \mathbb{E}\left\{\mathrm{E}_{o,\mathrm{M}}^{2}\right\} + \mathbb{E}\left\{\mathrm{E}_{o,\mathrm{M}}^{3}\right\} \\
&= \eta P_{\mathrm{M}}\left(\mathbb{E}\{h_o\} + \mathbb{E}\{h_o'\}(S-1)\right)\frac{\tau T}{S} L\left(\max\{x,d\}\right) \\
&\quad + \mathbb{E}\left\{\mathrm{E}_{o,\mathrm{M}}^{3}\right\} \\
&= \eta (N+S-1)\frac{P_{\mathrm{M}}}{S}\beta \\
&\quad \times \left(\mathbf{1}(x \le d)\, d^{-\alpha_{\mathrm{M}}} + \mathbf{1}(x > d)\, x^{-\alpha_{\mathrm{M}}}\right)\tau T \\
&\quad + \mathbb{E}\left\{\mathrm{E}_{o,\mathrm{M}}^{3}\right\}, \qquad \text{(C.1)}
\end{aligned}$$

where $\mathbb{E}\left\{\mathrm{E}_{o,\mathrm{M}}^{3}\right\}$ denotes the average harvested energy from the ambient RF, and is

expressed as

$$\mathbb{E}\left\{\mathrm{E}_{o,\mathrm{M}}^{3}\right\}=\eta\left(\mathbb{E}\{I_{\mathrm{M},1}\}+\mathbb{E}\{I_{\mathrm{S},1}\}\right)\times\tau T. \tag{C.2}$$

Here, $\mathbb{E}\{I_{\mathrm{M},1}\}$ is the average power harvested from the intra-tier interference, which is given by

$$\begin{aligned}
&\mathbb{E}\{I_{\mathrm{M},1}\}\\
&=\mathbb{E}\left\{\sum_{\ell\in\Phi_{\mathrm{M}}\setminus\{o\}}P_{\mathrm{M}}h_{\ell}L\left(\max\left\{\left|X_{\ell,\mathrm{M}}\right|,d\right\}\right)\right\}\\
&=P_{\mathrm{M}}\mathbb{E}\left\{\sum_{\ell\in\Phi_{\mathrm{M}}\setminus\{o\}}\mathbb{E}\{h_{\ell}\}L\left(\max\left\{\left|X_{\ell,\mathrm{M}}\right|,d\right\}\right)\right\}\\
&\overset{(a)}{=}P_{\mathrm{M}}\beta 2\pi\lambda_{\mathrm{M}}\left(\int_{x}^{\infty}\left(\max\{r,d\}\right)^{-\alpha_{\mathrm{M}}}rdr\right)\\
&=P_{\mathrm{M}}\beta 2\pi\lambda_{\mathrm{M}}\left(\mathbf{1}\left(x\leq d\right)\left(d^{-\alpha_{\mathrm{M}}}\frac{(d^{2}-x^{2})}{2}-\frac{d^{2-\alpha_{\mathrm{M}}}}{2-\alpha_{\mathrm{M}}}\right)\right.\\
&\qquad\left.-\mathbf{1}\left(x>d\right)\frac{x^{2-\alpha_{\mathrm{M}}}}{2-\alpha_{\mathrm{M}}}\right),
\end{aligned} \tag{C.3}$$

where (a) results from $\mathbb{E}\{h_{\ell}\}=1$ and the Campbell's theorem [81]. [1] Similarly, $\mathbb{E}\{I_{\mathrm{S},1}\}$ is the average power harvested from the inter-tier interference, which is

[1] The Campbell's theorem is [81]: For a Poisson point process Φ with density λ, we have $\mathbb{E}\left\{\sum_{x_i\in\Phi}f(x_i)\right\}=\lambda\int_{\mathbb{R}^{\dim}}\mathbb{E}\{f(x)\}dx$.

given by

$$\begin{aligned}
&\mathbb{E}\{I_{\mathrm{S},1}\} \\
&= \mathbb{E}\left\{\sum_{i=2}^{K}\sum_{j\in\Phi_i} P_i h_j L\left(\max\left\{\left|X_{j,i}\right|, d\right\}\right)\right\} \\
&= \sum_{i=2}^{K} P_i \beta 2\pi\lambda_i \left(\int_{\hat{r}_{\mathrm{MS}} x^{\alpha_{\mathrm{M}}/\alpha_i}}^{\infty} \left(\max\{r,d\}\right)^{-\alpha_i} r dr\right) \\
&= \sum_{i=2}^{K} P_i \beta 2\pi\lambda_i \Bigg[\mathbf{1}(x \le d_o) \\
&\qquad\qquad \times \left(d^{-\alpha_i}\frac{\left(d^2 - \hat{r}_{\mathrm{MS}}^2 x^{\frac{2\alpha_{\mathrm{M}}}{\alpha_i}}\right)}{2} - \frac{d^{2-\alpha_i}}{2-\alpha_i}\right) \\
&\qquad\qquad -\mathbf{1}(x > d_o)\frac{\hat{r}_{\mathrm{MS}}^{(2-\alpha_i)} x^{\frac{\alpha_{\mathrm{M}}(2-\alpha_i)}{\alpha_i}}}{2-\alpha_i}\Bigg],
\end{aligned} \tag{C.4}$$

in which $d_o = \left(\hat{r}_{\mathrm{MS}}\right)^{-\frac{\alpha_i}{\alpha_{\mathrm{M}}}} d^{\alpha_i/\alpha_{\mathrm{M}}}$. By substituting (C.3) and (C.4) into (C.1), we then obtain (3.30).

We next derive the average harvested energy for a typical user served by the SBS in the k-th tier under a given distance $\left|X_{o,k}\right| = y$, which is given by

$$\begin{aligned}
&\widetilde{\mathrm{E}}_{o,k}^{\mathrm{DRSP}}(y) \\
&= \mathbb{E}\left\{\mathrm{E}_{o,k}^{1}\right\} + \mathbb{E}\left\{\mathrm{E}_{o,k}^{2}\right\} \\
&= \eta P_k L(\max\{y,d\}) \times \tau T + \eta\left(\mathbb{E}\left\{I_{\mathrm{M},k}\right\} + \mathbb{E}\left\{I_{\mathrm{S},k}\right\}\right) \times \tau T,
\end{aligned} \tag{C.5}$$

where $\mathbb{E}\left\{I_{\mathrm{M},k}\right\}$ is calculated as

$$\begin{aligned}
&\mathbb{E}\left\{I_{\mathrm{M},k}\right\} \\
&= \mathbb{E}\left\{\sum_{\ell\in\Phi_{\mathrm{M}}} P_{\mathrm{M}} g_\ell L\left(\max\left\{\left|X_{\ell,\mathrm{M}}\right|, d\right\}\right)\right\} \\
&= P_{\mathrm{M}}\beta 2\pi\lambda_{\mathrm{M}}\left(\int_{\hat{r}_{\mathrm{SM}} y^{\alpha_k/\alpha_{\mathrm{M}}}}^{\infty}\left(\max\{r,d\}\right)^{-\alpha_{\mathrm{M}}} r dr\right) \\
&= P_{\mathrm{M}}\beta 2\pi\lambda_{\mathrm{M}}\Bigg[\mathbf{1}\left(y\le d_1\right) \\
&\qquad\qquad \times\left(d^{-\alpha_{\mathrm{M}}}\frac{\left(d^2-\hat{r}_{\mathrm{SM}}^2 y^{\frac{2\alpha_k}{\alpha_{\mathrm{M}}}}\right)}{2}-\frac{d^{2-\alpha_{\mathrm{M}}}}{2-\alpha_{\mathrm{M}}}\right) \\
&\qquad\qquad -\mathbf{1}\left(y>d_1\right)\frac{\hat{r}_{\mathrm{SM}}^{2-\alpha_{\mathrm{M}}} y^{\frac{\alpha_k(2-\alpha_{\mathrm{M}})}{\alpha_{\mathrm{M}}}}}{2-\alpha_{\mathrm{M}}}\Bigg],
\end{aligned} \tag{C.6}$$

where $d_1 = \left(\hat{r}_{\mathrm{SM}}\right)^{\frac{-\alpha_{\mathrm{M}}}{\alpha_k}} d^{\alpha_{\mathrm{M}}/\alpha_k}$, and $\mathbb{E}\left\{I_{\mathrm{S},k}\right\}$ is given by

$$\begin{aligned}
&\mathbb{E}\left\{I_{\mathrm{S},k}\right\} \\
&= \mathbb{E}\left\{\sum_{i=2}^{K}\sum_{j\in\Phi_i\setminus\{o\}} P_i g_{j,i} L\left(\max\left\{\left|X_{j,i}\right|, d\right\}\right)\right\} \\
&= \sum_{i=2}^{K}\beta 2\pi\lambda_i\int_{\hat{r}_{\mathrm{SS}} y^{\frac{\alpha_k}{\alpha_i}}}^{\infty}\left(\max\{r,d\}\right)^{-\alpha_i} r dr \\
&= \sum_{i=2}^{K}\beta 2\pi\lambda_i\Bigg[\mathbf{1}\left(y\le d_2\right) \\
&\qquad\qquad \times\left(d^{-\alpha_i}\frac{\left(d^2-\hat{r}_{\mathrm{SS}}^2 y^{\frac{2\alpha_k}{\alpha_i}}\right)}{2}-\frac{d^{2-\alpha_i}}{2-\alpha_i}\right) \\
&\qquad\qquad -\mathbf{1}\left(y>d_2\right)\frac{\hat{r}_{\mathrm{SS}}^{2-\alpha_i} y^{\frac{\alpha_k(2-\alpha_i)}{\alpha_i}}}{2-\alpha_i}\Bigg],
\end{aligned} \tag{C.7}$$

where $d_2 = \left(\hat{r}_{\mathrm{SS}}\right)^{\frac{-\alpha_i}{\alpha_k}} d^{\alpha_i/\alpha_k}$. By plugging (C.6) and (C.7) into (C.5), we obtain the

desired result in (3.31).

Appendix C

Appendix D: A proof of Corollary 3

According to (3.30) and (3.33), we first are required to derive the following asymptotic expressions:

$$\Xi_1(x) = \int_0^x f^{\mathrm{DRSP}}_{|X_{o,\mathrm{M}}|}(r)dr, \tag{D.1a}$$

$$\Xi_2(a,b) = \int_a^\infty x^b f^{\mathrm{DRSP}}_{|X_{o,\mathrm{M}}|}(x)dx, \tag{D.1b}$$

$$\Xi_3(c,d) = \int_0^c x^d f^{\mathrm{DRSP}}_{|X_{o,\mathrm{M}}|}(x)dx. \tag{D.1c}$$

By using the Taylor series expansion truncated to the first order as $N \to \infty$, (C.1a) is asymptotically computed as

$$\Xi_1(x) = \frac{2\pi\lambda_{\mathrm{M}}}{\Psi^{\mathrm{DRSP}}_{\mathrm{M}_\infty}} \left[\int_0^x r \exp\left(-\pi\lambda_{\mathrm{M}} r^2\right) dr \right.$$
$$\left. -\pi \sum_{i=2}^{K} \lambda_i \hat{r}^2_{\mathrm{MS}} \int_0^x r^{1+\frac{2\alpha_{\mathrm{M}}}{\alpha_i}} \exp\left(-\pi\lambda_{\mathrm{M}} r^2\right) dr \right]. \tag{D.2}$$

It is noted that the asymptotic expression for the probability of a typical user that is associated with the MBS has been derived in (3.24). Therefore, we can directly apply the result in (D.2). After some mathematical manipulations, we obtain (3.35). Similarly, the asymptotic expressions for (C.1b) and (C.1c) are correspondingly derived as (3.36) and (3.37). Substituting (3.35)–(3.37) into (3.33), we obtain the desired result in (3.32).

Appendix D

Appendix E: A proof of Theorem 2

The exact average achievable rate is written as

$$R = \frac{(1-\tau)T}{T}\mathbb{E}\left\{\log_2\left(1+\mathrm{SINR}\right)\right\}. \tag{E.1}$$

Now, using Jensen's inequality, we can obtain the lower bound for the conditional average uplink achievable rate between a typical user and its serving MBS as

$$R^{\mathrm{low}}_{\mathrm{DRSP,M}}(x) = (1-\tau)\log_2\left(1+\frac{1}{\mathrm{E}\left\{\mathrm{SINR}_{\mathrm{M}}^{-1}\right\}}\right). \tag{E.2}$$

Based on (3.14), $\mathbb{E}\left\{\mathrm{SINR}_{\mathrm{M}}^{-1}\right\}$ is calculated as

$$\begin{aligned}
&\mathbb{E}\left\{\mathrm{SINR}_{\mathrm{M}}^{-1}\right\} \\
&= \mathbb{E}\left\{\frac{I_{u,\mathrm{M}}+I_{u,\mathrm{S}}+\delta^2}{P_{u_{\mathrm{M}}}^{\mathrm{DRSP}}h_{o,\mathrm{M}}L\left(\max\left\{x,d\right\}\right)}\right\} \\
&\overset{(a)}{\approx} \left(P_{u_{\mathrm{M}}}^{\mathrm{DRSP}}(N-S+1)L\left(\max\left\{x,d\right\}\right)\right)^{-1} \\
&\qquad \times\left(\mathbb{E}\left\{I_{u,\mathrm{M}}\right\}+\mathbb{E}\left\{I_{u,\mathrm{S}}\right\}+\delta^2\right),
\end{aligned} \tag{E.3}$$

where (a) is obtained by using the law of large numbers, i.e., $h_{o,\mathrm{M}} \approx N - S + 1$ as N becomes large. Using the Campbell's theorem [81], we next derive $\mathbb{E}\left\{I_{u,\mathrm{M}}\right\}$ as

$$\begin{aligned}
&\mathbb{E}\left\{I_{u,\mathrm{M}}\right\} \\
&= \mathbb{E}\left\{ \sum_{i \in \widetilde{\mathscr{U}_{\mathrm{M}}} \setminus \{o\}} P_{u_{\mathrm{M}}}^{\mathrm{DRSP}} h_i L\left(\max\left\{|X_i|, d\right\}\right) \right\} \\
&= P_{u_{\mathrm{M}}}^{\mathrm{DRSP}} \beta 2\pi (S\lambda_{\mathrm{M}}) \left(\int_0^d d^{-\alpha_{\mathrm{M}}} r dr + \int_d^{\infty} r^{-\alpha_{\mathrm{M}}} r dr \right) \\
&= P_{u_{\mathrm{M}}}^{\mathrm{DRSP}} \beta 2\pi (S\lambda_{\mathrm{M}}) \left(\frac{d^{2-\alpha_{\mathrm{M}}}}{2} + \frac{d^{2-\alpha_{\mathrm{M}}}}{\alpha_{\mathrm{M}} - 2} \right).
\end{aligned} \tag{E.4}$$

Likewise, $\mathbb{E}\left\{I_{u,\mathrm{S}}\right\}$ is derived as

$$\begin{aligned}
&\mathbb{E}\left\{I_{u,\mathrm{S}}\right\} \\
&= \mathbb{E}\left\{ \sum_{i=2}^{K} \sum_{j \in \widetilde{\mathscr{U}_i}} P_{u_i}^{\mathrm{DRSP}} h_j L\left(\max\left\{\left|X_j\right|, d\right\}\right) \right\} \\
&= \sum_{i=2}^{K} P_{u_i}^{\mathrm{DRSP}} \beta 2\pi \lambda_i \left(\frac{d^{2-\alpha_{\mathrm{M}}}}{2} + \frac{d^{2-\alpha_{\mathrm{M}}}}{\alpha_{\mathrm{M}} - 2} \right).
\end{aligned} \tag{E.5}$$

Substituting (E.3)–(E.5) into (E.2), we obtain (3.42).

Appendix E

Appendix F: A proof of Theorem 3

Given a distance $\left|X_{o,k}\right| = y$, the conditional average uplink achievable rate for a typical user served by the SBS in the k-th tier is expressed as

$$\begin{aligned} R_{\mathrm{DRSP},k}(y) &= \frac{(1-\tau)T}{T}\mathbb{E}\{\mathrm{SINR}_k\} \\ &= \frac{(1-\tau)}{\ln 2}\int_0^{\infty}\frac{\bar{F}_{\mathrm{SINR}}(x)}{1+x}dx, \end{aligned} \tag{F.1}$$

where $\bar{F}_{\mathrm{SINR}_k}(x)$ is the CCDF of the received SINR, denoted by SINR_k, and is given by

$$\begin{aligned} &\bar{F}_{\mathrm{SINR}}(x) \\ &= \Pr(\mathrm{SINR}_k > x) \\ &= \Pr\left(\frac{P_{u_k}^{\mathrm{DRSP}} g_{o,k} L(y,d)}{I_{u,\mathrm{M}} + I_{u,\mathrm{S}} + \delta^2} > x\right) \\ &= e^{-\frac{x\delta^2}{P_{u_k}^{\mathrm{DRSP}}\Delta_2(y)}}\mathbb{E}\left\{e^{-\frac{xI_{u,\mathrm{M}}}{P_{u_k}^{\mathrm{DRSP}}\Delta_2(y)}}\right\}\mathbb{E}\left\{e^{-\frac{xI_{u,\mathrm{S}}}{P_{u_k}^{\mathrm{DRSP}}\Delta_2(y)}}\right\} \\ &= e^{-\frac{x\delta^2}{P_{u_k}^{\mathrm{DRSP}}\Delta_2(y)}} \times \\ &\qquad \mathscr{L}_{I_{u,\mathrm{M}}}\left(\frac{x}{P_{u_k}^{\mathrm{DRSP}}\Delta_2(y)}\right)\mathscr{L}_{I_{u,\mathrm{S}}}\left(\frac{x}{P_{u_k}^{\mathrm{DRSP}}\Delta_2(y)}\right), \end{aligned} \tag{F.2}$$

where $\Delta_2(y) = L(\max\{y,d\})$, $\mathscr{L}_{I_{u,\mathrm{M}}}(\cdot)$ and $\mathscr{L}_{I_{u,\mathrm{S}}}(\cdot)$ are the Laplace transforms of the PDFs of $I_{u,\mathrm{M}}$ and $I_{u,\mathrm{S}}$, respectively. We first derive the Laplace transform of the

PDF of $I_{u,\mathrm{M}}$:

$$
\begin{aligned}
&\mathscr{L}_{I_{u,\mathrm{M}}}(s) \\
&= \mathbb{E}\left\{\exp\left(-s\sum_{i\in\widetilde{\mathscr{U}_{\mathrm{M}}}} P_{u_{\mathrm{M}}}^{\mathrm{DRSP}} g_i L(\max\{|X_i|,d\})\right)\right\} \\
&\overset{(a)}{=} \exp\left(-2\pi(S\lambda_{\mathrm{M}})\int_0^{\infty} \frac{sP_{u_{\mathrm{M}}}^{\mathrm{DRSP}} L(\max\{r,d\})}{1+sP_{u_{\mathrm{M}}}^{\mathrm{DRSP}} L(\max\{r,d\})} r dr\right) \\
&= \exp\left(-\pi(S\lambda_{\mathrm{M}})\frac{sP_{u_{\mathrm{M}}}^{\mathrm{DRSP}}\beta d^{-\alpha_i}}{1+sP_{u_{\mathrm{M}}}^{\mathrm{DRSP}}\beta d^{-\alpha_i}} d^2\right. \\
&\quad -2\pi(S\lambda_{\mathrm{M}}) sP_{u_{\mathrm{M}}}^{\mathrm{DRSP}}\beta \times \\
&\quad \left.\frac{d^{2-\alpha_i}}{\alpha_i-2}\,{}_2F_1\left[1,\frac{\alpha_i-2}{\alpha_i};2-\frac{2}{\alpha_i};-sP_{u_{\mathrm{M}}}^{\mathrm{DRSP}}\beta d^{-\alpha_i}\right]\right),
\end{aligned}
\tag{F.3}
$$

where (a) is obtained by using the generating functional of PPP [97]. Similarly, $\mathscr{L}_{I_{u,\mathrm{S}}}(s)$ is given by

$$
\begin{aligned}
\mathscr{L}_{I_{u,\mathrm{S}}}(s) = \exp\left(-\sum_{i=2}^{K}\pi\lambda_i \frac{sP_{u_i}^{\mathrm{DRSP}}\beta d^{-\alpha_i}}{1+sP_{u_i}^{\mathrm{DRSP}}\beta d^{-\alpha_i}} d^2\right. \\
-\sum_{i=2}^{K} 2\pi\lambda_i sP_{u_i}^{\mathrm{DRSP}}\beta\frac{d^{2-\alpha_i}}{\alpha_i-2}\times \\
\left.{}_2F_1\left[1,\frac{\alpha_i-2}{\alpha_i};2-\frac{2}{\alpha_i};-sP_{u_i}^{\mathrm{DRSP}}\beta d^{-\alpha_i}\right]\right).
\end{aligned}
\tag{F.4}
$$

Substituting (F.3) and (F.4) into (F.2), we get (3.47).

Appendix F

Appendix G: A detailed derivation of Theorem 4

Using [98, Lemma 1], the average rate $\overline{R}$ is calculated as

$$\begin{aligned}\overline{R} =& \mathbb{E}\left[\log_2(1+\gamma_0)\right] = \mathbb{E}\left[\frac{1}{\ln 2}\int_0^\infty \frac{1}{z}(1-e^{-z\gamma_o})e^{-z}dz\right] \\ =& \frac{1}{\ln 2}\mathbb{E}\left[\int_0^\infty \frac{1}{z}(1-e^{-zY})e^{-z(\mathscr{I}+\sigma_0^2)}dz\right] \\ =& \frac{1}{\ln 2}\int_0^\infty \frac{1}{z}(1-\underbrace{\mathbb{E}\left[e^{-zY}\right]}_{\Xi_1(z)})\underbrace{\mathbb{E}\left[e^{-z\mathscr{I}}\right]}_{\Xi_2(z)}e^{-z\sigma_0^2}dz, \end{aligned} \tag{G.1}$$

where $Y = P_t G_{\mathrm{M}}^2 L(r)$ is dependent on the LoS or NLoS condition given a distance r, and the interference $\mathscr{I}$ is

$$\mathscr{I} = \sum_{i\in\Phi/o} P_t G_i L(|X_i|). \tag{G.2}$$

Based on the law of total expectation, we can directly obtain $\Xi_1(z)$ as (4.8). Then, we see that $\Xi_2(z)$ is the Laplace transform of $\mathscr{I}$. To solve it, using the thinning theorem [99], the mmWave transmitting nodes are divided into two independent PPPs, namely LoS point process Φ_{LoS} with density function $\lambda f_{\mathrm{Pr}}(R)$, and NLoS point process Φ_{NLoS} with density function $\lambda(1-f_{\mathrm{Pr}}(R))$. Accordingly, by using

the Slivnyak's theorem [99], $\Xi_2(z)$ is given by

$$\begin{aligned}\Xi_2(z) &= \mathbb{E}\left[e^{-z\mathscr{I}}\right] = \mathbb{E}\left[e^{-z(\mathscr{I}_{\mathrm{LoS}}+\mathscr{I}_{\mathrm{NLoS}})}\right] \\ &= \mathbb{E}\left[e^{-z\mathscr{I}_{\mathrm{LoS}}}\right]\mathbb{E}\left[e^{-z\mathscr{I}_{\mathrm{NLoS}}}\right]\end{aligned} \tag{G.3}$$

with

$$\begin{cases} \mathscr{I}_{\mathrm{LoS}} = \sum_{i\in\Phi_{\mathrm{LoS}}} P_t G_i L(|X_i|), \\ \mathscr{I}_{\mathrm{NLoS}} = \sum_{i\in\Phi_{\mathrm{NLoS}}} P_t G_i L(|X_i|). \end{cases} \tag{G.4}$$

By applying the Laplace functional of the PPP [99],

$$\begin{aligned}\mathbb{E}\left[e^{-z\mathscr{I}_{\mathrm{LoS}}}\right] &= \exp\Big(-2\pi\lambda\times \\ \int_0^\infty f_{\mathrm{Pr}}(u)\Big(1-\underbrace{\mathbb{E}\left[e^{-zP_tG_i\beta(\max\{u,d\})^{-\alpha_{\mathrm{LoS}}}}\right]}_{\Omega_1}\Big)udu\Big).\end{aligned} \tag{G.5}$$

Based on the array gain distribution in (4.1) and the law of total expectation, Ω_1 is obtained as

$$\Omega_1(z,u) = \sum_{\ell,k\in\{\mathrm{M,m}\}} \mathrm{Pr}_{\ell k} \times e^{-zP_tG_\ell G_k\beta(\max\{u,d\})^{-\alpha_{\mathrm{LoS}}}}. \tag{G.6}$$

Likewise, we can derive $\mathbb{E}\left[e^{-z\mathscr{I}_{\mathrm{NLoS}}}\right]$. Then, we get $\Xi_2(z)$ in (4.9). Based on (G.1) and (4.9), we attain the desired result in (4.7) and complete the proof.

Appendix G

Appendix H: A detailed derivation of Eq. (4.10)

The average rate between the typical transmitting node and its intended receiver can be tightly lower bounded as [70]

$$\bar{R}_1^{\mathrm{L}} = \log_2\left(1 + e^{\mathbb{E}[\ln \gamma_o]}\right), \tag{H.1}$$

where $\mathbb{E}[\ln \gamma_o]$ is calculated as

$$\begin{aligned}\mathbb{E}[\ln \gamma_o] = &\underbrace{\mathbb{E}\left[\ln\left(P_t G_{\mathrm{M}}^2 \beta r^{-\alpha_o}\right)\right]}_{Z_1} + \\ &\underbrace{\mathbb{E}\left[\ln\left(\frac{1}{\sum_{i\in\Phi/o} P_t G_i \beta |X_{i,o}|^{-\alpha_i} + N_o}\right)\right]}_{Z_2}.\end{aligned} \tag{H.2}$$

Since the typical link can be either LoS or NLoS, using the law of total probability, Z_1 is calculated as

$$Z_1 = \ln\left(P_t G_{\mathrm{M}}^2 \beta\right) - \left(f_{\mathrm{Pr}}(r)\,\alpha_{\mathrm{LoS}} + (1 - f_{\mathrm{Pr}}(r))\,\alpha_{\mathrm{NLoS}}\right)\ln r, \tag{H.3}$$

where α_{LoS} and α_{NLoS} are the path loss exponents of the LoS and the NLoS, respectively.

Considering the convexity of $\ln\left(\frac{1}{1+x}\right)$ and using Jensen's inequality, we derive

the lower bound on the Z_2 as

$$Z_2^{\mathrm{L}} = \ln\left(\frac{1}{\underbrace{\mathbb{E}\left[\sum_{i\in\Phi/o} P_t G_i \beta |X_{i,o}|^{-\alpha_i}\right]}_{\overline{\Lambda}} + N_o}\right). \tag{H.4}$$

Using a similar approach in (G.3), Λ is derived as

$$\begin{aligned}
\overline{\Lambda} &= \mathbb{E}\left[\sum_{i\in\Phi_{\mathrm{LoS}}} P_t G_i \beta \left(\max\left\{|X_{i,o}|, d\right\}^{-\alpha_{\mathrm{LoS}}}\right)\right] \\
&+ \mathbb{E}\left[\sum_{i\in\Phi_{\mathrm{NLoS}}} P_t G_i \beta \left(\max\left\{|X_{i,o}|, d\right\}^{-\alpha_{\mathrm{NLoS}}}\right)\right] \\
&\overset{(a)}{=} P_t \bar{G} \beta 2\pi\lambda \times \Bigg(\int_0^d \left((d^{-\alpha_{\mathrm{LoS}}} - d^{-\alpha_{\mathrm{NLoS}}}) r f_{\mathrm{Pr}}(r) + d^{-\alpha_{\mathrm{NLoS}}} r\right) dr \\
&\quad + \int_d^\infty \left((r^{1-\alpha_{\mathrm{LoS}}} - r^{1-\alpha_{\mathrm{NLoS}}}) f_{\mathrm{Pr}}(r) + r^{1-\alpha_{\mathrm{NLoS}}}\right) dr \Bigg),
\end{aligned} \tag{H.5}$$

where $\bar{G}$ is the average array gain. Here, step (a) results from using Campbell's theorem [81]. Based on (4.1) and using the law of total expectation, $\bar{G}$ is calculated as

$$\bar{G} = \mathbb{E}\{G_i\} = \sum_{\ell,k\in\{\mathrm{M,m}\}} G_{\ell k} \mathrm{Pr}_{\ell k}. \tag{H.6}$$

Substituting (H.3), (H.4) and (H.5) into (H.2), we obtain $\mathbb{E}\{\ln\gamma_o\}$ in (H.1), and the desired result (4.10).

Appendix H

Appendix I: A detailed derivation of Theorem 6

The average rate $\overline{R}_{e^*}$ is calculated as

$$\begin{aligned}\overline{R}_{e^*} &= \mathbb{E}\left[\log_2\left(1+\gamma_{e^*}\right)\right] \\ &= \frac{1}{\ln 2}\int_0^{\infty}\frac{\left(1-F_{\gamma_{e^*}}\left(x\right)\right)}{1+x}dx,\end{aligned} \tag{I.1}$$

where $F_{\gamma_{e^*}}\left(\cdot\right)$ is the cumulative distribution function (CDF) of γ_{e^*}. By using the thinning theorem [81], the eavesdroppers are divided into the LoS point process Φ_e^{LoS} with density function $\lambda_e f_{\mathrm{Pr}}(R)$, and NLoS point process Φ_e^{NLoS} with density function $\lambda_e(1-f_{\mathrm{Pr}}(R))$. Then, $F_{\gamma_{e^*}}\left(\cdot\right)$ is given by

$$\begin{aligned}F_{\gamma_{e^*}}\left(x\right) &= \Pr\left(\gamma_{e^*}<x\right) \\ &= \Pr\left(\max\left\{\gamma_{e^*}^{\mathrm{LoS}},\gamma_{e^*}^{\mathrm{NLoS}}\right\}<x\right) \\ &= \underbrace{\Pr\left(\gamma_{e^*}^{\mathrm{LoS}}<x\right)}_{\mathscr{P}_1(x)}\underbrace{\Pr\left(\gamma_{e^*}^{\mathrm{NLoS}}<x\right)}_{\mathscr{P}_2(x)},\end{aligned} \tag{I.2}$$

where

$$\begin{cases}\gamma_{e^*}^{\mathrm{LoS}} = \max\limits_{e\in\Phi_e^{\mathrm{LoS}}}\left\{\dfrac{P_t G_e L\left(|X_e|\right)}{\sigma_e^2}\right\}, \\ \gamma_{e^*}^{\mathrm{NLoS}} = \max\limits_{e\in\Phi_e^{\mathrm{NLoS}}}\left\{\dfrac{P_t G_e L\left(|X_e|\right)}{\sigma_e^2}\right\}.\end{cases} \tag{I.3}$$

We first derive $\mathscr{P}_1(x)$ as

$$\begin{aligned}
&\mathscr{P}_1(x) = \Pr\left(\gamma_{e^*}^{\mathrm{LoS}} < x\right) \\
&= \mathbb{E}\left[\prod_{e\in\Phi_e^{\mathrm{LoS}}} \Pr\left(\frac{P_t G_e \beta \left(\max\{r_e, d\}\right)^{-\alpha_{\mathrm{LoS}}}}{\sigma_e^2} < x\right)\right] \\
&\overset{(a)}{=} \exp\Big\{-2\pi\lambda_e \times \\
&\int_0^{\infty} \underbrace{\Pr\big(\frac{P_t G_e \beta \left(\max\{r_e, d\}\right)^{-\alpha_{\mathrm{LoS}}}}{\sigma_e^2} > x\big)}_{\Theta} f_{\mathrm{Pr}}(r_e) r_e dr_e\Big\},
\end{aligned} \tag{I.4}$$

where step (a) is obtained by using the Laplace functional. Based on the law of total probability, Θ is calculated as

$$\Theta = \sum_{\ell,n\in\{\mathrm{M},\mathrm{m}\}} \mathbf{1}\left(\max\{r_e, d\} < \big(\frac{P_t G_\ell G_n^e \beta}{x\sigma_e^2}\big)^{\frac{1}{\alpha_{\mathrm{LoS}}}}\right) \mathrm{Pr}_{\ell n}, \tag{I.5}$$

Substituting (I.5) into (I.4), we get $\mathscr{P}_1(x)$ in (4.15). Then, $\mathscr{P}_2(x)$ is similarly derived as (4.16).

Bibliography

[1] Sijia Deng, Mathew K Samimi, and Theodore S Rappaport. 28 GHz and 73 GHz millimeter-wave indoor propagation measurements and path loss models. In *Prof. IEEE Int. Conf.on Commun. Workshop (ICCW)*, pages 1244–1250, 2015.

[2] Theodore S Rappaport, Eshar Ben-Dor, James N Murdock, and Yijun Qiao. 38 GHz and 60 GHz angle-dependent propagation for cellular & peer-to-peer wireless communications. In *Proc. IEEE Int. Conf. Commun. (ICC)*, pages 4568–4573, 2012.

[3] Kiran Venugopal, Matthew C Valenti, and R. W. Heath Jr. Interference in finite-sized highly dense millimeter wave networks. In *Information Theory and Applications Workshop (ITA), 2015*, pages 175–180, 2015.

[4] Akira Hashimoto, Hitoshi Yoshino, and Hiroyuki Atarashi. Roadmap of imt-advanced development. *Microwave Magazine, IEEE*, 9(4):80–88, 2008.

[5] Nisha Panwar, Shantanu Sharma, and Awadhesh Kumar Singh. A survey on 5g: The next generation of mobile communication. *Physical Communication*, 2016.

[6] Rui Zhang and Chin Keong Ho. MIMO broadcasting for simultaneous wireless information and power transfer. *Wireless Communications, IEEE Transactions on*, 12(5):1989–2001, May 2013.

[7] Kaibin Huang and V. K. N. Lau. Enabling wireless power transfer in cellular

networks: Architecture, modeling and deployment. *Wireless Communications, IEEE Transactions on*, 13(2):902–912, February 2014.

[8] Liang Liu, Rui Zhang, and Kee-Chaing Chua. Wireless information transfer with opportunistic energy harvesting. *IEEE Transactions on Wireless Communications*, 12(1):288–300, jan 2013.

[9] Congzheng Han, Tim Harrold, Simon Armour, Ioannis Krikidis, Stefan Videv, Peter M Grant, Harald Haas, John S Thompson, Ivan Ku, Cheng-Xiang Wang, et al. Green radio: radio techniques to enable energy-efficient wireless networks. *Communications Magazine, IEEE*, 49(6):46–54, 2011.

[10] Kaya Tutuncuoglu and Aylin Yener. Optimum transmission policies for battery limited energy harvesting nodes. *Wireless Communications, IEEE Transactions on*, 11(3):1180–1189, 2012.

[11] Marios Gatzianas, Leonidas Georgiadis, and Leandros Tassiulas. Control of wireless networks with rechargeable batteries [transactions papers]. *IEEE Transactions on Wireless Communications*, 9(2):581–593, 2010.

[12] Jing Yang and Sennur Ulukus. Transmission completion time minimization in an energy harvesting system. In *Information Sciences and Systems (CISS), 2010 44th Annual Conference on*, pages 1–6. IEEE, 2010.

[13] Mukherji Utpal Joseph Vinay Sharma, Vinod and Shrey Gupta. Optimal energy management policies for energy harvesting sensor nodes. *IEEE Transactions on Wireless Communications*, 9(4):1326–1336, Apr 2010.

[14] Chin Keong Ho and Rui Zhang. Optimal energy allocation for wireless communications powered by energy harvesters. In *Information Theory Proceedings (ISIT), 2010 IEEE International Symposium on*, pages 2368–2372. IEEE, Sep 2010.

[15] Liang Liu, Rui Zhang, and Kee-Chaing Chua. Secrecy wireless information and power transfer with miso beamforming. pages 1831–1836, Apr 2013.

[16] Muhammad RA Khandaker and Kai-Kit Wong. Robust secrecy beamforming with energy-harvesting eavesdroppers. *Wireless Communications Letters, IEEE*, 4(1):10–13, Feb 2015.

[17] Muhammad RA Khandaker and Kai-Kit Wong. Masked beamforming in the presence of energy-harvesting eavesdroppers. *Information Forensics and Security, IEEE Transactions on*, 10(1):40–54, Jan 2015.

[18] Liu Liang Lee, Seunghyun and Rui Zhang. Collaborative wireless energy and information transfer in interference channel. *IEEE Transactions on Wireless Communications*, 14(1):545–557, 2015.

[19] Jeffrey G Andrews, Stefano Buzzi, Wan Choi, Stephen V Hanly, Aurelie Lozano, Anthony CK Soong, and Jianzhong Charlie Zhang. What will 5g be? *IEEE Journal on Selected Areas in Communications*, 32(6):1065–1082, 2014.

[20] Han-Shin Jo, Young Jin Sang, Ping Xia, and Jeffrey G Andrews. Heterogeneous cellular networks with flexible cell association: A comprehensive downlink sinr analysis. *IEEE Transactions on Wireless Communications*, 11(10):3484–3495, 2012.

[21] Jeffrey G Andrews, François Baccelli, and Radha Krishna Ganti. A tractable approach to coverage and rate in cellular networks. *IEEE Transactions on Communications*, 59(11):3122–3134, 2011.

[22] Dilip Bethanabhotla, Ozgun Y. Bursalioglu, Haralabos C. Papadopoulos, and Giuseppe Caire. Optimal user-cell association for massive MIMO wireless networks. *arXiv preprint arXiv:1407.6731*, 2014.

[23] Ning Wang, Ekram Hossain, and Vijay K. Bhargava. Joint downlink cell association and bandwidth allocation for wireless backhauling in two-tier hetnets with large-scale antenna arrays. *CoRR*, abs/1501.00078, 2015.

[24] E. Björnson, M. Kountouris, and M. Debbah. Massive MIMO and small cells: Improving energy efficiency by optimal soft-cell coordination. In *Proc. 2013 20th Int. Conf. on Telecommun.*, pages 1–5, May 2013.

[25] Yi Xu and Shiwen Mao. User association in massive mimo hetnets. *CoRR*, abs/1501.03407, 2015.

[26] Hu Rose and Yi Qian. An energy efficient and spectrum efficient wireless heterogeneous network framework for 5g systems. *Communications Magazine, IEEE*, 52(5):94–101, 2014.

[27] Federico Boccardi, Robert W Heath, Aurelie Lozano, Thomas L Marzetta, and Petar Popovski. Five disruptive technology directions for 5g. *Communications Magazine, IEEE*, 52(2):74–80, 2014.

[28] Erik Larsson, Ove Edfors, Fredrik Tufvesson, and Thomas Marzetta. Massive mimo for next generation wireless systems. *Communications Magazine, IEEE*, 52(2):186–195, 2014.

[29] Young-Han Nam, Boon Loong Ng, Krishna Sayana, Yang Li, Jianzhong Zhang, Younsun Kim, and Juho Lee. Full-dimension mimo (fd-mimo) for next generation cellular technology. *Communications Magazine, IEEE*, 51(6):172–179, 2013.

[30] Thomas L Marzetta. Noncooperative cellular wireless with unlimited numbers of base station antennas. *IEEE Transactions on Wireless Communications*, 9(11):3590–3600, Nov. 2010.

[31] Gang Yang, Chin Keong Ho, Rui Zhang, and Yong Liang Guan. Throughput optimization for massive MIMO systems powered by wireless energy transfer. *IEEE Journal on Selected Areas in Communications*, 33(8):1640–1650, Aug 2015.

[32] Volker Jungnickel, Konstantinos Manolakis, Wolfgang Zirwas, Berthold Panzner, Volker Braun, Moritz Lossow, Mikael Sternad, Rikke Apelfrojd, and

Tommy Svensson. The role of small cells, coordinated multipoint, and massive mimo in 5g. *Communications Magazine, IEEE*, 52(5):44–51, 2014.

[33] Xiang Cheng, Bo Yu, Liuqing Yang, Jianhua Zhang, Guangyi Liu, Yong Wu, and Lei Wan. Communicating in the real world: 3d mimo. *Wireless Communications, IEEE*, 21(4):136–144, 2014.

[34] Theodore S Rappaport, Shu Sun, Rimma Mayzus, Hang Zhao, Yaniv Azar, Kevin Wang, George N Wong, Jocelyn K Schulz, Mathew Samimi, and Felix Gutierrez. Millimeter wave mobile communications for 5g cellular: It will work! *IEEE access*, 1:335–349, 2013.

[35] K. Huang, J. G. Andrews, D. Guo, R. W. Heath Jr., and R. A. Berry. Spatial interference cancellation for multiantenna mobile ad hoc networks. 58(3):1660–1676, March 2012.

[36] Zhouyue Pi and F. Khan. An introduction to millimeter-wave mobile broadband systems. *IEEE Commun. Mag.*, 49(6):101–107, June 2011.

[37] Andrew Thornburg, Tianyang Bai, and R. W. Heath Jr. Performance analysis of outdoor mmWave ad hoc networks. 64(15):4065–4079, August 2016.

[38] N. Valliappan, A. Lozano, and R. W. Heath Jr. Antenna subset modulation for secure millimeter-wave wireless communication. 61(8), August 2013.

[39] Nan Yang, Lifeng Wang, Giovanni Geraci, Maged Elkashlan, Jinhong Yuan, and Marco Di Renzo. Safeguarding 5G wireless communication networks using physical layer security. 53(4):20–27, 2015.

[40] D. Steinmetzer, J. Chen, J. Classen, E. Knightly, and M. Hollick. Eavesdropping with periscopes: Experimental security analysis of highly directional millimeter waves. In *IEEE Conf. on Commun. and Netw. Security (CNS)*, pages 335–343, 2015.

[41] Saad G Kiani and David Gesbert. Capacity maximizing power allocation for interfering wireless links: A distributed approach. In *Global Telecommunications Conference, 2007. GLOBECOM'07. IEEE*, pages 1405–1409. IEEE, 2007.

[42] Stephen A Maas. *Nonlinear microwave and RF circuits*. Artech House, 2003.

[43] Dipak L Sengupta and Tapan K Sarkar. Maxwell, hertz, the maxwellians, and the early history of electromagnetic waves. *Antennas and Propagation Magazine, IEEE*, 45(2):13–19, 2003.

[44] Zuleita Ka Ming Ho and David Gesbert. Balancing egoism and altruism on interference channel: The mimo case. In *Communications (ICC), 2010 IEEE International Conference on*, pages 1–5. IEEE, 2010.

[45] Michael J Neely, Eytan Modiano, and Chih-Ping Li. Fairness and optimal stochastic control for heterogeneous networks. *Networking, IEEE/ACM Transactions on*, 16(2):396–409, 2008.

[46] Alessio Zappone, Luca Sanguinetti, Giacomo Bacci, Eduard Jorswieck, and Mérouane Debbah. Energy-efficient power control: A look at 5g wireless technologies. *arXiv preprint arXiv:1503.04609*, 2015.

[47] José F Paris, M del Carmen Aguayo-Torres, and José T Entrambasaguas. Optimum discrete-power adaptive qam scheme for rayleigh fading channels. *Communications Letters, IEEE*, 5(7):281–283, 2001.

[48] Haibo Dai, Yongming Huang, and Luxi Yang. Game theoretic max-logit learning approaches for joint base station selection and resource allocation in heterogeneous networks. *IEEE Journal on Selected Areas in Communications*, 33(6):1–14, 2015.

[49] Lingyang Song, Dusit Niyato, Zhu Han, and Ekram Hossain. Game-theoretic resource allocation methods for device-to-device communication. *Wireless Communications, IEEE*, 21(3):136–144, 2014.

[50] Yonglong Zhang, Dilip Bethanabhotla, Tianyu Hao, and Konstantinos Psounis. Near-optimal user-cell association schemes for real-world networks. In *Information Theory and Applications Workshop (ITA), 2015*, pages 204–213. IEEE, 2015.

[51] Steven Corroy, Laetitia Falconetti, and Rudolf Mathar. Dynamic cell association for downlink sum rate maximization in multi-cell heterogeneous networks. In *Communications (ICC), 2012 IEEE International Conference on*, pages 2457–2461. IEEE, 2012.

[52] Lidong Zhou and Z. J. Haas. Securing ad hoc networks. *IEEE Network*, 13(6):24–30, 1999.

[53] Jing Huang and A. L. Swindlehurst. Cooperative jamming for secure communications in MIMO relay networks. 59(10):4871–4884, October 2011.

[54] Yingbin Liang, H. V. Poor, and S. Shamai. Secure communication over fading channels. 54(6):2470–2492, June 2008.

[55] Lifeng Wang, Nan Yang, M. Elkashlan, Phee Lep Yeoh, and Jinhong Yuan. Physical layer security of maximal ratio combining in two-wave with diffuse power fading channels. *IEEE Trans. Inf. Forensics Security*, 9(2):247–258, Feb. 2014.

[56] X. Zhou and M. R. Mckay. Secure transmission with artificial noise over fading channels: Achievable rate and optimal power allocation. 59(8):3831–3842, October 2010.

[57] T. Lv, H. Gao, and S. Yang. Secrecy transmit beamforming for heterogeneous networks. 33(6):1154–1170, 2015.

[58] H. M. Wang, T. X. Zheng, J. Yuan, D. Towsley, and M. H. Lee. Physical layer security in heterogeneous cellular networks. 64(3):1204–1219, March 2016.

[59] Jun Zhu, R. Schober, and V. K. Bhargava. Secure transmission in multicell massive MIMO systems. 13(9):4766–4781, Sept 2014.

[60] Xiangyun Zhou, R. K. Ganti, J. G. Andrews, and A. Hjorungnes. On the throughput cost of physical layer security in decentralized wireless networks. 10(8):2764–2775, August 2011.

[61] Y. Deng, L. Wang, M. Elkashlan, A. Nallanathan, and R. K. Mallik. Physical layer security in three-tier wireless sensor networks: A stochastic geometry approach. 11(6):1128–1138, June 2016.

[62] Xi Zhang, Xiangyun Zhou, and M. R. McKay. Enhancing secrecy with multi-antenna transmission in wireless ad hoc networks. 8(11):1802–1814, November 2013.

[63] C. Cai, Y. Cai, X. Zhou, W. Yang, and W. Yang. When does relay transmission give a more secure connection in wireless ad hoc networks? 9(4):624–632, April 2014.

[64] C. Wang and H. M. Wang. Physical layer security in millimeter wave cellular networks. 15(8):5569–5585, August 2016.

[65] S. Vuppala, S. Biswas, and T. Ratnarajah. An analysis on secure communication in millimeter/micro-wave hybrid networks. 64(8):3507–3519, August 2016.

[66] S. Gong, C. Xing, Z. Fei, and S. Ma. Millimeter-wave secrecy beamforming designs for two-way amplify-and-forward MIMO relaying networks. Early Access Articles, pp. 1-12, 2016.

[67] Ali A Nasir, Xiangyun Zhou, Salman Durrani, and Rodney A Kennedy. Wireless-powered relays in cooperative communications: Time-switching relaying protocols and throughput analysis. *IEEE Transactions on Communications*, 63(5):1607–1622, 2015.

[68] E. Hossain and M. Hasan. 5G cellular: Key enabling technologies and research challenges. *IEEE Instrumentation Measurement Mag.*, 18(3):11–21, Jun. 2015.

[69] Hien Quoc Ngo, Erik G. Larsson, and Thomas L. Marzetta. Energy and spectral efficiency of very large multiuser MIMO systems. *IEEE Transactions on Communications*, 61(4):1436–1449, Apr. 2013.

[70] Hien Quoc Ngo Maged Elkashlan Trung Q. Duong Wang, Lifeng and Kai-Kit Wong. Massive mimo in spectrum sharing networks: Achievable rate and power efficiency. *IEEE Systems Journal*, pages 1–12, 2015.

[71] Xiaoming Chen, Xiumin Wang, and Xianfu Chen. Energy-efficient optimization for wireless information and power transfer in large-scale MIMO systems employing energy beamforming. *Wireless Communications Letters, IEEE*, 2(6):667–670, December 2013.

[72] Hengzhi Wang, Wei Wang, Xiaoming Chen, and Zhaoyang Zhang. Wireless information and energy transfer in interference aware massive mimo systems. In *Global Communications Conference (GLOBECOM), 2014 IEEE*, pages 2556–2561. IEEE, 2014.

[73] Dantong Liu, Lifeng Wang, Yue Chen, Tiankui Zhang, Kok Keong Chai, and Maged Elkashlan. Distributed energy efficient fair user association in massive mimo enabled hetnets. *Communications Letters, IEEE*, 19(10):1770–1773, 2015.

[74] Volker Jungnickel, Konstantinos Manolakis, Wolfgang Zirwas, Berthold Panzner, Volker Braun, Moritz Lossow, Mikael Sternad, Rikke Apelfröjd, and Tommy Svensson. The role of small cells, coordinated multipoint, and massive mimo in 5g. *Communications Magazine, IEEE*, 52(5):44–51, 2014.

[75] Federico Boccardi, Jeffrey Andrews, Hisham Elshaer, Mischa Dohler, Stefan Parkvall, Petar Popovski, and Sarabjot Singh. Why to decouple the uplink and downlink in cellular networks and how to do it. *arXiv preprint arXiv:1503.06746*, Mar. 2015.

[76] F. Baccelli, B. Blaszczyszyn, and P. Muhlethaler. An Aloha protocol for mul-

tihop mobile wireless networks. *IEEE Transactions on Information Theory*, 52(2):421–436, Feb. 2006.

[77] Hoon Huh, Antonia M Tulino, and Giuseppe Caire. Network mimo with linear zero-forcing beamforming: Large system analysis, impact of channel estimation, and reduced-complexity scheduling. *IEEE Transactions on Information Theory*, 58(5):2911–2934, 2012.

[78] Dilip Bethanabhotla, Ozgun Y. Bursalioglu, Haralabos C. Papadopoulos, and Giuseppe Caire. Optimal user-cell association for massive mimo wireless networks. *IEEE Transactions on Wireless Communications*, 58(5):1835 – 1850, 2012.

[79] Kianoush Hosseini, Wei Yu, and Raviraj S Adve. Large-scale mimo versus network mimo for multicell interference mitigation. *Selected Topics in Signal Processing, IEEE Journal of*, 8(5):930–941, 2014.

[80] Israel S Gradshteyn and IM Ryzhik. *Table of integrals, series, and products. Translated from the Russian. Translation edited and with a preface by Alan Jeffrey and Daniel Zwillinger*. Academic Press, Inc., San Diego, CA, 2000.

[81] François Baccelli and Bartlomiej Błszczyszyn. *Stochastic geometry and wireless networks: Theory*, volume 1. Now Publishers Inc. Hanover, MA, USA, 2009.

[82] A. M. Hunter, J. G. Andrews, and S. Weber. Transmission capacity of ad hoc networks with spatial diversity. 7(12):5058–5071, December 2008.

[83] Tianyang Bai and Robert W. Heath Jr. Coverage and rate analysis for millimeter-wave cellular networks. 14(2):1100–1114, February 2015.

[84] S. Singh, M. N. Kulkarni, A. Ghosh, and J. G. Andrews. Tractable model for rate in self-backhauled millimeter wave cellular networks. 33(10):2196–2211, October 2015.

[85] O. El Ayach, S. Rajagopal, S. Abu-Surra, Z. Pi, and R. W. Heath Jr. Spatially sparse precoding in millimeter wave MIMO systems. 13(3):1499–1513, March 2014.

[86] T.S. Rappaport, Shu Sun, R. Mayzus, Hang Zhao, Y. Azar, K. Wang, G. N. Wong, J. K. Schulz, M. Samimi, and F. Gutierrez. Millimeter wave mobile communications for 5G cellular: It will work! *IEEE Access*, 1:335–349, May 2013.

[87] G. Geraci, H. S. Dhillon, J. G. Andrews, Jinhong Yuan, and I. B. Collings. Physical layer security in downlink multi-antenna cellular networks. 62(6):2006–2021, June 2014.

[88] Lun Dong, Zhu Han, A. P. Petropulu, and H. V. Poor. Improving wireless physical layer security via cooperating relays. 58(3):1875–1888, March 2010.

[89] Matthieu Bloch, Joõo Barros, Miguel RD Rodrigues, and Steven W McLaughlin. Wireless information-theoretic security. *IEEE Transactions on Information Theory*, 54(6):2515–2534, 2008.

[90] S. Rangan, T. S. Rappaport, and E. Erkip. Millimeter-wave cellular wireless networks: Potentials and challenges. *IEEE Proc.*, 102(3):366–385, 2014.

[91] H. Shokri-Ghadikolaei, C. Fischione, G. Fodor, P. Popovski, and M. Zorzi. Millimeter wave cellular networks: A MAC layer perspective. 63(10):3437–3458, October 2015.

[92] J. Park, S. L. Kim, and J. Zander. Tractable resource management with uplink decoupled millimeter-wave overlay in ultra-dense cellular networks. 15(6):4362–4379, June 2016.

[93] Nektarios Moraitis and Philip Constantinou. Indoor channel capacity evaluation utilizing ULA and URA antennas in the millimeter wave band. In *IEEE Personal, Indoor and Mobile Radio Commun.(PIMRC)*, pages 1–5, 2007.

[94] Anders Gjendemsjø, David Gesbert, Geir E Oien, and Saad G Kiani. Binary power control for sum rate maximization over multiple interfering links. *IEEE Transactions on Wireless Communications*, 7(8):3164–3173, Aug. 2008.

[95] Alexander Pyattaev, Kerstin Johnsson, Sergey Andreev, and Yevgeni Koucheryavy. Communication challenges in high-density deployments of wearable wireless devices. *Wireless Communications, IEEE*, 22(1):12–18, 2015.

[96] Han-Shin Jo, Young Jin Sang, Ping Xia, and Jeffrey G Andrews. Heterogeneous cellular networks with flexible cell association: A comprehensive downlink sinr analysis. *IEEE Transactions, Wireless Communications*, 11(10):3484–3495, Oct. 2012.

[97] Martin Haenggi. *Stochastic geometry for wireless networks*. Cambridge University Press, 2012.

[98] K. A. Hamdi. Capacity of MRC on correlated rician fading channels. 56(5):708–711, May 2008.

[99] M. Haenggi, J. G. Andrews, F. Baccelli, O. Dousse, and M. Franceschetti. Stochastic geometry and random graphs for the analysis and design of wireless networks. 27(7):1029–1046, 2009.